The Dissertation Committee for Mohammed Abdullah Alhussain Certifies that this is the approved version of the following dissertation:

Fracture Characterization of a Carbonate Reservoir in the Arabian Peninsula

Committee:

Mrinal K. Sen, Supervisor

Kyle T. Spikes

Paul L. Stoffa

Robert H. Tatham

Osareni C. Ogiesoba

Yosio Nakamura

Fracture Characterization of a Carbonate Reservoir in the Arabian Peninsula

by

Mohammed Abdullah Alhussain, B.S.; M.S.

DISSERTATION

Presented to the Faculty of the Graduate School of

The University of Texas at Austin

in Partial Fulfillment

of the Requirements

for the Degree of

DOCTOR OF PHILOSOPHY

The University of Texas at Austin

May 2013

Dedication

To my parents, wife and kids

Acknowledgements

I would like to express my gratitude to my advisor Prof. Mrinal K. Sen for his endless support throughout my Ph.D. He has been there whenever I needed him. He has been a great source of encouragement and inspiration through difficult times. Now I understand why he was persistent on working on my research from day one and waste no time. I am truly thankful to him for believing in me.

I would like also to thank Dr. Kyle T, Spikes for his constant guidance and support. I have learned a lot from him through many useful discussions. I thank him for having his door open whenever I needed help. I have learned a lot from his course "Rock Physics" which helped me in my research.

I would like to thank Prof. Paul L. Stoffa for encouragement and advice throughout my research and for believing that I can come up with useful research results. I also would like to thank Prof. Robert H. Tatham, Dr. Osareni C. Ogiesoba and Prof. Yosio Nakamura for great discussions and for serving on my committee. Their insightful comments provided valuable inputs to my dissertation. I also would like to thank Thomas E. Hess for his endless support in dealing with real data. With his help I was able to apply my new technique to real data in a timely manner. Many thanks to the graduate program coordinator Mr. Philip Guerrero for his help throughout my PhD program.

I would like to thank Dr. Panos Kelamis in Saudi Aramco for his endless support and my mentor Dr. Tonellot for his help in providing the real data for my research and for great discussions. I also thank Saudi Aramco for funding my Ph.D. program.

My sincere thanks to the graduate students: Yi Tao, Terence Campbell, and Corey Joy for their constant support and useful discussions.

Fracture Characterization of a Carbonate Reservoir in the Arabian Peninsula

Mohammed Abdullah Alhussain, Ph.D

The University of Texas at Austin, 2013

Supervisor: Mrinal K. Sen

Estimation of reservoir fracture parameters, fracture orientation and density, from seismic data is often difficult because of one important question: Is observed anisotropy caused by the reservoir interval or by the effect of the lithologic unit or multiple units above the reservoir? Often hydrocarbon reservoirs represent a small portion of the seismic section, and reservoir anisotropic parameter inversion can be easily obscured by the presence of an anisotropic overburden. In this study, I show examples where we can clearly observe imprints of overburden anisotropic layers on the seismic response of the target zone. Then I present a simple method to remove the effect of anisotropic overburden to recover reservoir fracture parameters. It involves analyzing amplitude variation with offset and azimuth (AVOA) for the top of reservoir reflector and for a reflector below the reservoir. Seismic CMP gathers are transformed to delay-time vs. slowness (tau-p) domain. We then calculate the ratio of the amplitudes of reflections at the reservoir top and from the reflector beneath the reservoir. The ratios of these amplitudes are then used to isolate the effect of the reservoir interval and remove the transmission effect of the overburden.

The methodology is tested on two sets of models - one containing a fractured reservoir with isotropic overburden and the other containing a fractured reservoir with anisotropic

overburden. Conventional analysis in the x-t domain indicates that the anisotropic overburden has completely obscured the anisotropic signature of the reservoir zone. When the new methodology is applied, the overburden effect is significantly reduced. The methodology is also applied to an actual PP surface reflection (R_{pp}) 3D dataset over a reservoir in the Arabian Peninsula. Ellipse-fitting technique was applied to invert for two Fracture parameters: (1) Fracture density and (2) fracture direction. Fracture density inversion results indicate increased fracturing in the anticline structure hinge zone. Fracture orientation inversion results agree with Formation MicroImaging (FMI) borehole logs showing a WNW-ESE trend.

This newly developed amplitude ratio method is suitable for quantitative estimation of fracture parameters including normal and tangential "weaknesses" (ΔN and ΔT respectively). Initially, inversion of conventional AVOA for ΔN and ΔT parameters indicates that the ΔN parameter is reliably estimated given an accurate background isotropic parameter estimation derived from borehole logging data. While ΔN parameter inversion is successful, inversion for ΔT parameter from R_{pp} information is not, presumably due to the dependence of ΔT estimation on many medium parameters for accurate prediction. The ΔN parameter is then successfully recovered when applied to the amplitude ratio values derived from synthetic data. It is important to recognize that ΔN parameter is directly proportional to fracture density and high ΔN values can be attributed to high crack density values.

The ΔN parameter inversion is also applied to the amplitude ratios derived from real seismic data. This inversion requires fracture azimuth data input that is obtained from the fracture direction inversion using ellipse-fitting technique. The background Vp/Vs ratio,

estimated from well logs, is another required parameter for ΔN estimation. Inversion results are promising when fracture density computed from ΔN parameter is compared to the facture density computed from ellipse-fitting technique. The maps of both attributes show similarities with more fractures located at the anticline structure hinge. Spatial variability in fracture parameters has proven valuable in locating "sweet spots" areas or highly fractured zones within the reservoir interval.

Table of Contents

List of Tables

List of Figures

Chapter 1: Introduction

Natural fractures in petroleum reservoirs play an important role in determining fluid flow, and ultimately production. Knowledge of the orientation and density of fractures is required to optimize production (Sayers, 2009). In recent years analysis of surface seismic observations has played a significant role in exploration and development of hydrocarbon reservoirs. This is partially accredited to the development of inversion techniques that provide information on interval reservoir properties, in addition to a structure map, to interpreters and reservoir engineers. One example is a fracture characterization (orientation and density map), which can be of great help in exploring for new hydrocarbon reservoirs or managing production of existing ones.

The second chapter of this dissertation gives the background theory covering various subjects related to my research area. The first part discusses seismic anisotropy, its definition, significance, causes and symmetry classes. The second part addresses the theory of seismic partitioning of energy at an interface. In particular, the importance of amplitude variation with offset (AVO) in quantifying medium parameters is highlighted. Both isotropic and anisotropic AVO equations are discussed. The third part provides a background on effective medium theory and how fractures are represented as a "bulk" rock property.

In the third chapter, I use an effective-medium model to represent a fractured porous medium. A sensitivity analysis of Thomsen's (1986) Epsilon parameter is performed to measure the difference between elastic properties of a wave propagating

parallel to and across the fracture strike direction. Anisotropic reflection analysis is performed for a two-layer (isotropic over fractured model), to study the effect of variations in the model parameters on the amplitude variation with offset and azimuth (AVOA) response and consequently the commonly interpreted intercept and gradient attributes.

In the fourth chapter, I propose an amplitude ratio technique to remove the effect of transmission through the overburden which may cause erroneous analysis of reservoir parameter estimation. It involves analyzing AVOA for reflections above and below the reservoir. I show that the technique results in a more accurate estimation of reservoir fracture parameters.

In the fifth chapter, the amplitude ratio method is applied to a PP 3D dataset from the Arabian Peninsula. The analysis involves predicting two reservoir fracture parameters: (1) Fracture density and (2) fracture orientation. The results are compared to the interpretation of FMI logs for a couple of horizontal wells in the reservoir. Post-stack coherency and curvature attributes are calculated and compared to the pre-stack ratio attributes.

In chapter six I perform a quantitative analysis of reservoir fracture properties, namely, fracture normal and tangential weaknesses or ΔN and ΔT, respectively. To test the accuracy of my results, the ΔN, ΔT inversion is performed on synthetic data generated in chapter 4. The first step is to do a conventional inversion using AVOA data and see which parameter is reliable. The second step is to apply the inversion to the ratio attribute derived in chapter 4. The last step is to perform the inversion on real data using the ratio method where the overburden effect is believed to be removed.

Chapter 2: Background Theory

SEISMIC ANISOTROPY

Introduction

Seismic anisotropy is defined as "the dependence of velocity upon angle" (Thomsen, 2002). In the past, geoscientists preferred to work with simple and intuitive equations assuming isotropy of rocks. Seismic anisotropy is complex and this is the main reason it was ignored for a long time and the cost of adding the complexity of anisotropy in seismic data analysis was not justified. The advent of digital recording, long offset acquisition and better seismic data processing algorithms, have now made it possible to take into account anisotropy in seismic data processing analysis and interpretation.

Because anisotropic equations involve a large number of parameters, anisotropic processing used to be very computationally intensive. With modern powerful computers it is now possible to process and interpret data with great precision and within a reasonable time frame. For all of these reasons, seismic anisotropy has become an important subject that cannot be neglected anymore.

In this section, I review the basic theory and concepts behind seismic anisotropy and anisotropic wave propagation.

Causes of seismic anisotropy

Numerous geological processes can cause seismic anisotropy, which can be classified into three main categories (Crampin et al., 1984):

Intrinsic anisotropy

A preferred orientation of anisotropic mineral grains is called "intrinsic anisotropy" (Thomsen, 1986). This type of anisotropy is found in clay-rich shales, which comprise about 70% of sedimentary rocks (Slater, 1997). Compaction, stresses and sedimentation of flattened grains make them intrinsically anisotropic. The velocity difference along and across shale plates can be large enough to cause significant imaging problems if this effect is ignored during seismic data processing. A microscopic image of a shale formation is shown in Figure 2.1 showing what shale looks like at the grain scale. The plate-like particles are clay minerals while the larger, nearly spherical particles are silt.

Thin layering

This type of anisotropy is caused by thin (relative to seismic wavelengths) layering in rock sequences, which is commonly found in sedimentary rocks. Sand-shale sequence environments are examples of such layering. When the layering is much thinner than seismic wavelength, the sequence of isotropic layers is effectively averaged by the long seismic wavelength. For long wavelengths such thinly layered media is equivalent to a transversely isotropic (TI) homogeneous medium (Backus, 1962, Schoenberg 1980). The TI medium is discussed in more details in a later section.

Fracture-induced anisotropy

This kind of anisotropy is caused by non uniform action of stress, where the two principal horizontal stresses are not equal. This causes the rocks to crack and/or fracture where fractures are usually aligned with the dominant horizontal stress direction. Fracture-induced anisotropy plays an important role in exploring for new hydrocarbon reservoirs or managing existing ones.

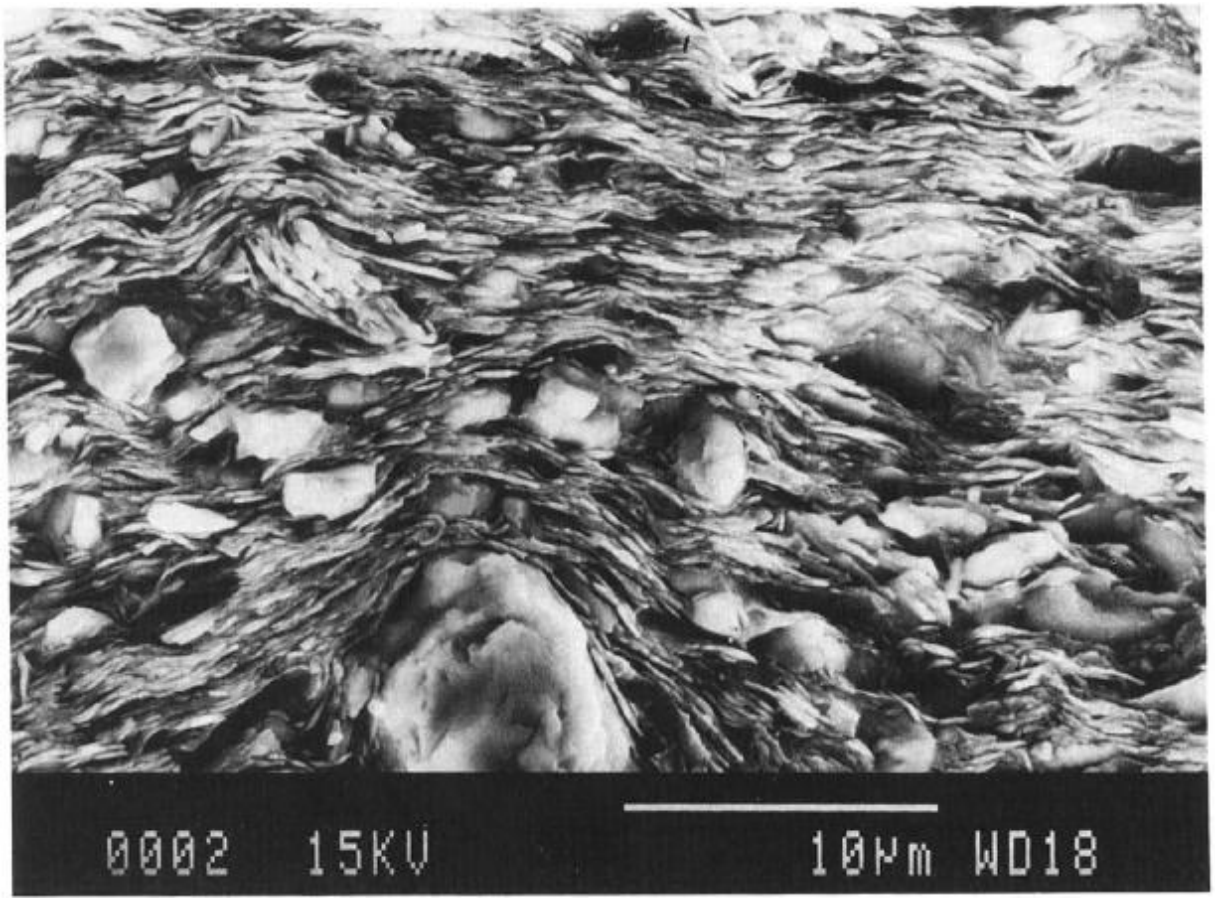

Figure 2.1: An SEM scan of a microscopic vertical section of shale showing what shale looks like at the grain scale. The plate-like particles, with predominantly horizontal orientation, are clay minerals while the larger, nearly spherical particles are silt (after Hornby et al., 1994).

Because of overburden stress and differential horizontal stress, sub-vertical or vertical fractures may open and become important for hydrocarbon exploitation. They can be a main source of permeability, especially in low porosity, tight reservoirs.

The theory of elasticity and Hooke's Law

Sheriff (1991) described elasticity as the property that enables a solid body to return to its original shape after removal of a distorting stress. The elasticity theory is very foundation of seismology because it is the elastic properties of rocks that allow seismic waves to propagate through the Earth. Stress is defined as a force per unit area, while strain is the deformation resulting from that stress. For isotropic, linear elastic material, the relationship between stress and strain can be expressed by the isotropic form of Hooke's Law as follows (Timoshenko and Goodier, 1934):

$$\sigma_{ij} = 2\mu\varepsilon_{ij} + \lambda\varepsilon_{kk}\delta_{ij}, \tag{2.1}$$

where σ_{ij} = elements of stress tensor, ε_{ij} = element of strain tensor, ε_{kk} = volumetric strain (sum over repeated indices is implied), δ_{ij} = 0 if i ≠ j, and 1 if i = j, λ and μ are called Lamé constants.

A simplified matrix form of Hooke's law for isotropic, linear elastic material can be written as follows:

$$\begin{bmatrix} \sigma_1 \\ \sigma_2 \\ \sigma_3 \\ \sigma_4 \\ \sigma_5 \\ \sigma_6 \end{bmatrix} = \begin{bmatrix} \lambda+2\mu & \lambda & \lambda & 0 & 0 & 0 \\ \lambda & \lambda+2\mu & \lambda & 0 & 0 & 0 \\ \lambda & \lambda & \lambda+2\mu & 0 & 0 & 0 \\ 0 & 0 & 0 & \lambda & 0 & 0 \\ 0 & 0 & 0 & 0 & \lambda & 0 \\ 0 & 0 & 0 & 0 & 0 & \lambda \end{bmatrix} \times \begin{bmatrix} \varepsilon_{11} \\ \varepsilon_{22} \\ \varepsilon_{33} \\ 2\varepsilon_{23} \\ 2\varepsilon_{31} \\ 2\varepsilon_{12} \end{bmatrix}. \tag{2.2}$$

The Hooke's law for general anisotropic, linear elastic solids states that the stress is linearly proportional to the strain (Mavko et al., 1998),

$$\sigma_{ij} = c_{ijkl}\varepsilon_{kl} \ . \tag{2.3}$$

The summation is implied over the repeated subscripts *k* and *l*. c_{ijkl} is called the elastic stiffness tensor, which has a total of eighty-one components and is a fourth rank tensor. Fortunately, not all of the 81 components are independent, due to the symmetry of stress and strain, which implies that: $c_{ijkl} = c_{jikl} = c_{ijlk} = c_{jilk}$ resulting in only thirty-six independent constants. Due to strain energy considerations where $c_{ijkl} = c_{klij}$ the total number of independent constants further reduces to twenty-one.

Because of the symmetry of stress and strain tensers, the fourth-order elasticity tensor can be represented by a two dimensional matrix. As a result, the 3x3x3x3 tensor is replaced by a 6x 6 matrix as follows (Mavko et al., 1998; Thomsen, 2002):

$$C_{ij} = \begin{bmatrix} C_{11} C_{12} C_{13} C_{14} C_{15} C_{16} \\ C_{21} C_{22} C_{23} C_{24} C_{25} C_{26} \\ C_{31} C_{32} C_{33} C_{34} C_{35} C_{36} \\ C_{41} C_{42} C_{43} C_{44} C_{45} C_{46} \\ C_{51} C_{52} C_{53} C_{54} C_{55} C_{56} \\ C_{61} C_{62} C_{63} C_{64} C_{65} C_{66} \end{bmatrix}. \tag{2.4}$$

The independent constants are further reduced to only 21 because of the symmetry about the main diagonal. In the most general case of anisotropy where 21 independent matrix elements are needed, it is almost impossible to measure them in any

geophysical field survey. The good news is that what we observe in seismic data is generally much simpler at the expense of not having enough directionally dependent properties

Symmetry classes

Due to the symmetry in any material, the total number of elastic constants is reduced proportionally to the degree of symmetry. The most general one is called triclinic where there are 21 independent parameters. In this section I will discuss two symmetry classes: Isotropic symmetry and transverse isotropy.

Isotropic symmetry

In the isotropic symmetry case both P-wave and S-wave velocities are the same in all directions. This simple and unique kind of symmetry results in reducing the number of independent elastic constants to only two. The resulting stiffness matrix is as follows:

$$C_{ij=}\begin{bmatrix} C_{11} & C_{12} & C_{12} & 0 & 0 & 0 \\ C_{12} & C_{11} & C_{12} & 0 & 0 & 0 \\ C_{12} & C_{12} & C_{11} & 0 & 0 & 0 \\ 0 & 0 & 0 & C_{44} & 0 & 0 \\ 0 & 0 & 0 & 0 & C_{44} & 0 \\ 0 & 0 & 0 & 0 & 0 & C_{44} \end{bmatrix}, C_{12} = C_{11} - 2C_{44}. \qquad (2.5)$$

Lamé's parameters λ and μ are directly related to C_{ij} elements according to these equations:

$$C_{11} = \lambda + 2\mu, C_{44} = \mu, C_{12} = \lambda\,. \qquad (2.6)$$

Transverse isotropy

Shale formations, which comprise about 70% of sedimentary rocks, have a transverse isotropic (TI) symmetry, and that is why TI medium is the most common anisotropic model in exploration seismology (Tsvankin, 2001). Transverse isotropy is classified according to the symmetry axis which is the axis where seismic properties are rotationally invariant. In the case of vertical axis of symmetry, we have vertical transverse isotropy (VTI). Shale formations represent VTI media. If the axis of symmetry is rotated from vertical to horizontal, this results in a horizontal transverse isotropy or a HTI medium. A more complicated type of anisotropy is called orthorhombic, which is a combination of VTI and HTI. All three types are shown in Figure 2.2. The TI media requires five independent elastic constants.

Vertical transverse isotropy (VTI)

This kind of TI medium can also be called polar anisotropy (Thomsen, 2002). The stiffness matrix for a VTI medium is (Mavko et al., 1998):

$$C^{(VTI)}_{ij=}\begin{bmatrix} C_{11} & C_{12} & C_{13} & 0 & 0 & 0 \\ C_{12} & C_{11} & C_{13} & 0 & 0 & 0 \\ C_{13} & C_{13} & C_{33} & 0 & 0 & 0 \\ 0 & 0 & 0 & C_{44} & 0 & 0 \\ 0 & 0 & 0 & 0 & C_{44} & 0 \\ 0 & 0 & 0 & 0 & 0 & C_{66} \end{bmatrix}, C_{66} = \frac{1}{2}(C_{11} - C_{12}). \qquad (2.7)$$

Horizontal transverse isotropy (HTI)

The stiffness matrix for a HTI medium is:

$$C^{(HTI)}_{ij=}\begin{bmatrix} C_{11} & C_{13} & C_{13} & 0 & 0 & 0 \\ C_{13} & C_{33} & C_{33}-2C_{44} & 0 & 0 & 0 \\ C_{13} & C_{33}-2C_{44} & C_{33} & 0 & 0 & 0 \\ 0 & 0 & 0 & C_{44} & 0 & 0 \\ 0 & 0 & 0 & 0 & C_{55} & 0 \\ 0 & 0 & 0 & 0 & 0 & C_{55} \end{bmatrix}. \qquad (2.8)$$

As it can be seen in equation 2.8, an HTI medium has five independent elastic constants and another common name for this kind of symmetry is azimuthally anisotropic medium with horizontal axis of symmetry. Naturally occurring fracture systems in the Earth is the most common cause of azimuthal anisotropy where seismic properties vary with azimuth. An HTI medium is used to represent reservoirs with one set of vertical fractures. Inverting for HTI elastic constants results in gaining information about the orientation of fractures, their density and the nature of crack in-fill.

Figure 2.3 shows a sketch of an HTI model where the symmetry axis is horizontal and the [x1,x3]-plane is called the symmetry plane. Shear-wave splitting, or birefringence, is caused by fracture-induced azimuthal anisotropy and can be seen in figure 2.3 where the vertically traveling S-wave splits into two polarized waves: one has particle motion parallel to the fractures (polarized within the isotropy plane) travelling with relatively fast velocity ($S^{\parallel}$) and the other has particle motion perpendicular to the fracture (polarized within the symmetry-axis plane) with relatively slower velocity ($S^{\perp}$) (Martin and Davis, 1987; Rüger, 1996).

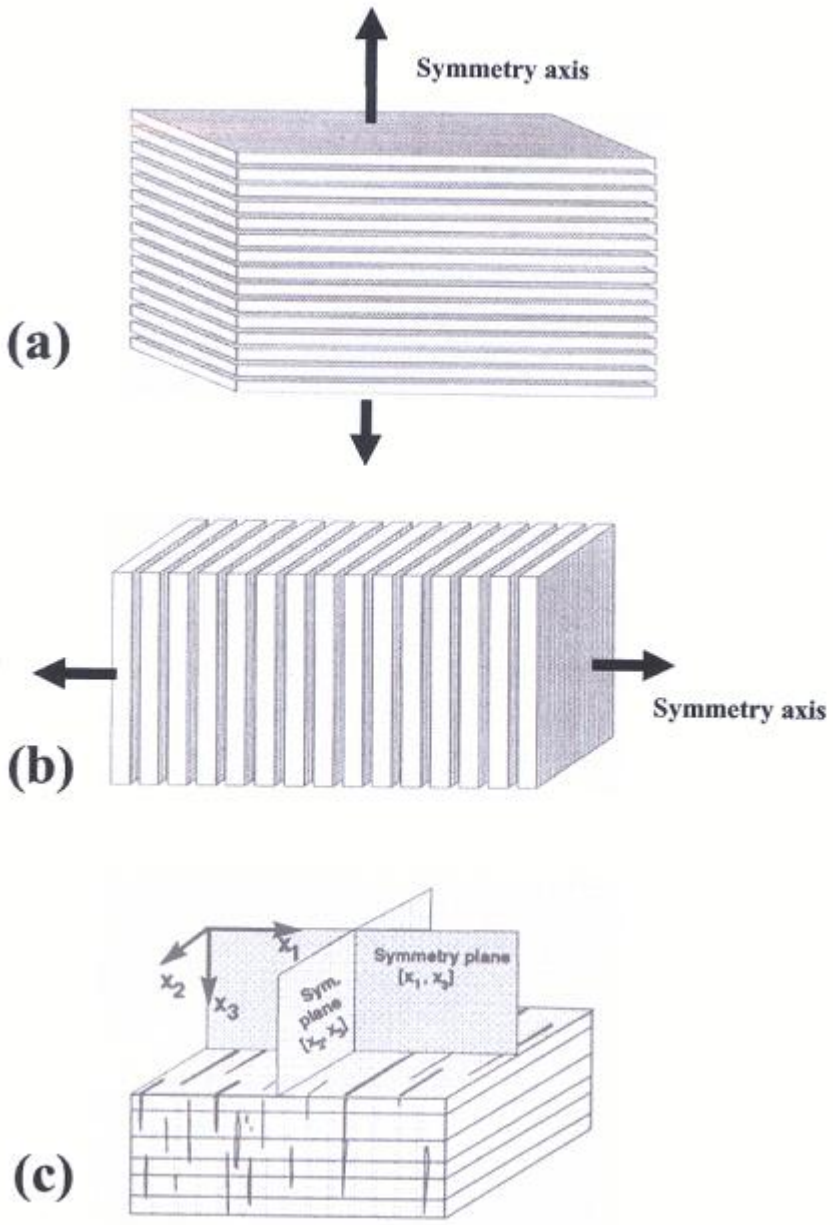

Figure 2.2: Illustrations of three anisotropic media with different axes of symmetry. (a) Transverse isotropy with vertical symmetry (VTI), (b) transverse isotropy with horizontal symmetry (HTI) and (c) orthorhombic anisotropy with two sets of symmetrical planes (after Rüger, 1996).

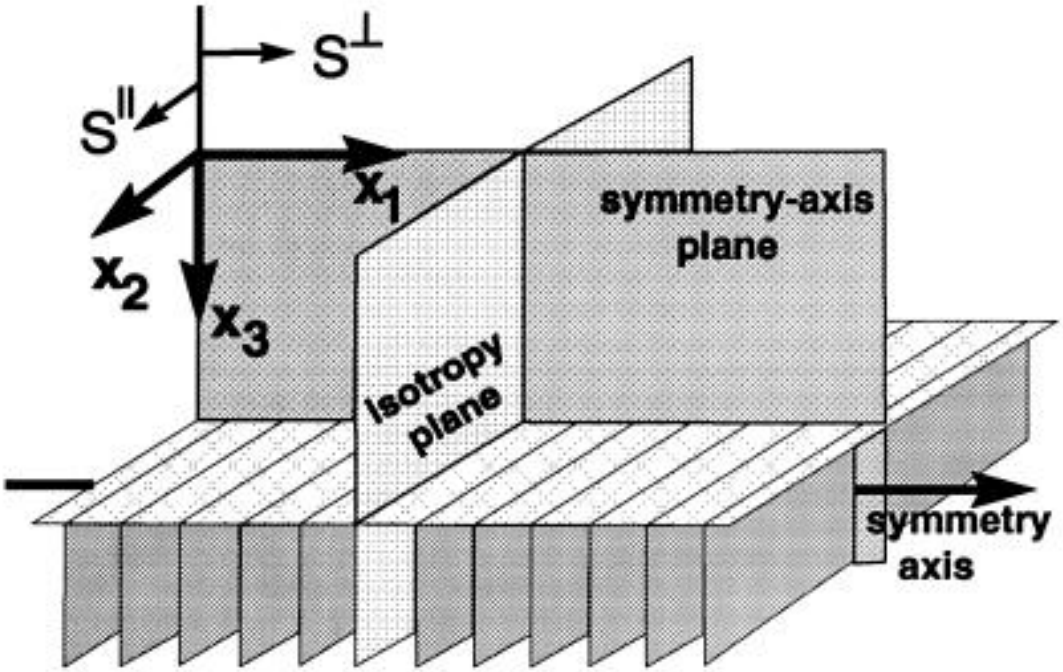

Figure 2.3: HTI model due to a system of parallel vertical cracks. Vertically travelling shear waves in HTI media split into two modes polarization parallel $S^{\parallel}$ and perpendicular $S^{\perp}$ to the crack faces (after Rüger, 1996).

THEORY OF TRANSMISSION AND REFLECTION

Partitioning of energy at an interface

When an elastic wave propagating through a solid reaches a boundary with another solid of different properties, it will partly reflect off the boundary at some angle and partly pass through it, but has a different direction after interaction with the boundary. Zoeppritz (1919) published the solution to the reflection and transmission of plane waves at a plane boundary between two isotropic elastic media. In his derivation of what is now called "The Zoeppritz equations", he assumed the continuity of stress and displacement across the reflecting boundary. The incident P-wave on a boundary between two layers of different velocities and densities will give rise to a reflected P-wave, a reflected S-wave, a transmitted P-wave and a transmitted S-wave. The difference in velocities and densities between the upper and lower layers (1 and 2) cause the angle of reflected P-wave (φ_1) energy to differ from the angle of transmitted P-wave energy (φ_2). Similarly, the reflection angle of the S-wave energy (ψ_1) is different from the angle of the transmitted S-wave energy (ψ_2) (Figure 2.4).

It is often convenient to work with displacement potentials instead of the displacement vector **u** when dealing with wave propagation problems (Officer, 1958). The two displacement potentials are defined as a P-wave potential (Φ) and an S-wave potential (Ψ) in terms of the displacement u and w as:

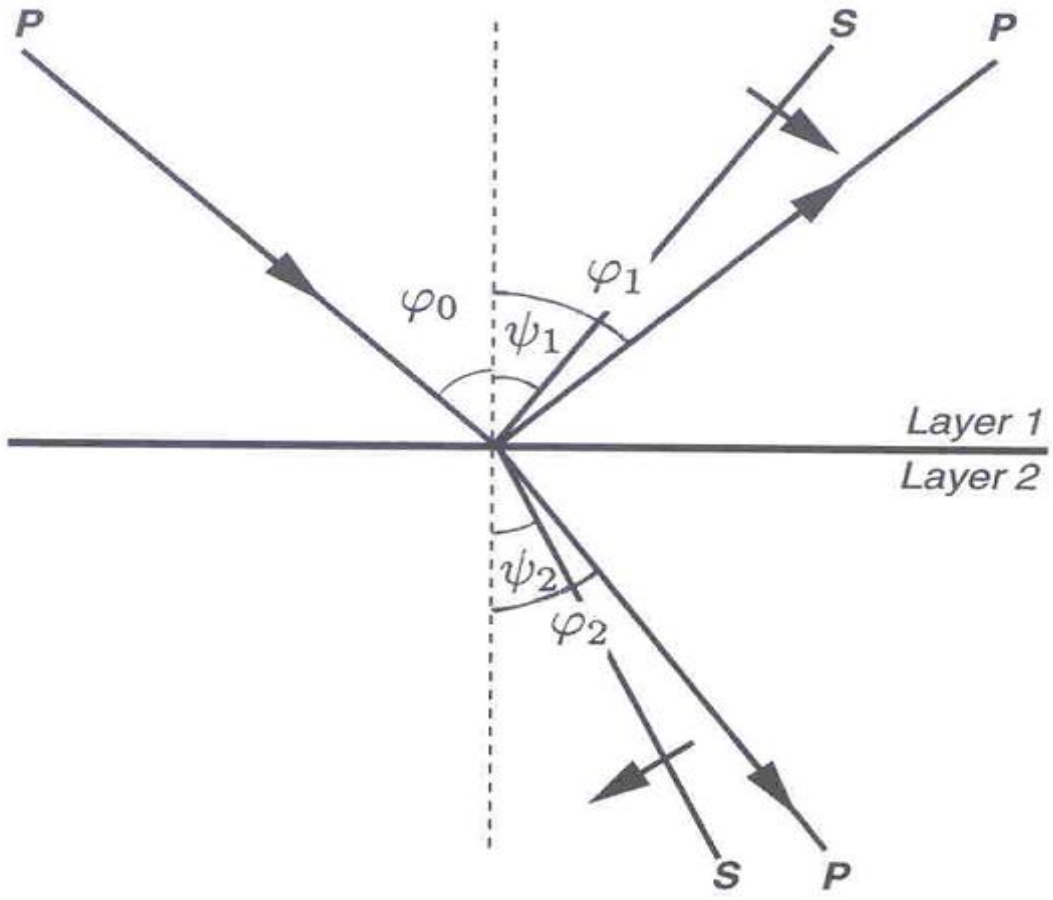

Figure 2.4: Incident P-wave and associated reflected and transmitted P- and S-waves. The arrows indicate the difference between reflected and transmitted angles (after Yilmaz, 2001).

$$u = \frac{\partial \Phi}{\partial x} + \frac{\partial \Psi}{\partial z}, \tag{2.9}$$

$$w = \frac{\partial \Phi}{\partial z} - \frac{\partial \Psi}{\partial x}. \tag{2.10}$$

There are four important boundary conditions used to derive Zoeppritz's equations:

1 .The displacement component tangential to the interface is continuous: $u_1 = u_2$.

2. The displacement component normal to the interface is continuous: $w_1 = w_2$.

3. The stress component normal to the interface is continuous: $(P_{zz})_1 = (P_{zz})_2$.

4. The stress component tangential to the interface is continuous: $(P_{xz})_1 = (P_{xz})_2$.

Each of these boundary conditions is used to derive one equation and in total we have four equations known as the Zoeppritz's equations, which are expressed in matrix form as follows (Yilmaz, 2001):

$$\begin{bmatrix} \cos\varphi_1 & \frac{\alpha_1}{\beta_1}\sin\psi_1 & \frac{\alpha_1}{\beta_{21}}\cos\varphi_2 & -\frac{\alpha_1}{\beta_2}\sin\psi_2 \\ -\sin\varphi_1 & \frac{\alpha_1}{\beta_1}\cos\psi_1 & \frac{\alpha_1}{\beta_{21}}\sin\varphi_2 & \frac{\alpha_1}{\beta_2}\cos\psi_2 \\ -\cos 2\psi_1 & -\sin 2\psi_1 & \frac{\rho_2}{\rho_1}\cos 2\psi_2 & -\frac{\rho_2}{\rho_1}\sin 2\psi_2 \\ \sin 2\varphi_1 & -\frac{\alpha^2{}_1}{\beta^2{}_1}\cos 2\psi_1 & \frac{\rho_2\beta_2{}^2\alpha_1{}^2}{\rho_1\beta_1{}^2\alpha_2{}^2}\sin 2\varphi_2 & \frac{\rho_2\alpha_1{}^2}{\rho_1\beta_1{}^2}\cos 2\psi_2 \end{bmatrix} \begin{bmatrix} A_1 \\ B_1 \\ A_2 \\ B_2 \end{bmatrix} = \begin{bmatrix} \cos\varphi_1 \\ \sin\varphi_1 \\ \cos 2\psi_1 \\ \sin 2\varphi_1 \end{bmatrix} \tag{2.11}$$

where A_1, B_1, A_2, B_2 are the reflected P-wave, reflected S-wave, transmitted P-wave, and transmitted S-wave, ψ_1, ψ_2 φ_1 and φ_2 are angles denoted in figure 2.4, ρ is density, α is P-wave velocity and β is S-wave velocity. 1 and 2 denote the upper and lower media.

Amplitude variation with offset in isotropic media

Zoeppritz's equations relate reflection coefficients as a function of the angle of incidence to medium physical parameters. For that reason, Zoeppritz's equations are the building blocks for AVO analysis. Algebraic complexity and a requirement for information usually not available made the Zoeppritz's equations impractical for AVO analysis. Therefore, conventional AVO analysis is mostly based on approximate analytic expressions for reflection coefficients.

Bortfeld (1961) was the first to approximate Zoeppritz equations for P-to-P reflection amplitude, which is given as:

$$R(\varphi_1) = \frac{1}{2}\ln\left(\frac{\alpha_2\rho_2\cos\varphi_2}{\alpha_1\rho_1\cos\varphi_1}\right) + \left(2 + \frac{\ln\left(\frac{\rho_2}{\rho_1}\right)}{\ln\left(\frac{\alpha_2}{\alpha_1}\right) - \ln\left(\frac{\alpha_2\beta_1}{\alpha_1\beta_2}\right)}\right)\frac{\beta^2{}_1 - \beta^2{}_2}{\alpha^2{}_1}\sin^2\varphi_1, \qquad (2.12)$$

where φ_1 and φ_2 are incident and transmitted angles respectively, α is P-wave velocity, β is S-wave velocity, ρ is density, the subscripts 1 and 2 denote the upper and lower media.

In his approximation, Bortfeld arranged the equation into two terms separating the acoustic and the elastic effects on reflection amplitudes but its practical implementation for AVO analysis was not considered because it does not explicitly indicate angle or

offset dependence of reflection amplitudes (Yilmaz, 2001). A practical method for routine application of AVO analysis was possible after the introduction of the Aki-Richard's approximation assuming that changes in elastic properties of rocks across the layer boundary are small and propagation angles are within the sub-critical range (Aki and Richard, 1980). The resulting equation can be written as follows:

$$R(\theta)=\left[\frac{1}{2}\left(1+\tan^2\theta\right)\right]\frac{\Delta\alpha}{\alpha}-\left[4\frac{\beta^2}{\alpha^2}\sin^2\theta\right]\frac{\Delta\beta}{\beta}+\left[\frac{1}{2}\left(1-4\frac{\beta^2}{\alpha^2}\sin^2\theta\right)\right]\frac{\Delta\rho}{\rho}, \tag{2.13}$$

where $\alpha=(\alpha_1+\alpha_2)/2$, average P-wave velocity and $\Delta\alpha=(\alpha_2-\alpha_1)$, $\beta=(\beta_1+\beta_2)/2$, average S-wave velocity and $\Delta\beta=\beta_2-\beta_1$, $\rho=(\rho_1+\rho_2)/2$, average density and $\Delta\rho=\rho_2-\rho_1$, and $\theta=(\varphi_1+\varphi_2)/2$, average of the incidence and transmission angles for the P-wave.

Shuey (1985) derived a more practical form of Aki-Richards equation in terms of contrasts in the P-wave velocity, density and Poisson's ration. The same form can be obtained if the contrasts in P-wave velocity, S-wave velocity and density are used as perturbation parameters. This leads to:

$$R(\theta)=A+B\sin^2\theta+C(\tan^2\theta\sin^2\theta), \tag{2.14}$$

where

$$A=\left[\frac{1}{2}\left(\frac{\Delta\alpha}{\alpha}+\frac{\Delta\rho}{\rho}\right)\right],$$

$$B=\left[\frac{1}{2}\frac{\Delta\alpha}{\alpha}-4\frac{\beta^2}{\alpha^2}\frac{\Delta\beta}{\beta}-2\frac{\beta^2}{\alpha^2}\frac{\Delta\rho}{\rho}\right],$$

$$C=\left[\frac{1}{2}\frac{\Delta\alpha}{\alpha}\right],$$

A is called the intercept, B is the gradient and C is the curvature term usually dealing with large incident angles. In most routine applications, the higher-order $\tan^2\theta\sin^2\theta$ term is generally ignored.

Amplitude variation with offset in azimuthally anisotropic media

Reflection coefficient approximations given by Bortfeld (1961), Aki and Richards (1980), and Shuey (1985) (equations 2.12 to 2.14) are for solely isotropic materials, and thus do not account for anisotropy. Vertical fractures, which often cause azimuthal anisotropy, affect hydrocarbon flow in reservoirs. For that reason, it is useful to include azimuthal anisotropy into calculations of reflection amplitudes. Interpreting AVO results assuming the isotropy of rocks could result in significant errors in the presence of anisotropy (Teng and Mavko, 1996).

Plane waves in HTI medium

If a plane P-wave is propagating through on an HTI medium outside of the symmetry-axis and isotropy plane, three plane waves are generated. The first one is a P-wave polarized approximately along its propagation direction. The second and third are two S-waves, one is polarized within the isotropy plane, referred to as S-parallel ($S^{\parallel}$), and the other one is polarized in the symmetry axis, referred to as S perpendicular ($S^{\perp}$), Polarization of S-waves in the direction parallel and perpendicular to fractures (S-wave birefringence) is often used as a valuable tool for estimating fracture properties in fractured reservoir exploration and development (Martin and Davis, 1987).

Rüger's approximations

Analysis of amplitude variations with offset and azimuth (AVOA), often caused by vertical fractures is an important tool in inferring medium elastic parameters from surface seismic. For long wavelengths, a fractured reservoir can be represented by the HTI model. The PP-wave reflection coefficient, R, at a horizontal interface between isotropic and HTI media is defined by the approximate formula (Rüger, 1996):

$$R_p(i,\phi) = A + B\sin^2 i + C\sin^2 i \tan^2 i ,$$

$$A = \frac{1}{2}\frac{\Delta Z}{\overline{Z}},$$

$$B = \frac{1}{2}\left\{\frac{\Delta\alpha}{\overline{\alpha}} - \left(\frac{2\overline{\beta}}{\overline{\alpha}}\right)^2 \frac{\Delta G}{\overline{G}} + \left[\Delta\delta^{v} + 2\left(\frac{2\overline{\beta}}{\overline{\alpha}}\right)\Delta\gamma\right]\cos^2\phi\right\},$$

$$C = \frac{1}{2}\left\{\frac{\Delta\alpha}{\overline{\alpha}} + \Delta\varepsilon^{v}\cos^4\phi + \Delta\delta^{v}\sin^2\phi\cos^2\phi\right\}, \qquad (2.15)$$

where i is the angle between the slowness vector of the incident wave and the vertical, ϕ is the azimuthal angle defined with respect to the symmetry axis pointing in the x_1-direction (see Figure 2.5), $Z = \rho\alpha$ is the vertical P-wave impedance and $G = \rho\beta^2$ is the vertical shear modulus. A and B are called the intercept and gradient respectively. C is called the curvature term. The elastic parameters are expressed through their average values and relative differences across the interface. The vertical P-wave velocities in the upper and lower layers, for example, can be written as functions of the average velocity $\overline{\alpha} = \frac{1}{2}(\alpha_2 + \alpha_1)$ and the difference $\Delta\alpha = (\alpha_2 - \alpha_1)$. Corresponding expressions are defined for the shear modulus, the density and the P-wave impedance.

The superscript "*v*" in equation 2.15 emphasizes that the coefficients are computed with respect to the vertical and correspond to the equivalent HTI model that describes wave propagation in the symmetry-axis plane. A more intuitive form of Rüger's approximation is:

$$R(i,\phi) = A + B(\phi)\sin^2 i + C(\phi)\sin^2 i \tan^2 i \tag{2.16}$$

The term A is the normal-incidence reflection coefficient or intercept. The term $B(\phi)$ is so-called AVO gradient,which can be written as:

$$B(\phi) = B_{iso} + B_{ani}\cos^2(\phi - \phi_{sym}) \tag{2.17}$$

The symmetry axis forms an angle ϕ_{sym} with the x-axis. The term B_{iso} is the AVO-gradient isotropic part (equal to the AVO gradient for isotropic media), and B_{ani} is the anisotropic part of AVO gradient:

$$B_{iso} = \frac{1}{2}\left[\frac{\Delta\alpha}{\alpha} - \left(\frac{2\overline{\beta}}{\overline{\alpha}}\right)^2 \frac{\Delta G}{\overline{G}}\right], \tag{2.18}$$

and

$$B_{ani} = \frac{1}{2}\left[\Delta\delta^{v} + 2\left(\frac{2\overline{\beta}}{\overline{\alpha}}\right)\Delta\gamma\right]. \tag{2.19}$$

The shape of the variation of AVO gradients with azimuth is determined by both B_{iso} and B_{ani} (Rüger, 1996). A parallel direction to the fractures corresponds to only B_{iso}, while a perpendicular direction corresponds to $B_{iso} + B_{ani}$.

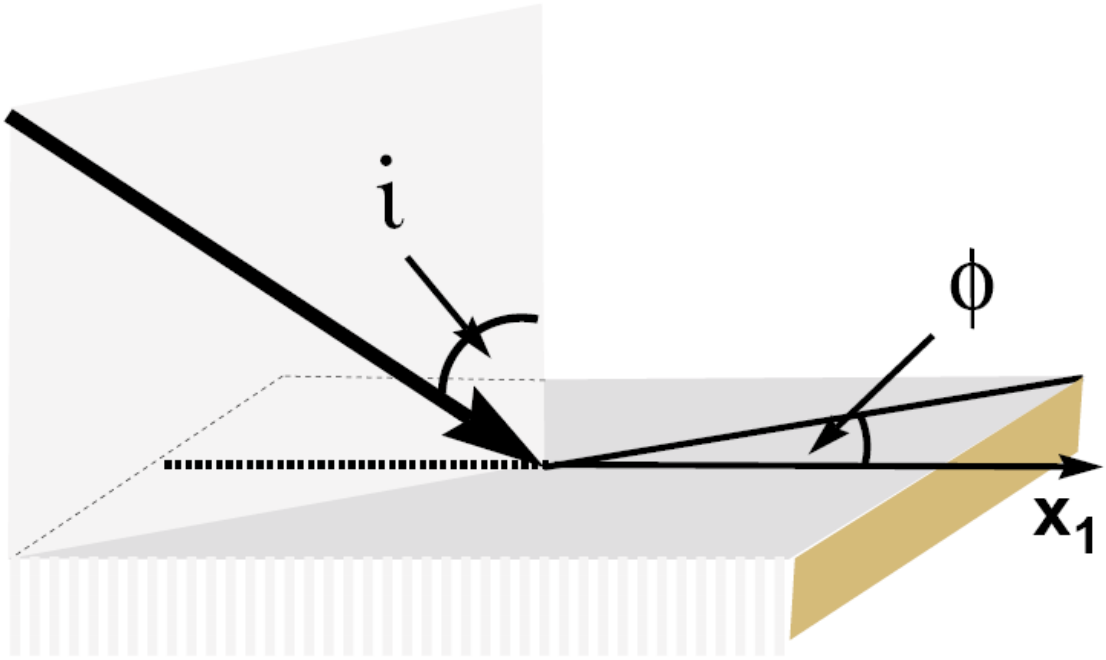

Figure 2.5: Reflection response for vertically fractured reservoir (HTI media) as a function of incidence angle i and azimuth ∅ (after Rüger, 1996).

NATURALLY FRACTURED RESERVOIRS

A fracture is a discontinuity or parting in a material caused by brittle failure (Wayne et. al, 2006). "Fracture" is a general term that includes various natural and induced features where the two principal naturally occurring fracture types are joints and faults (Figure 2.6). The orientation of fractures is controlled predominantly by the orientation of the Earth's stress field, which varies in direction and magnitude with location.

An important parameter of a fracture set is the distance between the adjacent fractures. Fracture intensity is one other parameter usually used by geologists,

Fracture intensity = number of fractures / unit length,

where the number of fractures are counted in the direction perpendicular to the fracture planes. Fracture intensity is usually replaced by a similar parameter called the crack density (Bakulin et. al, 2000a), given by $e = \xi a^3$, where ξ is the number of cracks per unit volume and a is the average crack radius.

Seismic wavelengths are usually much larger than fracture spacing. Fracture spacing also considered to be much larger than fracture opening. For these reasons, in building fracture models, the finite fracture opening and details of the spatial distributions of fractures are usually neglected. Therefore, fractured blocks are replaced by equivalent or effective anisotropic solids. Such models are controlled by four parameters: fracture orientation, fracture density, material filling the fractures and the elastic coefficients of the host rock (Bakulin et. al, 2000a).

Nelson (2001) classifies fractured reservoirs in the following way:

Type 1: Fractures provide the essential reservoir porosity and permeability.

Type 2: Fractures provide the essential reservoir permeability. However, the matrix porosity is several orders of magnitude greater than fracture volume.

Type 3: Fractures assist permeability in an already producible reservoir.

In this dissertation, I study seismic data from an Oil field in the Arabian Peninsula, which is classified as a type 3 reservoir.

The earth is complicated, and in an ideal case we need a large number of parameters to truly describe its heterogeneity. As an alternative approach, a complicated earth model is replaced by a simplified equivalent medium where fewer parameters are used. This process is called homogenization, which is the basis of all effective-medium theories. There exist several different effective medium models to represent the reservoirs in the seismic frequency band.

Model building

The integration of various data types is usually performed in industry practice because deriving a realistic reservoir model is very complex and requires information from structural geology, well data, seismic and production data. Structural geology information can describe the reservoir at a coarse scale, failing to give detailed reservoir properties like porosity or fracture density, especially when reservoir units have undergone a complex tectonic history. On the other hand, production data, well logs and cores give a detailed description of reservoir only at the well locations. In between and away from wells, seismic methods can aid the interpolation of valuable information on reservoir properties.

In my research, I attempt to use P-P pre-stack seismic data to characterize a fractured carbonate reservoir in The Arabian Peninsula and compare my results at the well locations.

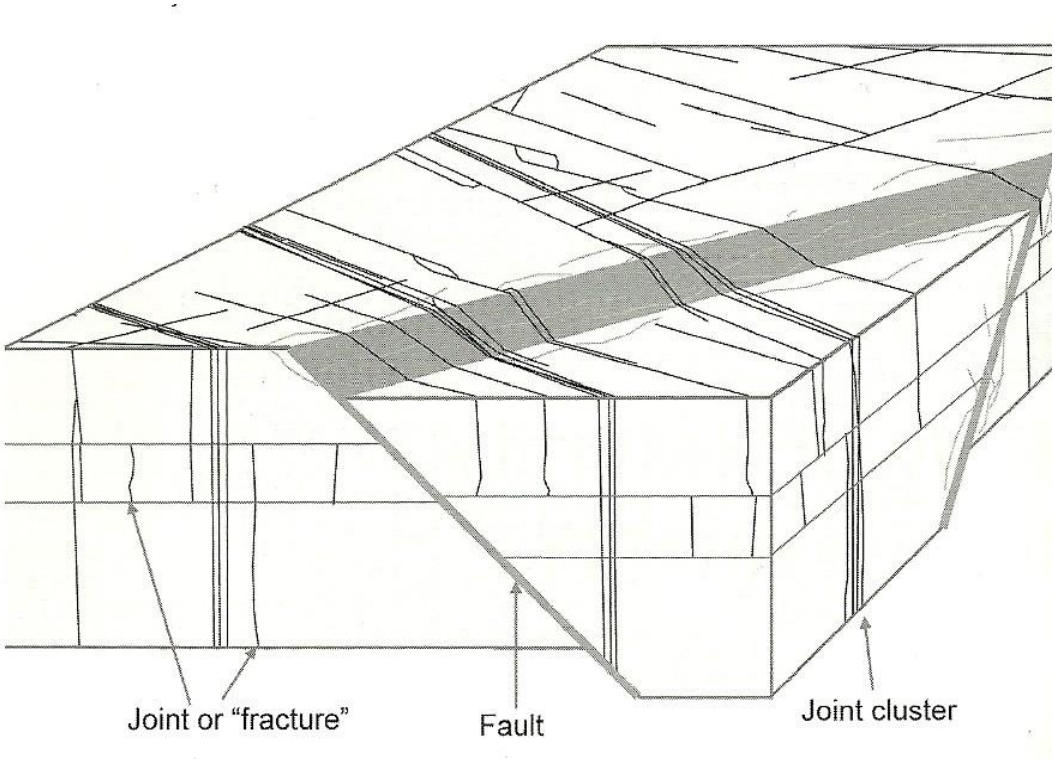

Figure 2.6: Conceptual view of fractured sandstone showing joints, joint cluster and a fault (After Wayne et. al, 2006).

Seismic methods for fracture characterization

Traveltime and amplitude are the two main azimuthal attributes of reflected waves often used to characterize reservoirs that contain vertical fractures. These attributes can provide valuable information about anisotropy associated with natural fracture systems (Tsvankin et al., 2010).

1. Traveltime: Moveout analysis of wide-azimuth data is based on the concept of the NMO ellipse and on the generalized Dix-type averaging equations (Grechka and Tsvankin, 1998). The normal moveout velocity expressed as a function of the azimuth α of the CMP line is given by the following quadratic form:

$$\frac{1}{V^2}(\alpha) = W_{11}cos^2\alpha + 2W_{12}sin\alpha\, cos\alpha + W_{22}sin^2\alpha \quad , \qquad (2.20)$$

where W is a symmetric 2x2 matrix determined by the medium properties oriented around the zero-offset ray.

2. Amplitude: Amplitude variation with incidence angle and azimuth (AVOA) can achieve a much higher vertical resolution than traveltime methods because reflection coefficients are determined by the elastic properties averaged on the scale of seismic wavelength (Tsvankin et al., 2010). Much effort has been devoted to the development of anisotropic reflection coefficients (e.g., Rüger and Tsvankin, 1997; Sayers and Rickett, 1997; Montoya et al., 2002) and characterization of AVOA. Rüger (1998) offered an analytic approximation to reflection coefficients in azimuthally anisotropic media and presented a simple method for exploiting AVOA to characterize fractures. Al-Marzoug et al. (2006) and Balharith (2009) successfully applied AVOA method to 3-D seismic data set in The Arabian Peninsula.

ROCK PHYSICS MODELS

Static fractured models

The most important assumption in the derivation of static models is that the fractures are hydraulically isolated and in the case of saturated models, there is no exchange of fluids neither between fractures themselves nor between fractures and the background matrix. The resultant effective elastic coefficients are frequency independent. Two static fracture models are discussed below in more details:

1. The linear slip model

Schoenberg (1980, 1983) estimated the effective parameters of fractured media by assuming the fractures to be either infinitely thin and highly compliant layers or planes of weakness with linear slip boundary conditions. Fracture shape and microstructure were ignored in his derivation. The first derivation was made using exact Backus (1962) averaging procedure for parallel thin, soft layers embedded in an isotropic matrix leading to the conclusion that the effective compliance matrix is the sum of the compliance matrix of the background and the compliance matrix of fractures or excess compliance.

$$S = S_b + S_f, \tag{2.21}$$

where S_b is the compliance matrix of the host rock and S_f is the excess compliance associated with the fractures (Schoenberg and Muir, 1989). According to Schoenberg and Douma (1988), for perfectly aligned and rotationally invariant fractures (no coupling between the slips along the coordinate directions and a purely isotropic microstructure of the fracture surfaces), the matrix of fracture compliance is given by:

$$s_f = \begin{bmatrix} K_N & 0 & 0 & 0 & 0 & 0 \\ 0 & 0 & 0 & 0 & 0 & 0 \\ 0 & 0 & 0 & 0 & 0 & 0 \\ 0 & 0 & 0 & 0 & 0 & 0 \\ 0 & 0 & 0 & 0 & K_T & 0 \\ 0 & 0 & 0 & 0 & 0 & K_T \end{bmatrix} . \tag{2.22}$$

The values K_N and K_T are nonnegative and have the physical meaning of the normal and tangential compliances added linearly to the host rock. Two dimensionless quantities Δ_N and Δ_T were introduced by Hsu and Schoenberg (1993). They are denoted by normal and tangential weaknesses respectively. Where:

$$\Delta_N = \frac{(\lambda + 2\mu)K_N}{1 + (\lambda + 2\mu)K_N}, \tag{2.23}$$

and,

$$\Delta_T = \frac{\mu K_T}{1 + \mu K_T} . \tag{2.24}$$

were λ and μ are the Lamé constant for the isotropic host rock.

The stiffness matrix of a vertically fractured effective medium can be explicitly written in terms of the Lamé parameters of the host background matrix and weaknesses as follows (Schoenberg and Sayers, 1995):

$$C = S^{-1} = C_b - \begin{bmatrix} (\lambda + 2\mu)\Delta_N & \lambda\Delta_N & \lambda\Delta_N & 0 & 0 & 0 \\ \lambda\Delta_N & \frac{\lambda^2}{\lambda + 2\mu}\Delta_N & \frac{\lambda^2}{\lambda + 2\mu}\Delta_N & 0 & 0 & 0 \\ \lambda\Delta_N & \frac{\lambda^2}{\lambda + 2\mu}\Delta_N & \frac{\lambda^2}{\lambda + 2\mu}\Delta_N & 0 & 0 & 0 \\ 0 & 0 & 0 & 0 & 0 & 0 \\ 0 & 0 & 0 & 0 & \mu\Delta_T & 0 \\ 0 & 0 & 0 & 0 & 0 & \mu\Delta_T \end{bmatrix} . \tag{2.25}$$

2. Penny-shaped crack model

Hudson's (1980) model is based on scattering-theory analysis of the mean wave-field in an elastic solid with thin, isolated, penny-shaped ellipsoidal cracks or inclusions filled with a weak material. In other words, the model is based on smoothing by averaging equations of motion over the cracks.

The model describes a material containing embedded thin cracks. The solid matrix is assumed to be isotropic, while the overall elastic properties become anisotropic if the orientations of the cracks are not random. Crack density is assumed to be low, and the crack diameter is assumed to be much smaller than the acoustic wavelength. It is assumed that the cracks are not hydraulically connected, and there is no possibility for fluid flow into or out of the volume containing the cracks.

For penny-shaped cracks orthogonal to the x1-axis, Hudson (1980, 1981) derived the following expression for the stiffness matrix C for the effective medium:

$$C = C_b - \frac{e}{\mu}\begin{bmatrix} (\lambda+2\mu)^2 U_{11} & \lambda(\lambda+2\mu)U_{11} & \lambda(\lambda+2\mu)U_{11} & 0 & 0 & 0 \\ \lambda(\lambda+2\mu)U_{11} & \lambda^2 U_{11} & \lambda^2 U_{11} & 0 & 0 & 0 \\ \lambda(\lambda+2\mu)U_{11} & \lambda^2 U_{11} & \lambda^2 U_{11} & 0 & 0 & 0 \\ 0 & 0 & 0 & 0 & 0 & 0 \\ 0 & 0 & 0 & 0 & \mu^2 U_{33} & 0 \\ 0 & 0 & 0 & 0 & 0 & \mu^2 U_{33} \end{bmatrix} + O(e^2) \tag{2.25}$$

where e is fracture density and U_{11} and U_{33} are dimensionless quantities defined as follows (Mavko et. al, 2009):

$$U_{11} = \frac{16(\lambda+2\mu)}{3(3\lambda+4\mu)} \text{ and } U_{33} = \frac{4(\lambda+2\mu)}{3(\lambda+\mu)} \text{ (for dry cracks),} \tag{2.26}$$

$$U_{11} = \frac{16(\lambda + 2\mu)}{3(3\lambda + 4\mu)} \text{ and } U_{33} = 0 \quad \text{(for infinitely thin, fluid-filled cracks).} \tag{2.27}$$

3. The relationship between Schoenberg and Hudson models

According to Schoenberg and Douma (1988) both models are very similar where both effective elastic matrices have the same structure and become identical if the fracture weaknesses satisfy the following relations:

$$\Delta_N = \frac{(\lambda + 2\mu)}{\mu} U_{11} e \text{ and } \Delta_T = U_{33} e\,; \tag{2.28}$$

These relations can be used to obtain explicit expressions for the weakness for dry and fluid-filled cracks indicated by Schoenberg and Douma (1988):

$$\Delta_N = \frac{4e}{3g(1-g)} \text{ and } \Delta_T = \frac{16e}{3(3-2g)} \quad \text{(for dry cracks)}\,, \tag{2.29}$$

$$\Delta_N = 0 \text{ and } \Delta_T = \frac{16e}{3(3-2g)} \quad \text{(for fluid-filled cracks),} \tag{2.30}$$

where the parameter g is defined as:

$$g = \frac{V_S^2}{V_P^2} = \frac{\mu}{\lambda + 2\mu}\,. \tag{2.31}$$

QUASI-STATIC POROUS FRACTURED MODEL

Gurevich (2003) derived explicit analytical expressions for low-frequency elastic constants and anisotropy parameters of a fractured porous medium saturated with a given fluid. The model assumes that the background medium is embedded with one set of vertical fractures. The five elastic constants of the resultant transversely isotropic (TI) medium are derived as a function of the properties of the dry (isotropic) background porous matrix, fracture properties and fluid bulk modulus. The derivation is based on the combination of the anisotropic form of Gassmann (1951) equation and the linear-slip model (Schoenberg, 1980).

The saturated rock elastic constants are given by:

$$C_{11}^{sat} = \frac{L}{D}\left\{ d_1\theta + \frac{K_f}{\phi K_g L}\left[L_1\alpha' - \frac{16}{9}\frac{\mu^2\alpha_0}{L}\Delta_N \right] \right\}, \tag{2.32}$$

$$C_{33}^{sat} = \frac{L}{D}\left\{ d_2\theta + \frac{K_f}{\phi K_g L}\left[L_1\alpha' - \frac{4}{9}\frac{\mu^2\alpha_0}{L}\Delta_N \right] \right\}, \tag{2.33}$$

$$C_{13}^{sat} = \frac{L}{D}\left\{ d_2\theta + \frac{K_f}{\phi K_g L}\left[L_1\alpha' - \frac{4}{9}\frac{\mu^2\alpha_0}{L}\Delta_N \right] \right\}, \tag{2.34}$$

$$C_{44}^{sat} = \mu, \tag{2.35}$$

$$C_{55}^{sat} = \mu(1-\Delta_T), \tag{2.36}$$

where,

$$D = 1 + \frac{K_f}{K_g\phi}(\alpha_0 - \phi + \frac{K^2\Delta_N}{K_g L}), \quad \theta = 1 - \frac{K_f}{K_g}, \alpha' = \alpha_0 + \frac{K^2}{K_g L}\Delta_N,$$

$$K = \lambda + \frac{2\mu}{3}, L = \lambda + 2\mu, \alpha_0 = 1 - \frac{K}{K_g}, \; L_1 = K_g + \frac{4}{3}\mu,$$

$$\Delta_N = (4*e)/(3*g*(1-g)), \; \Delta_T = (16*e)/(3*(3-(2*g))),$$

$$d_1 = 1-\Delta_N, d_2 = 1 - \frac{\lambda^2}{L_2}\Delta_N, \; g = \mu/(\lambda + 2*\mu).$$

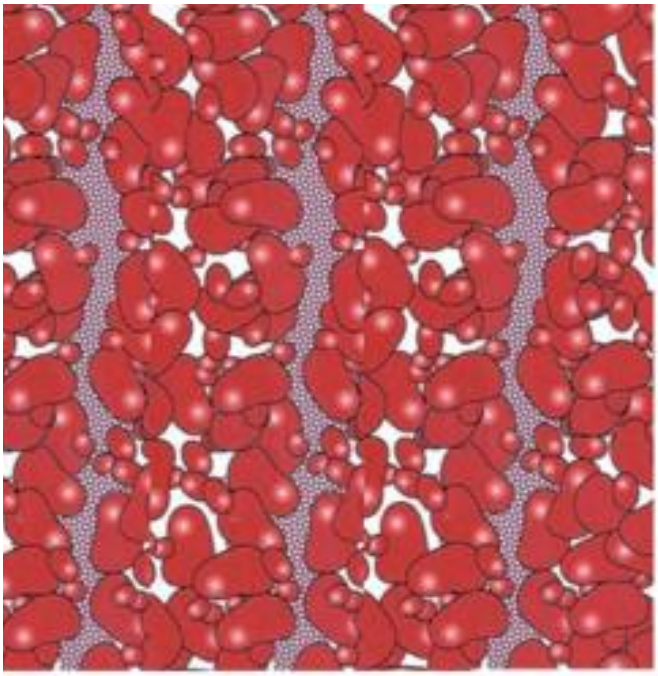

Figure 2.7: Schematic of porous fractured reservoir. The white color is the void space and the blue color represents vertical factures. Both void space and fractures are filled with a fluid (after Gurevich et al., 2009).

SUMMARY

In this chapter, I reviewed some important basic principles that are essential for carrying out the research work that I have reported in the following chapters. The first part discusses seismic anisotropy, its definition, importance, causes and symmetry classes. Transverse isotropy (TI) was discussed in more detail because analyses in this research are done on a TI model. The second part of this chapter gives a background on how the understanding of seismic partitioning of energy at an interface started and evolved over the years. The importance of amplitude variation with offset in quantifying medium parameters was highlighted. Both isotropic and anisotropic AVO equations were covered. The third part provides an overview of effective medium theory and how fractures can be represented in a rock physics formulation.

Chapter 3: Sensitivity Study of Fracture Parameters

INTRODUCTION

Model-based inversion involves building a forward model that is capable, to some extent, to reproduce real data and allows for robust estimation of model parameters from observation (Sen, 2006). The earth is naturally complex, and in an ideal case we need a large number of parameters to truly describe its heterogeneity. Alternatively, a more simplified earth model can be used, instead of a complicated one, that contains fewer parameters. This simplification process is called homogenization, and it is the basis of effective-medium theory. Effective-medium theory can be used to build a forward model that is robust enough to explain observation but also allows for meaningful parameter estimation. One use of effective-medium theory is to model a fractured reservoir, in anisotropic background material.

In this chapter, I use an effective-medium model to represent a fractured porous medium. The model was proposed originally by Gassmann (1951) with closed-form expressions for stiffness coefficients given by Gurevich (2003). A sensitivity analysis of Thomsen's Epsilon parameter is performed, to measure the difference between elastic properties of a wave traveling along and across fracture strike. Anisotropic reflection analysis is performed for a two-layer model, isotropic over HTI, to study the effect of variations in the model parameters on the amplitude variation with offset and azimuth (AVOA) response and consequently the intercept and gradient attributes. The motivation

for this study is to see which reservoir parameters have the greatest effect on the AVOA curves. This gives an idea about which parameter is reliable enough for inversion.

METHOD

Estimating fracture parameters from FMI logs

Formation micro-imaging (FMI) logs for four horizontal wells from a carbonate oil reservoir in the Arabian Peninsula are used. The rose diagram from all wells for open fractures is shown in Figure 3.1, which indicates a dominant fracture set oriented approximately East-West (N100ºW). This confirms our modeling assumption in dealing with one set of vertical fractures. Figure 3.2 shows a histogram of open fracture spacing from one of the horizontal wells derived from the FMI logs. The dominant fracture spacing is 20 cm. Making use of the fracture spacing parameter is a challenge because in order to calculate fracture density, fracture scale length is needed and FMI logs do not provide this information. We can conclude that we are dealing with one set of fractures, which validates the use of the Gurevich (2003) model, and that fracture density varies spatially across the reservoir.

ESTIMATING BACKGROUND PARAMETERS

Arithmetic averages of P-wave, S-wave velocities and density are taken from well logs. These measurements are then used to estimate the parameters of isotropic porous media. Values are shown the table below.

Vp	4600 m/s
Vs	2600 m/s
P	2400 kg/m^3

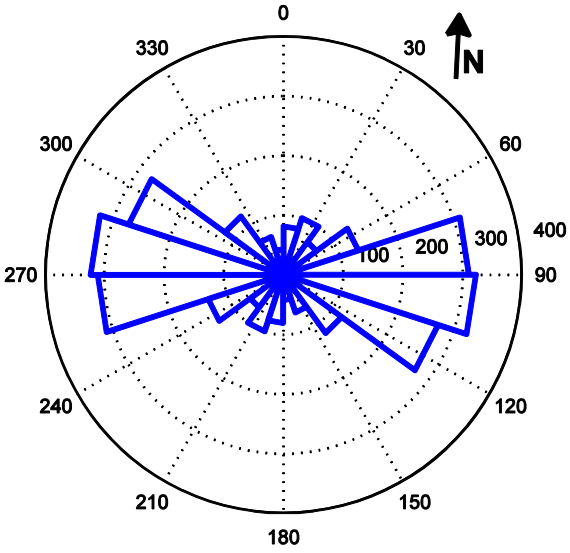

Figure 3.1: Rose diagram showing fractures dominant azimuthal direction for all wells. The outer circle numbers indicate azimuth and the inner circles indicate number of fractures.

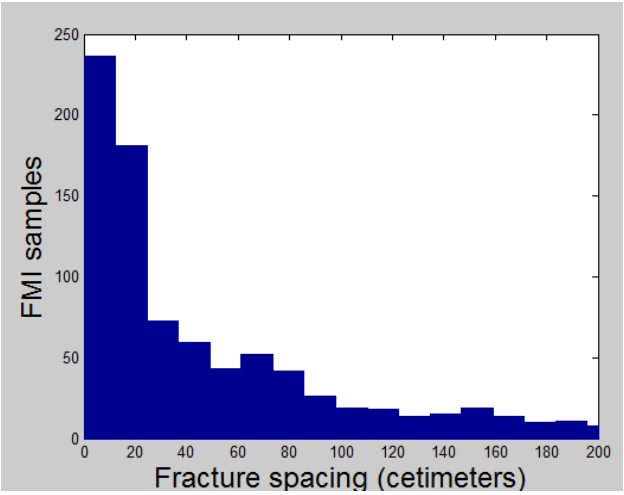

Figure 3.2: Histogram of fracture spacing for open fractures for one of the horizontal wells derived from FMI log. The dominant fracture spacing is 20 cm.

SENSITIVITY ANALYSIS

In order to understand how Thomsen's Epsilon parameter (ε) changes with regard to the porous fractured model, sensitivity analysis is done by changing three model parameters: fluid bulk modulus (K_f), porosity (Φ) and crack density(e). Sil et al (2010) reported a similar study where analysis is done on Shale/Sand interface. Here, the sensitivity study is done on as Anhydrite/Carbonate interface where ranges of acceptable parameter values are taken from well logs.

A 3-D cube is generated showing all possible combinations of the three model parameters, color coded by ε (Figure 3.3 a,b). In each cell of the cube, the three parameters are input into the Gurevich (2003) model, and the five elastic constants are calculated. Subsequently, the ε is calculated for this entry using:

$$\varepsilon = \frac{(C_{11} - C_{33})}{2C_{33}}. \tag{3.1}$$

Epsilon is an indicator of the degree of anisotropy caused by fracturing in our case especially when dealing with only one set fracture. Large ε values here indicate the predicted best possible combination of model parameters that shows a high degree of anisotropy. The 3D cube shows larger values of ε associated with high porosity, high crack density

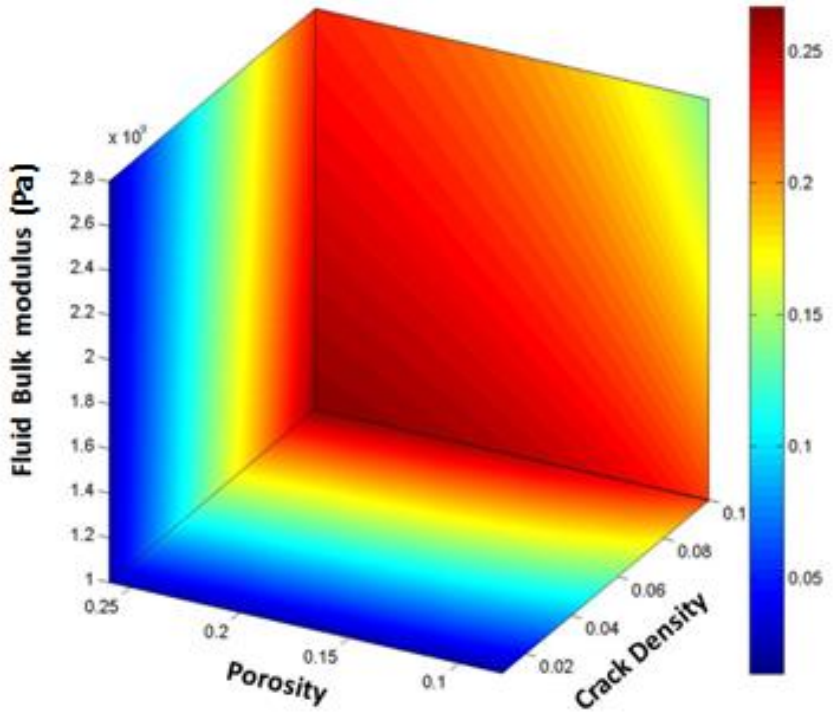

(a)

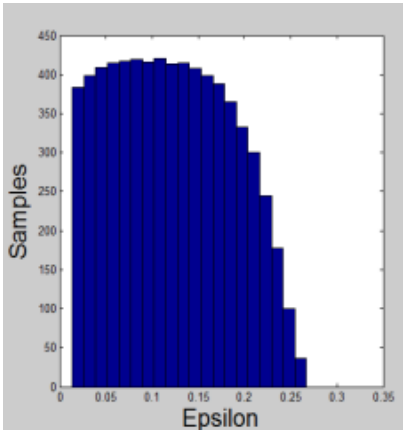

(b)

Figure 3.3: 3D cube (a) showing how the variation in the three model parameters would affect the Epsilon anisotropic parameter. The x-axis is porosity, y-axis is crack density, and z-axis is fluid bulk modulus. The histogram (b) shows all values of Epsilon present in the cube. Parameters values are (8-26%) for porosity, (1-2.8GP) for Kf and (0.01-0.1) for crack density.

and low fluid bulk modulus. To examine how each of the three parameters affects the change of ε , the gradient of ε is calculated:

$$\left(\frac{\partial \varepsilon}{\partial K_f}, \frac{\partial \varepsilon}{\partial \Phi}, \frac{\partial \varepsilon}{\partial e}\right). \tag{3.2}$$

The derivative terms indicate the sensitivity of ε to changes in fluid bulk modulus, porosity and crack density respectively. Three 3-D cubes are shown in (Figures 3.4a ,3.5a and 3.6a); however, they are color coded by the gradient of ε in the three directions. Analysis of Figure 3.4a, which describes the change of ε due to change in fluid bulk modulus, shows that the high values (red) are located at low porosity, high crack density, and high fluid bulk modulus. Figure 3.5a shows the change of ε due to the change in porosity where the largest change occurs at high porosity, high crack density, and low fluid bulk modulus. Figure 3.6a illustrates the change of ε due to the change in crack density where the largest change is associated with low porosity, high crack density, and low fluid bulk modulus. The histograms of each 3-D cube are shown in figures, 3.4b, 3.5b and 3.6b.

AZIMUTHAL AVO MODELING

The next step is to perform numerical simulation for the variation of amplitude with offset and azimuth (AVOA) to understand how the intercept and gradient attributes derived from the AVOA curves vary, given a change in porosity, crack density, fluid bulk modulus, and azimuth. An isotropic over an HTI interface is considered. Anhydrite is used as an isotropic cap rock that has P-wave velocity of 6050 m/s, S-wave velocity of 3200 m/s and density of 2900 kg/m^3. Equations (2.15) are used here to calculate the

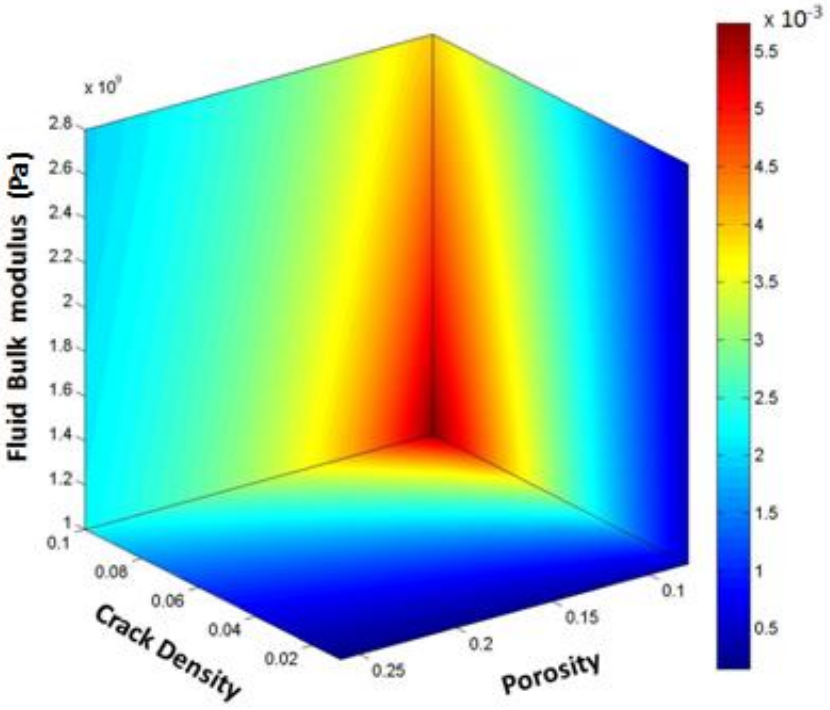

(a)

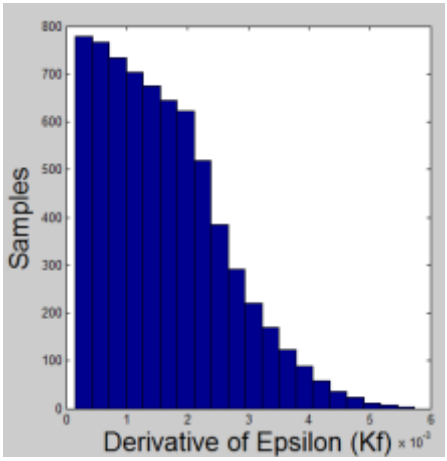

(b)

Figure 3.4: (a) 3D cube showing the gradient of the Epsilon due to changes in fluid bulk modulus. (b) Histogram of the gradient. The 3D cube is rotated to the left from figure 3.3 to highlight the area of the highest change in values.

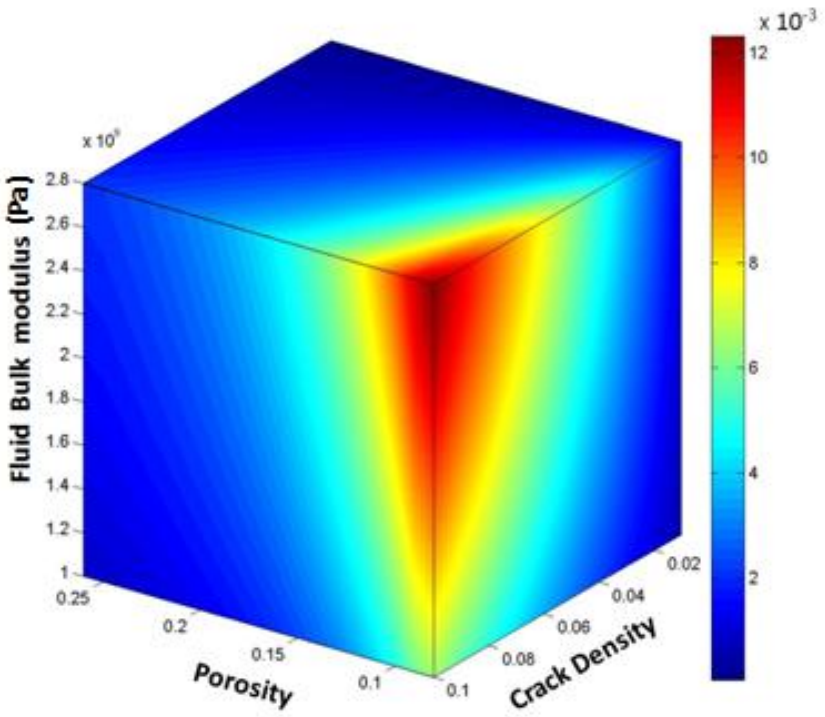

(a)

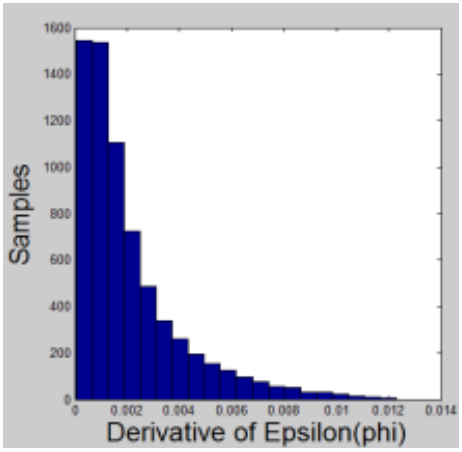

(b)

Figure 3.5: (a) 3D cube showing the gradient of the Epsilon due to changes in porosity. (b) Histogram of the gradient. The 3D cube is rotated left down from figure 3.3 to highlight the area of the highest change in values.

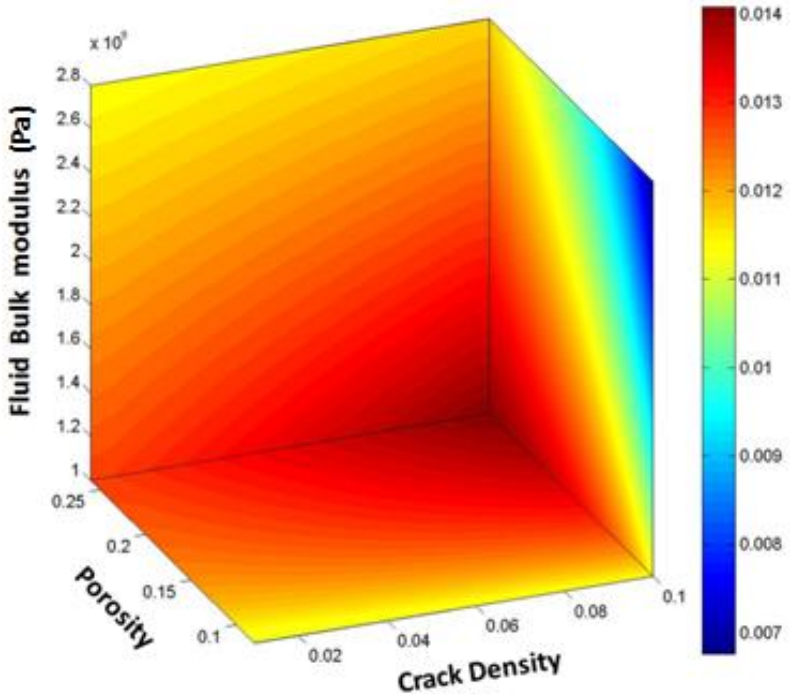

(a)

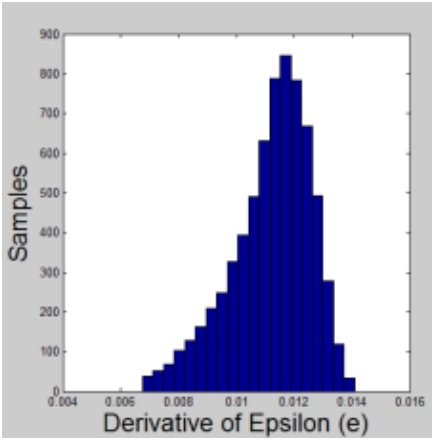

(b)

Figure 3.6: (a) 3D cube showing the gradient of the Epsilon due to changes in crack density. (b) Histogram of the gradient. The 3D cube is rotated slightly down right from figure 3.3 to highlight the area of the highest change in values.

intercept (A) and gradient terms (B). The intercept term corresponds to normal incident waves and the gradient term correspond to intermediate angles of incidents up to 30 degrees. In this analysis the largest incident angle is 30 degrees, and the third term (C) is neglected here because of its high-order effect at intermediate angels.

Intercept and gradient terms are calculated for all possible combination of model parameters. Each entry in the 3D cube from Figure 3.3 is populated with intercept and gradient attributes. Two calculations are done, one for a seismic wave traveling along the fractures and another for one traveling across the fracture. Incident angles used are up to 30 degrees. Figure 3.7 shows the cross plot of intercept and gradient terms color coded by crack density. Data points for the seismic wave traveling across the fractures show how the crack density parameter is well separated and robust estimation is possible. When the same cross plot is color coded by porosity (Figure 3.8), it can be seen that at low crack density values (blue area in Figure 3.7), the porosity does not show a clear separation and as the crack density increases, the estimation of porosity values is more robust. In other words the points of different colors (porosity values) are not clustered in a narrow a band; they are separated at high crack density values (blue area in Figure 3.7), which maximize the change of estimating them from the intercept-gradient cross plots. Figure 3.9 shows the same cross plot, but the color code is the fluid bulk modulus. The estimation of fluid bulk modulus shows a similar behavior to porosity in Figure 3.8 but it is less robust than porosity because many points are clustered in a narrower band than the porosity points for all combinations of parameters.

Another modeling step is performed to see how changing model parameters

would affect the azimuthal reflection response from an Isotropic/HTI interface. Fluid bulk modulus is set constant at 1 GPA to represent an oil-bearing, fractured reservoir. Porosity and crack density values are drawn from a normal distribution. The P-P reflection response is computed using Rüger's equations for four azimuths ranging from a wave traveling along the fractures to a wave traveling across the fractures. Figure 3.10a shows that for the cross plot of intercept and gradient, crack density is difficult to estimate for a wave traveling along the fractures. This is understandable because P-waves do not sense fractures when they travel along them. The histogram is shown in Figure 3.10b. Furthermore, as the seismic wave propagation direction approaches the direction across the fractures, estimation of crack density becomes more robust. Figure 3.11 shows a similar observation for the porosity parameter and the histogram is shown in Figure 3.11b.

CONCLUSIONS

FMI analysis in four boreholes indicated one set of dominant fractures. The change in Epsilon due to porosity is the highest at high crack density, high fluid bulk modulus and low porosity. Change in Epsilon due to crack density is the highest at low fluid bulk modulus and high porosity and high crack density. Epsilon change due to fluid bulk modulus is greatest at low porosity, high crack density and low fluid bulk. Crack density is the easiest parameter to discriminate in the intercept-gradient plot. Porosity estimation is more robust at high crack density and fluid bulk modulus is the hardest parameter to discriminate. Crack density and porosity is best estimated when seismic waves travel across the fractures. It is understood that besides using an idealized earth model all other effects that might hinder the robustness of parameter estimation like noise to signal ratio and overburden effects are ignored.

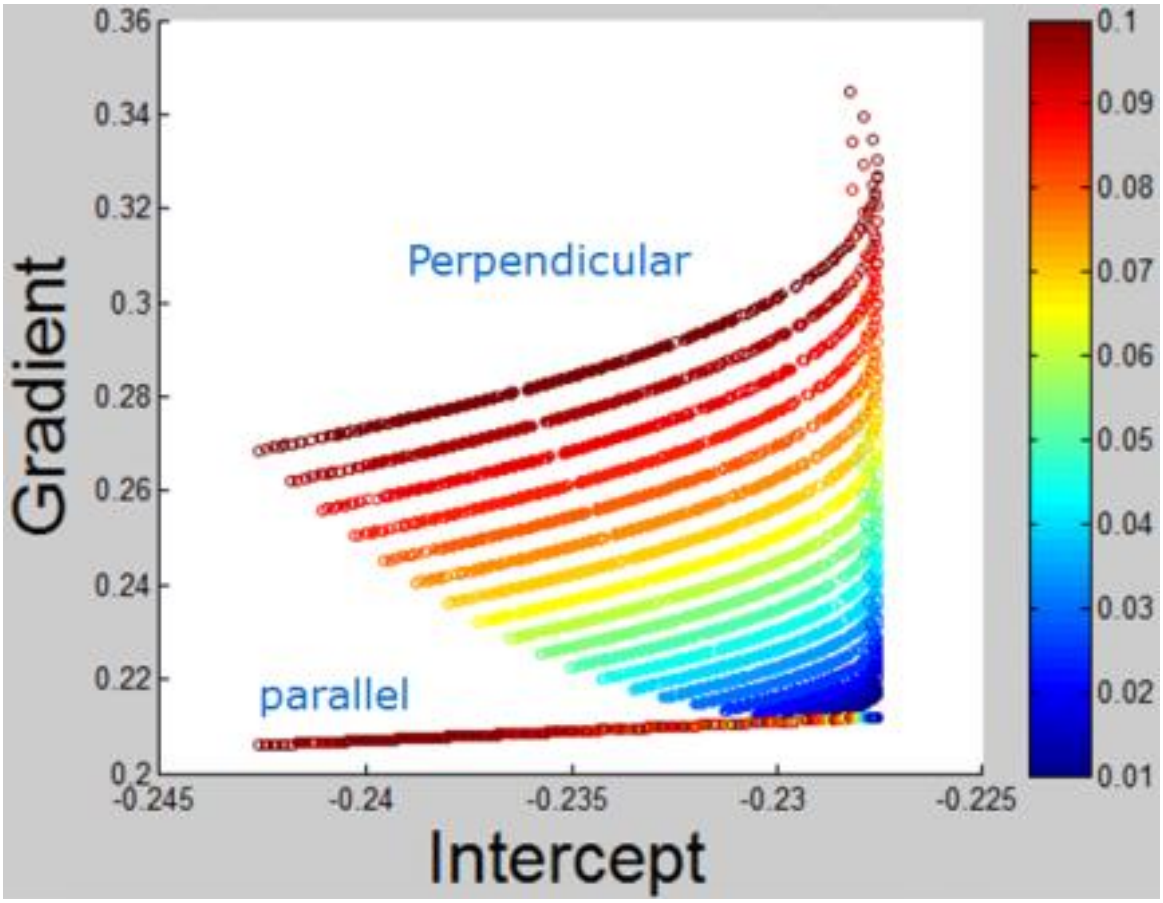

Figure 3.7: A cross plot of intercept and gradient terms color coded by crack density

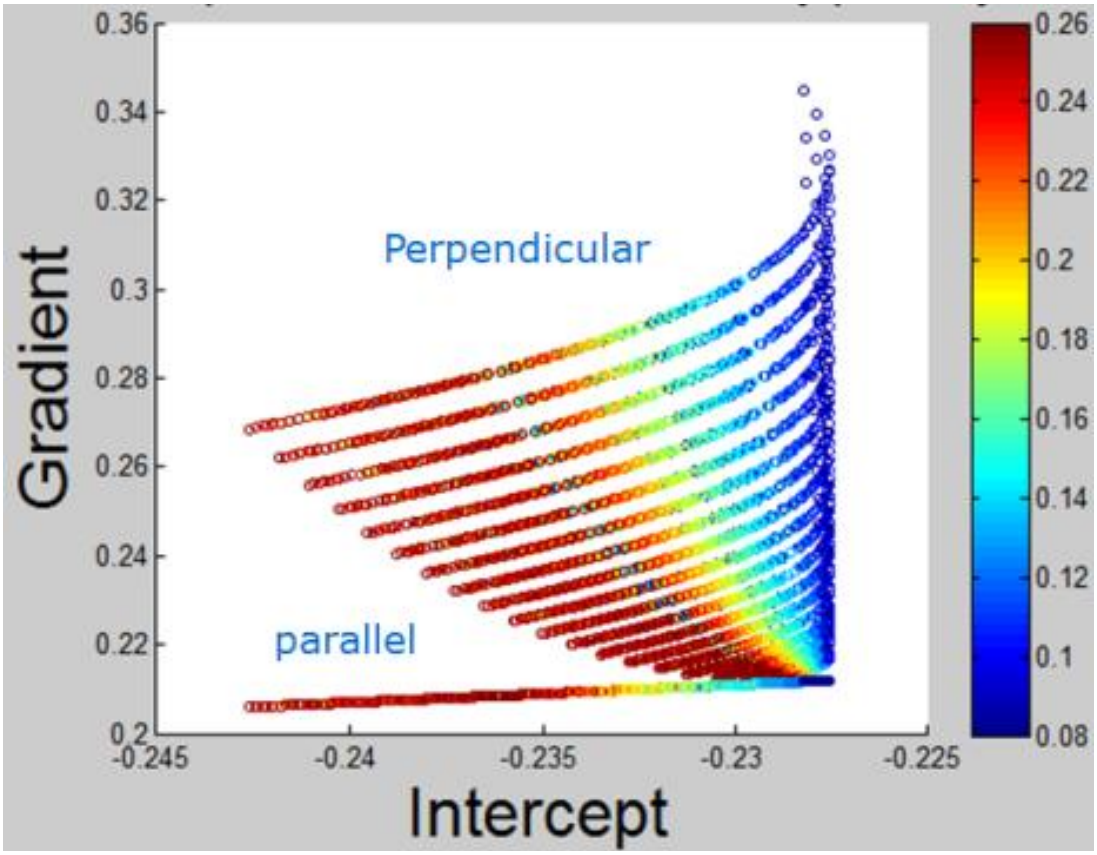

Figure 3.8: A cross plot of intercept and gradient terms color coded by porosity.

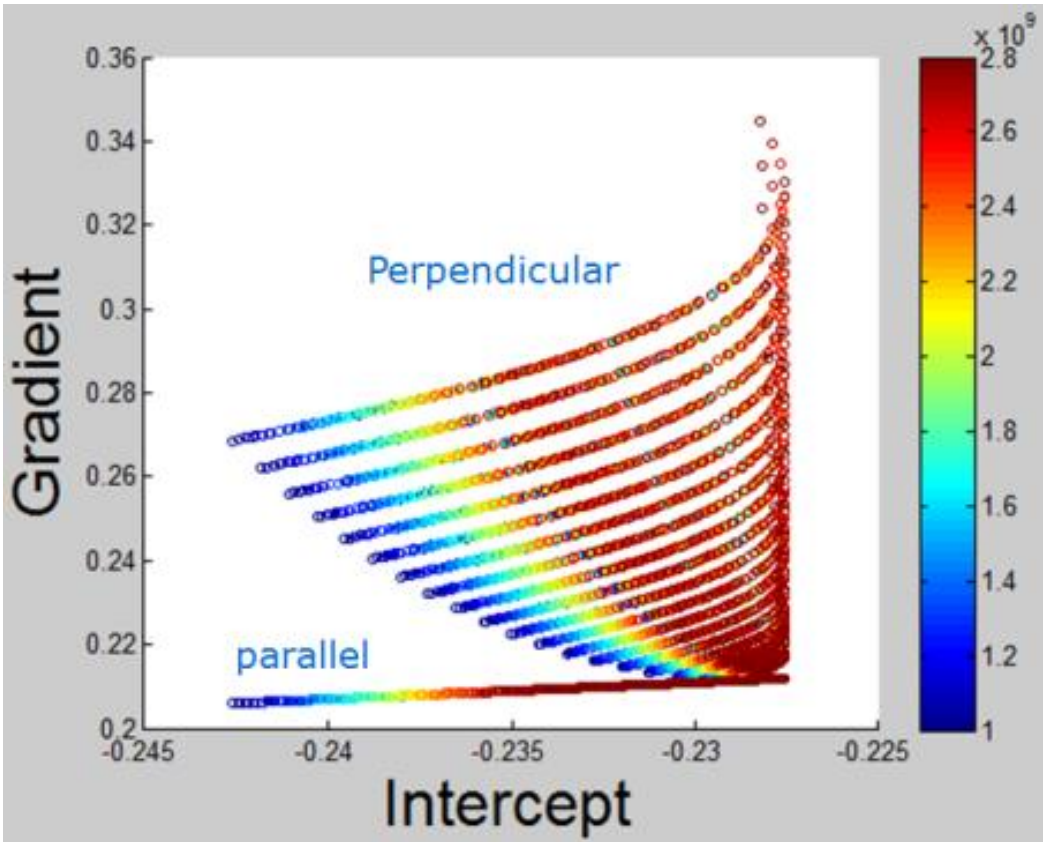

Figure 3.9: A cross plot of intercept and gradient terms color coded by fluid bulk modulus.

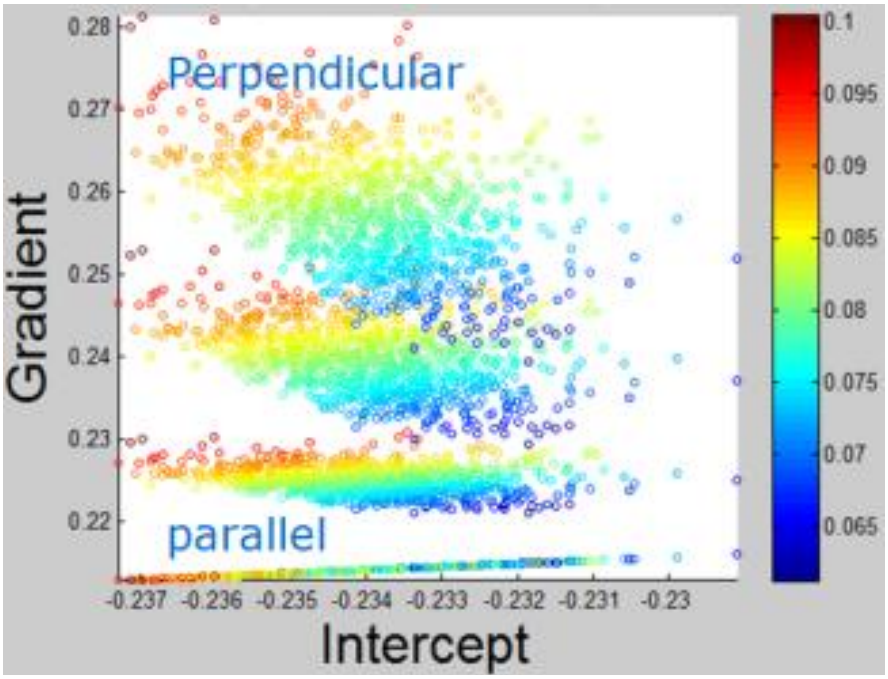

(a)

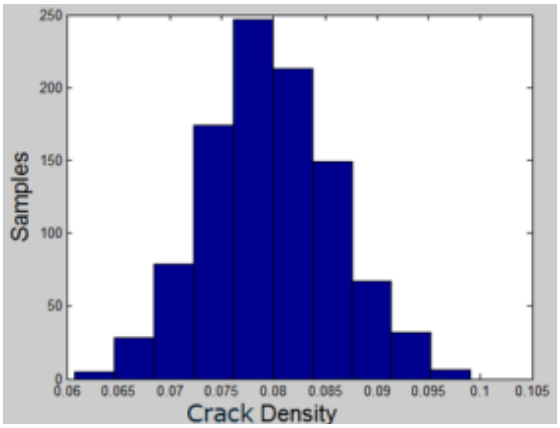

(b)

Figure 3.10: Cross plot of intercept and gradient attribute for the azimuthal AVO response of Isotropic/HTI interface along with histograms of random values used, color coded by crack density (a) .(b) Histogram of crack density values.

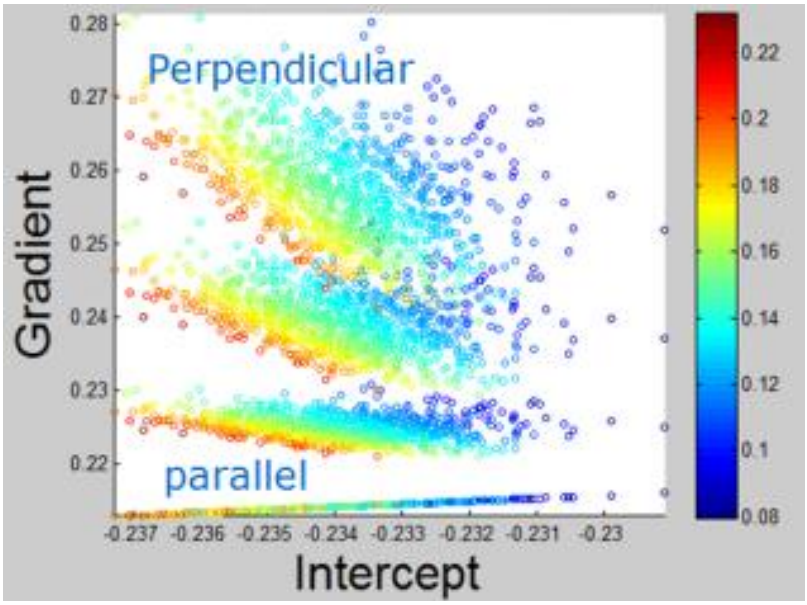

(a)

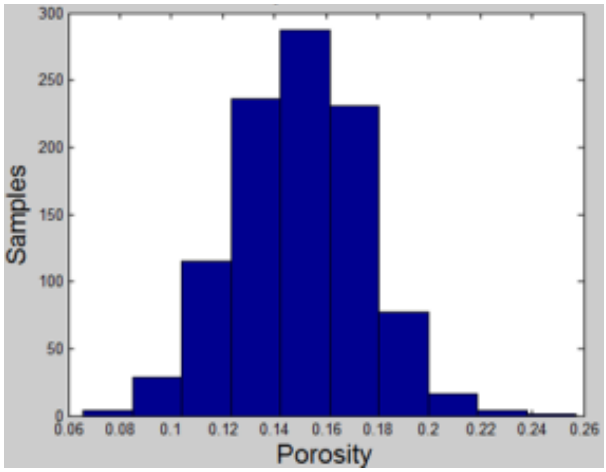

(b)

Figure 3.11: Cross plot of intercept and gradient attribute for the azimuthal AVO response of Isotropic/HTI interface along with histograms of random values used, color coded by porosity (a) . (b) Histogam of porosity values.

Chapter 4: Removing Anisotropic Overburden Effect for Reliable Reservoir Fracture Characterization

INTRODUCTION

Cumulative effects of seismic waves propagating in the overburden can distort the amplitudes of seismic reflections from a target reservoir. Hence, erroneous amplitude analysis of the reservoir may result if overburden effects are ignored. Many factors can cause distortion in amplitudes including, shallow sediments such as sand dunes, regional and local structural variations, sinkholes, shallow channels, and anisotropy in shallow layers. The need to account for such effects has been recognized by Luo et al. (2005, 2007), Liu et al. (2011), and others. Transmission effects caused by the presence of anisotropic layers in the overburden, for example, can easily hinder the AVOA analysis, which can lead to unreliable estimates of anisotropic reservoir parameters (Sen et al., 2007).

For a single set of vertical fractures, the medium can be considered a transversely isotropic medium with a horizontal axis of symmetry or an HTI medium in the low frequency limit (Schoenberg and Douma, 1988, Tsvankin, 2005). Conventional AVOA analysis is generally applied to the top of the reservoir where vertical fractures within the reservoir cause variation of reflected amplitude with source-receiver offset and azimuth. The AVOA signature from the base of the fractured unit, however, is generally stronger than that from the top. Azimuthal variations from the top of the reservoir depend only on the variation in reflection coefficient, whereas the raypath is also a function of azimuth for reflections from the base of the fractured unit, leading to stronger, more visible variation of AVO with azimuth (Sayers and Rickett, 1997). This also leads to the conclusion that an azimuthal variation in AVO due to fractures in the overburden may be

misinterpreted because of the presence of aligned fractures within the reservoir (Sayers and Rickett, 1997).

Two fundamental problems arise when analyzing AVOA of the base of reservoir reflection. The first one is that many petroleum reservoirs are not thick enough to clearly separate top and bottom reflectors given the frequency range of seismic data. Thin bed interference effects (e.g, internal multiples, tuning) would make it difficult to effectively invert for reservoir parameters (Sen et al., 2007). The second problem is that the base of reservoir reflection may not be detected in surface seismic data due to the gradual change from reservoir properties to the layer below reservoir. Analysis of the data acquired in my study area indicated that second problem is indeed present.

In this chapter, I propose a new technique to remove the effect of transmission through the overburden by analysis of picked amplitudes from the reservoir top and from an isolated reflector below the reservoir. I show that the technique results in more accurate estimation of reservoir fracture parameters.

PARAMETER ESTIMATION AND FORWARD MODELING

Estimation of fracture parameters (e.g., number of dominant fracture sets, fracture density and orientation) used as an input to a forward model is based on borehole logs including FMI logs. Despite the fact that FMI logs are not representative of the entire reservoir and are not as commonly acquired as conventional well logs, the FMI Log data are considered to be a direct measurement of fracture parameters and should be weighed heavily in estimating the parameters of our fracture model. A rose diagram for all open fractures from all horizontal wells shows that here we have only one set of vertical

fractures oriented approximately WNW-ESE (Figure 3.1). The information taken from conventional well logs and FMI logs indicate that the reservoir is porous and fractured; therefore, I conclude that forward models of a porous, fractured rock would best describe the reservoir. Five independent effective medium parameters are derived for a saturated porous fractured reservoir using the Gurevich (2003) model. This model is used here because it uses a limited number of parameters to describe porous fractured rocks and is a reasonably good representation of my field.

Well log interpretation shows that the reservoir has a coarsening upward sequence where the quality of the reservoir is gradually improving upward. This is clearly indicated by lower Vp and Vs velocities, and lower density values at the top of the reservoir. In order to depict reservoir parameters closely, the reservoir is divided into 14 layers each with different Vp, Vs, density and prorosity values. Figure 4.1 shows how these four parameters gradually vary across different depths of the reservoir in a simillar manner to the logs. Vertical crack density and orientations are set to be constant in all layers.

In order to investigate the effect of an anisotropic overburden on AVOA analysis, two models are considered. The first one consists of an anhydrite cap rock and vertically fractured carbonate reservoir (14 layers as mentioned above) and an isotropic overburden. The second model is the same but with added anisotropic section in the overburden that includes a layer with vertical fractures. Both models can be seen in Figures 4.2 and 4.3. Fracture sets in the overburden and in the reservoir are taken to be 90 degrees azimuth relative to each other. Full-waveform numerical simulation (Mallick and Frazer 1991) is performed on both models for several source-receiver offsets and azimuths. Offset values are from zero to 3200 m in increments of 80 m. The dominant frequency of the wavelet used is 35 Hz, and the target horizon is at a depth of 1500 m. The resultant gathers, the zero azimuth direction for each model, are shown in Figures 4.4 and 4.5.

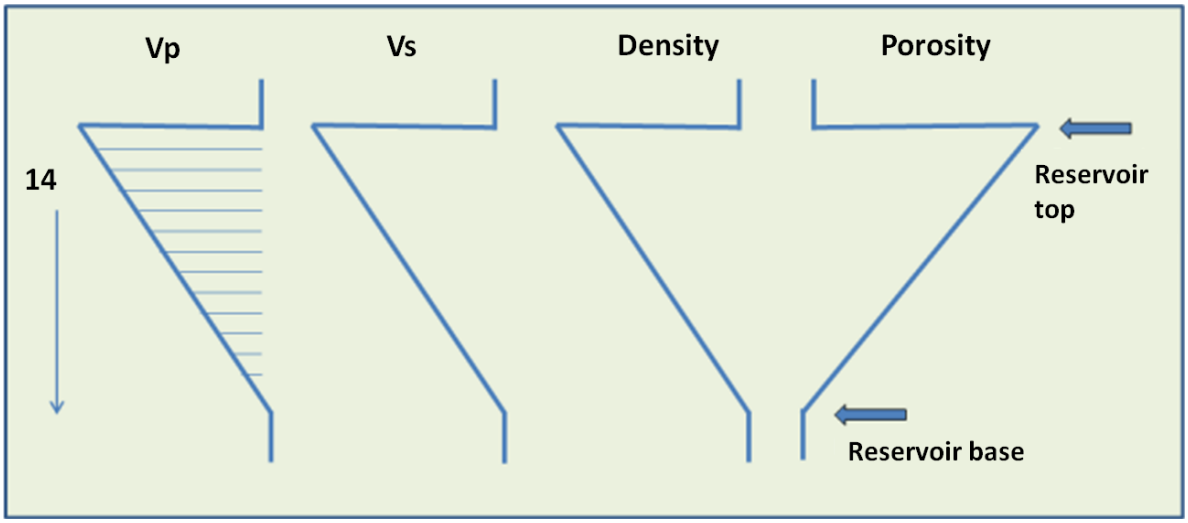

Figure 4.1: Reservoir interval is divided into 14 different horizontal layers. Each layer has a different set of reservoir property values.

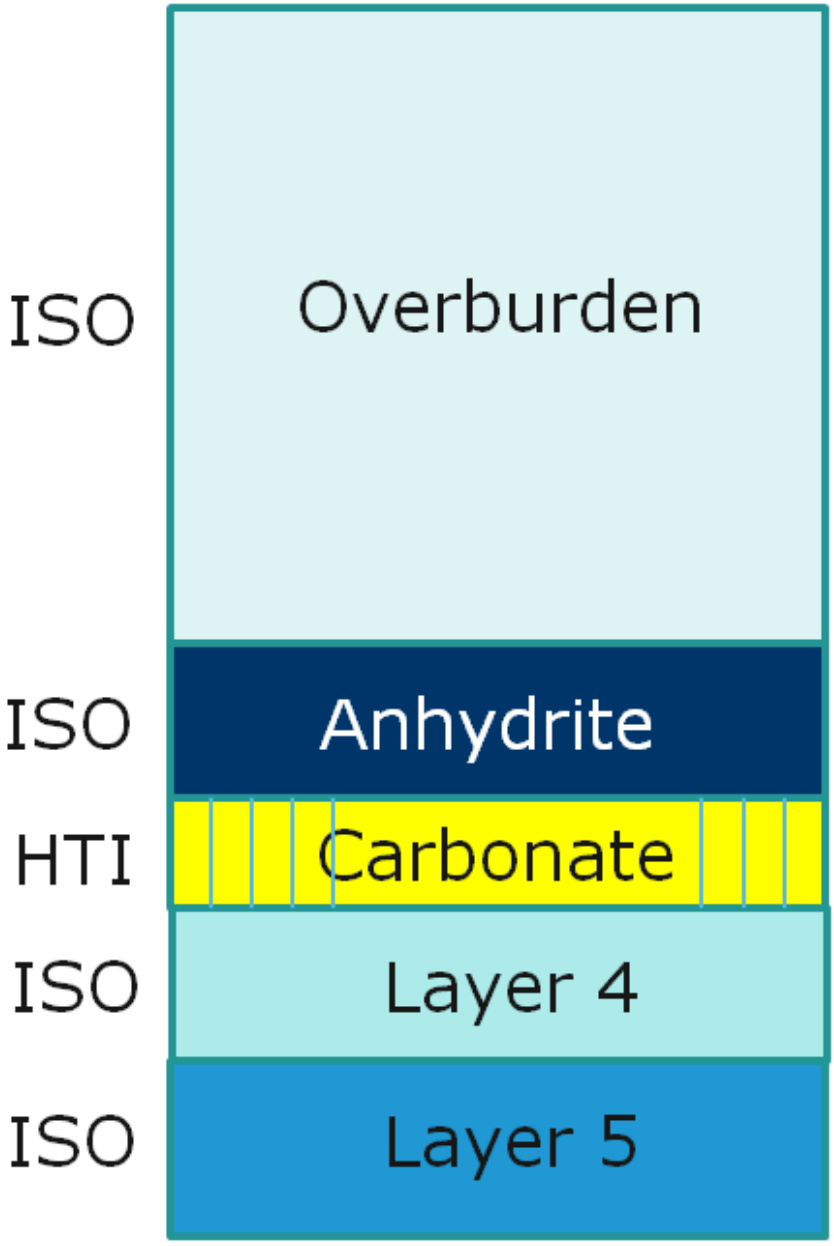

Figure 4.2: Forward model including anhydrite cap rock and vertically fractured carbonate reservoir and isotropic overburden.

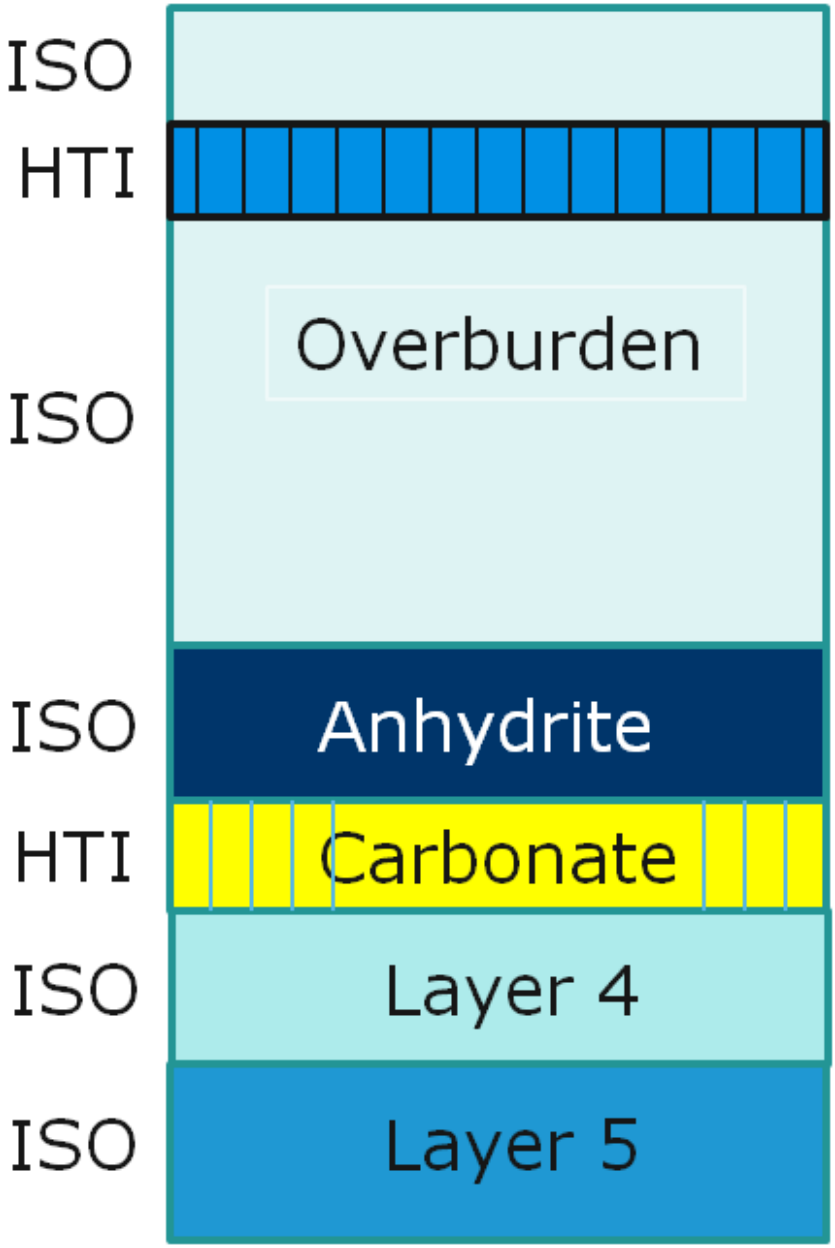

Figure 4.3: Forward model including anhydrite cap rock and vertically fractured carbonate reservoir and anisotropic overburden.

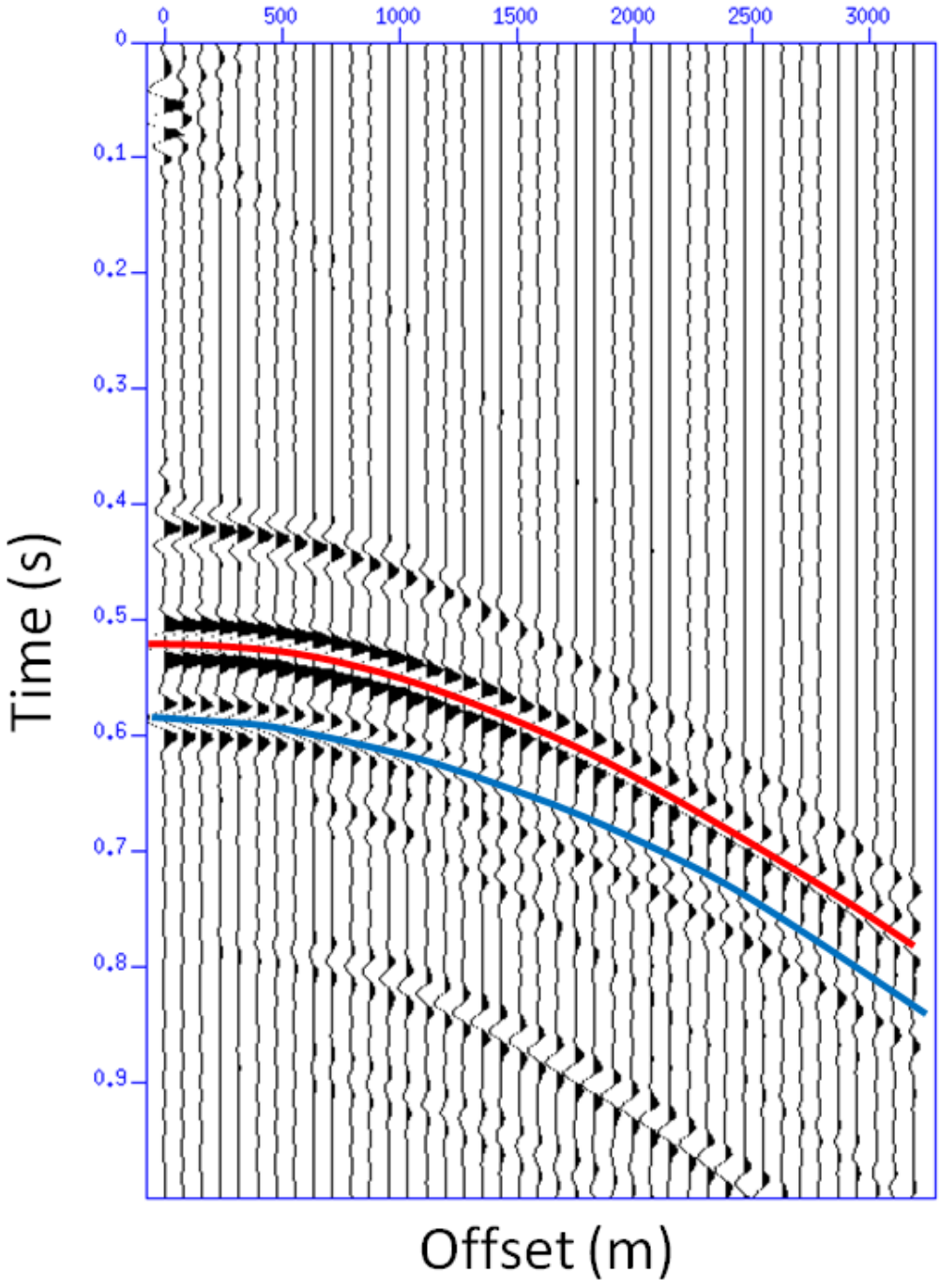

Figure 4.4: Full-waveform synthetic CMP gathers for a model with isotropic overburden. Red and blue picks denote reservoir top and a reflector below the reservoir, respectively. The azimuth direction is zero, which corresponds to a seismic wave traveling across the fractures.

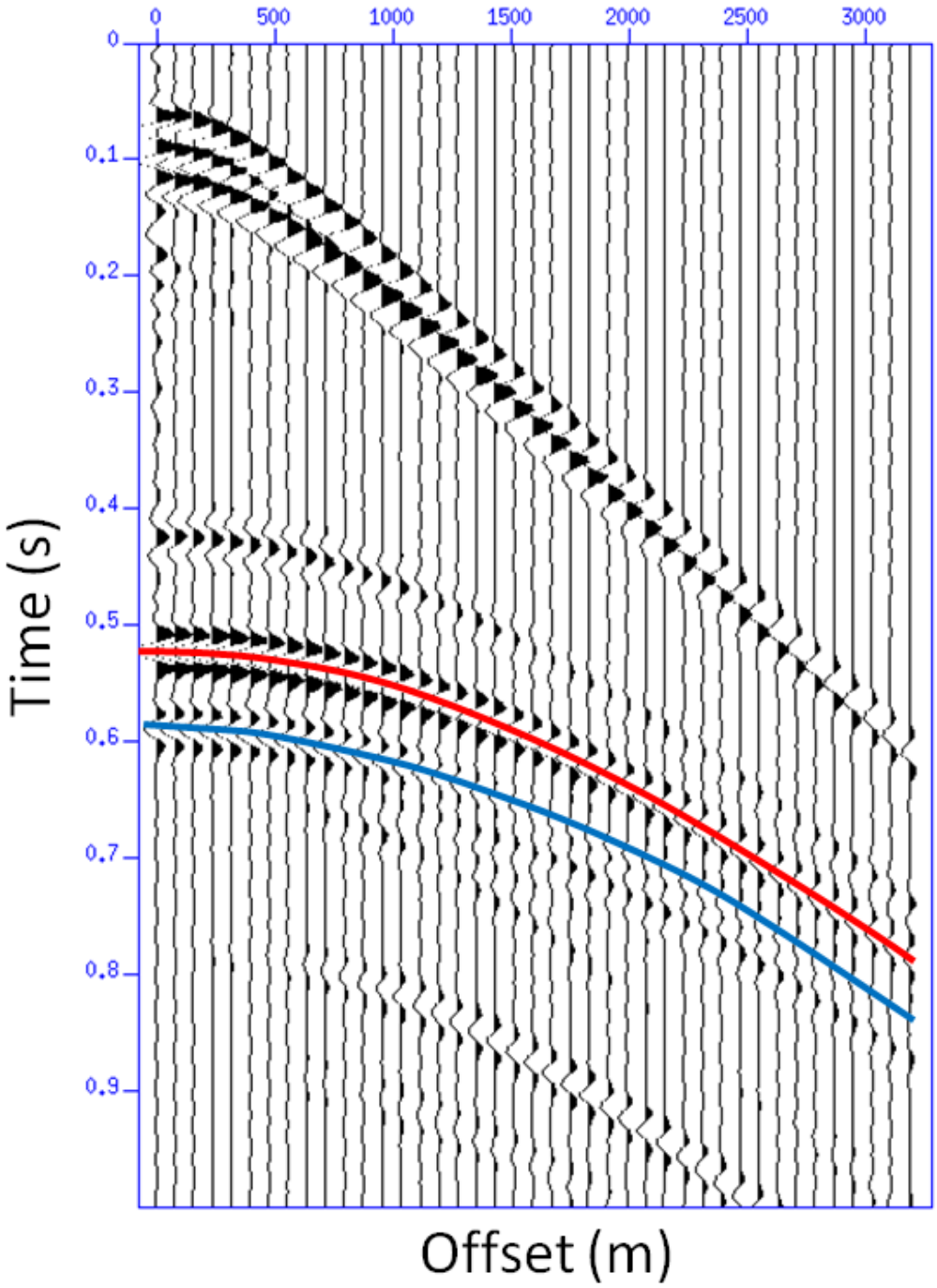

Figure 4.5: Full-waveform synthetic CMP gathers for a model with anisotropic overburden. Red and blue picks denote reservoir top and a reflector below reservoir respectively. The azimuth direction is zero which corresponds to a seismic wave traveling across the fractures.

CONVENTIONAL AVOA ANALYSIS

Reflection amplitudes for both the reservoir top (Anhydrite/Reservoir interface) and for a reflector below the reservoir (Layer 4/Layer 5 in Figure 4.2) are picked for all source-receiver azimuths. The base of the reservoir reflection (Reservoir/Layer 4) is not evident in the synthetic gathers because of the smooth transition in rock properties between the two layers. Figure 4.6 shows the AVOA curves for reservoir top (a) and for a reflector below the reservoir (b) at different azimuths for the model with isotropic overburden. The 0 and 90 degree azimuths correspond to a seismic wave traveling across and along fractures, respectively. Earth is complicated in nature and the assumption of isotropic overburden is not usually valid. Figure 4.7 shows the AVOA response of both reservoir top (a) and for a reflector below the reservoir (b), which represents the model in Figure 4.3. Here the overburden has one anisotropic layer caused by one set of vertical fractures which is perpendicular to the reservoir fracture set. Zero degree azimuth corresponds to a seismic wave traveling across fractures in the reservoir section and along fractures in the anisotropic layer in the overburden (Fracture sets in both sections are 90 degree azimuth to each other). Figure 4.7 shows that the AVOA response has been greatly affected by the existence of the anisotropic overburden, which could cause erroneous estimation of reservoir fracture parameters.

Proposed method

Seismic gathers for two models - one with isotropic overburden (Figure 4.4) and the other with anisotropic overburden (Figure 4.5) are transformed to the delay-time slowness (tau-p) domain. One seismic gather that corresponds to a zero azimuth (seismic wave that travels across the fractures) is shown in Figure 4.8 a, b. The red and

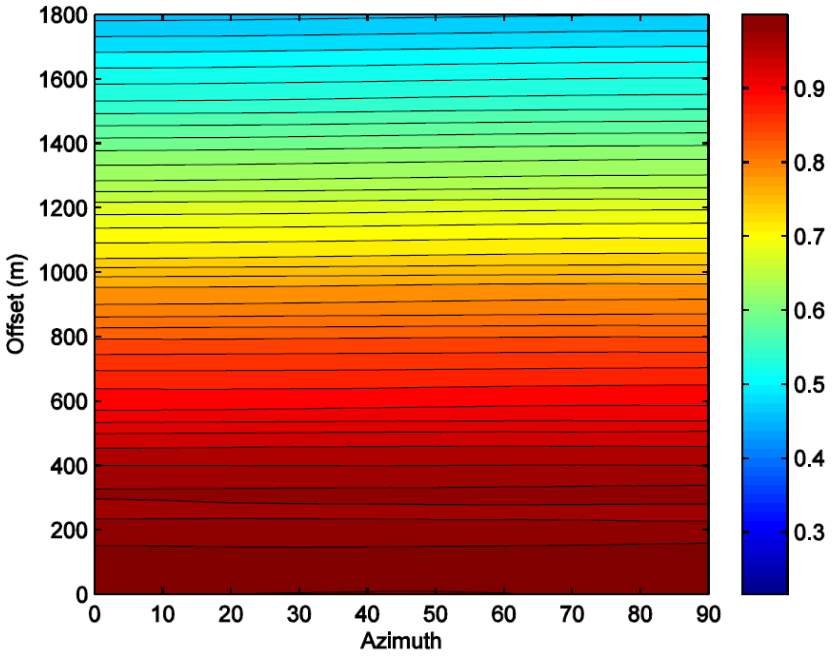

(a)

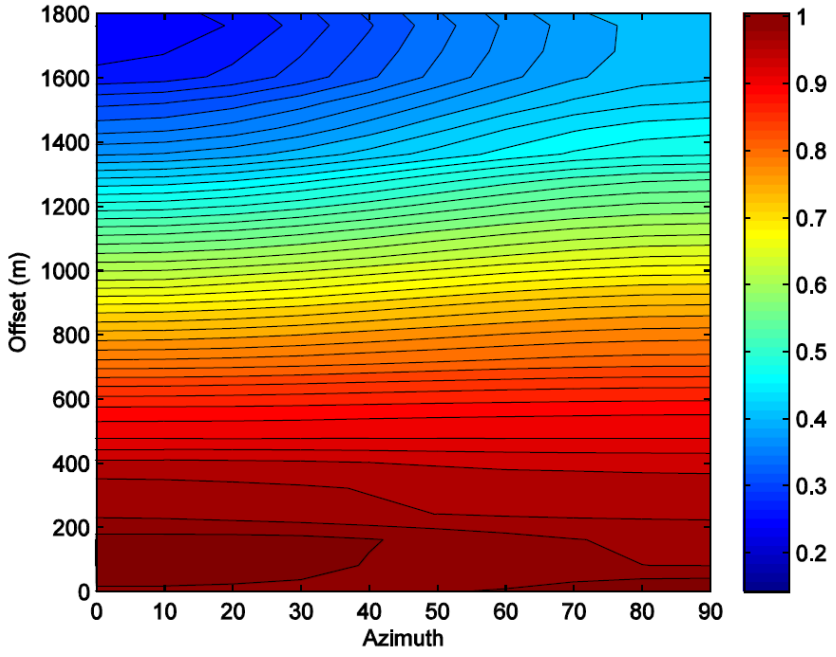

(b)

Figure 4.6: AVOA response of reservoir top (a) and for a reflector below the reservoir (b) for a model which has isotropic overburden.

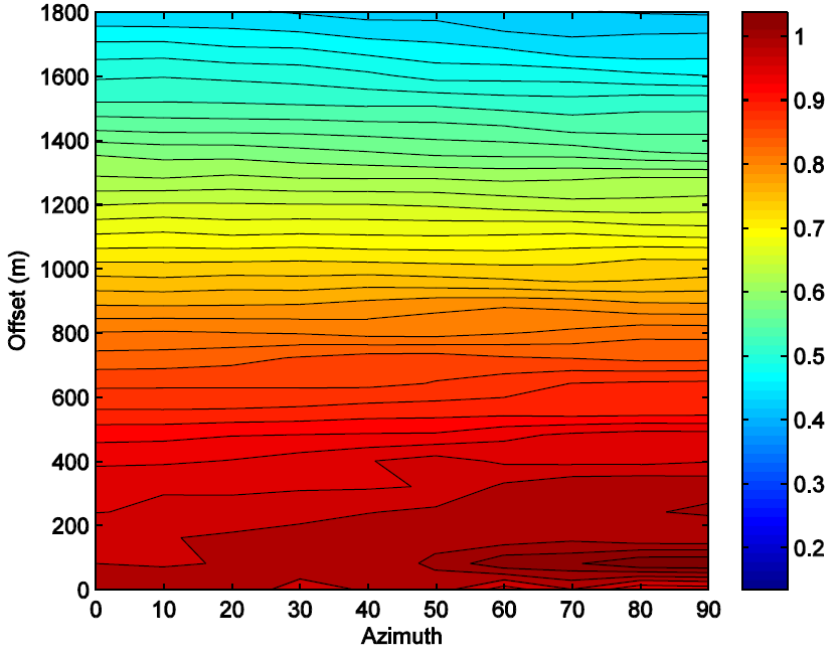

(a)

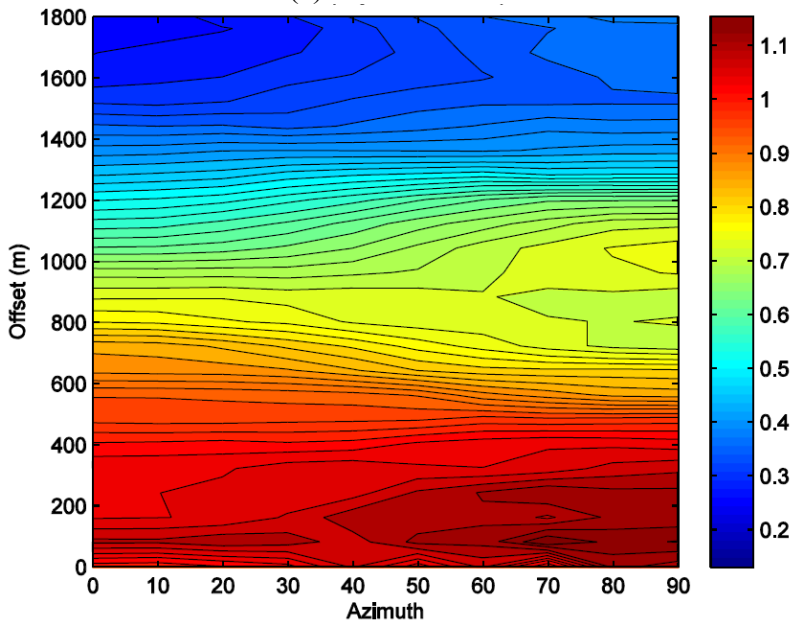

(b)

Figure 4.7: AVOA response of reservoir top (a) and for a reflector below the reservoir (b) for a model which has an anisotropic overburden.

blue lines correspond to reservoir top and a reflector below reservoir respectively. The ratio of amplitudes from both reflectors is taken in order to remove the transmission effect from the overburden. The ratio equation is:

$$R_{ratio} = \frac{T_{1\to2}^{down}T_{2\to3}^{down}R_3T_{3\to2}^{up}T_{2\to1}^{up}}{T_{1\to2}^{down}R_2T_{2\to1}^{up}} = T_{2\to3}^{down}(\frac{R_3}{R_2})T_{3\to2}^{up}\ , \qquad (4.1)$$

where: $T_{1\to2}^{down}, T_{2\to1,}^{up} T_{2\to3}^{down}, T_{3\to2}^{up}$ are upward and downward transmission amplitudes between layers 1, 2 and 3. $R_3\ and\ R_2$ are reflection amplitudes for layer interface. Figure 4.9 shows the model used for equation 4.1.

The ratio results for the two models can be seen in Figure 4.10 a, b. The overburden effect that hindered AVOA analysis is greatly reduced and both the ratio attributes from both models are almost identical. Fracture parameters can now correctly be estimated. If the ratio of the two horizons is taken in the t-x CMP domain, overburden effect is not removed as shown in figure 4.11 a, b. This indicates that the tau-p is the correct domain to take the ratio attribute in, where each trace in figure 4.8 has one ray parameter value.

Conclusions

A method to remove the effect of an anisotropic overburden in order to recover true reservoir fracture parameters is presented. It involves analyzing AVOA for a top reservoir pick and for a reflector below the reservoir. Seismic gathers are transformed to delay-time slowness (tau-px,py or tau-p,azimuth) domain and the ratio of the top reservoir pick to the layer below the reservoir is taken in order to remove transmission

effect from the overburden. Note that it is the ray-parameter and not the angle that remains constant in different layers and that the reflection/transmission coefficients are fundamentally functions of ray-parameters. That is precisely the reason as to why the ratio method works better in tau-p than in x-t domain. The method is applied to two sets of forward models one containing fractured reservoir with isotropic overburden and the other is the same model but with anisotropic overburden. Conventional analysis in the t-x domain shows that the anisotropic overburden has completely obscured the anisotropic estimation. When the new method was applied, the overburden effect was removed and more reliable anisotropic fracture parameter estimation can be reached.

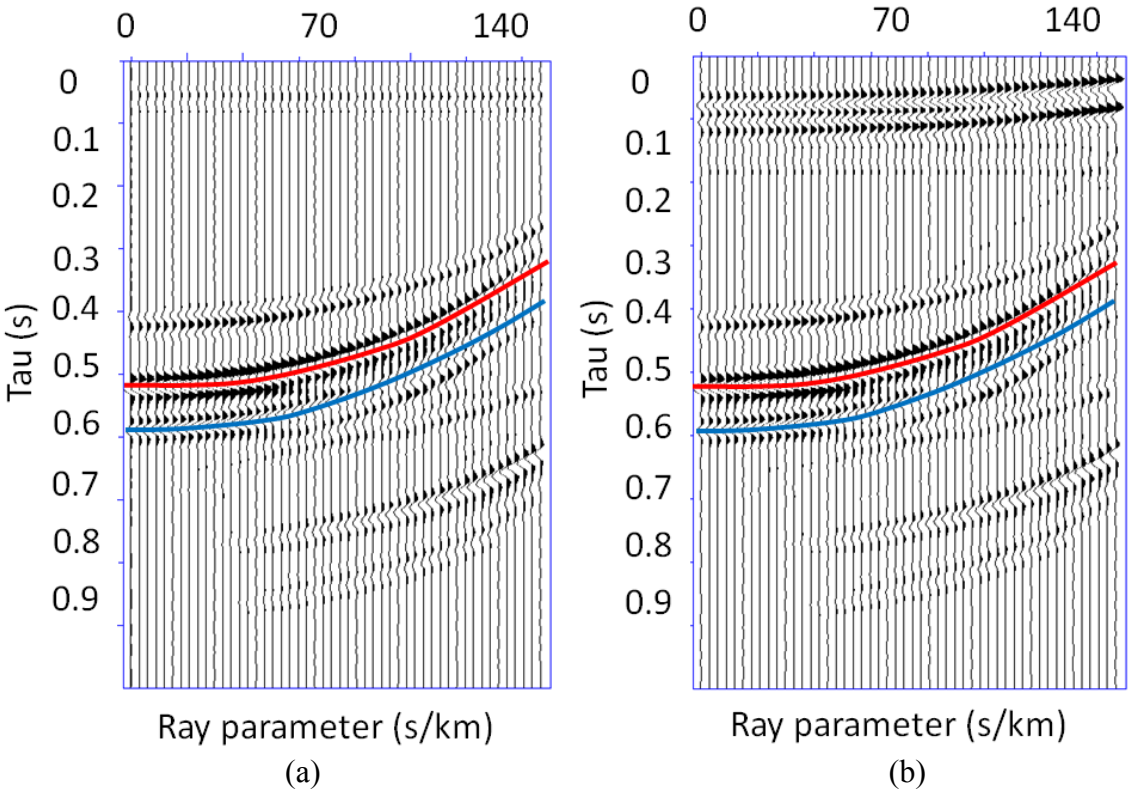

Figure 4.8: Transformed CMP gathers in the tau-p domain for both the model with isotropic overburden (a) and anisotropic overburden (b). The red and blue lines correspond to reservoir top and a reflector below reservoir , respectively. The azimuth direction is zero which corresponds to a seismic wave traveling across the fractures in the reservoir.

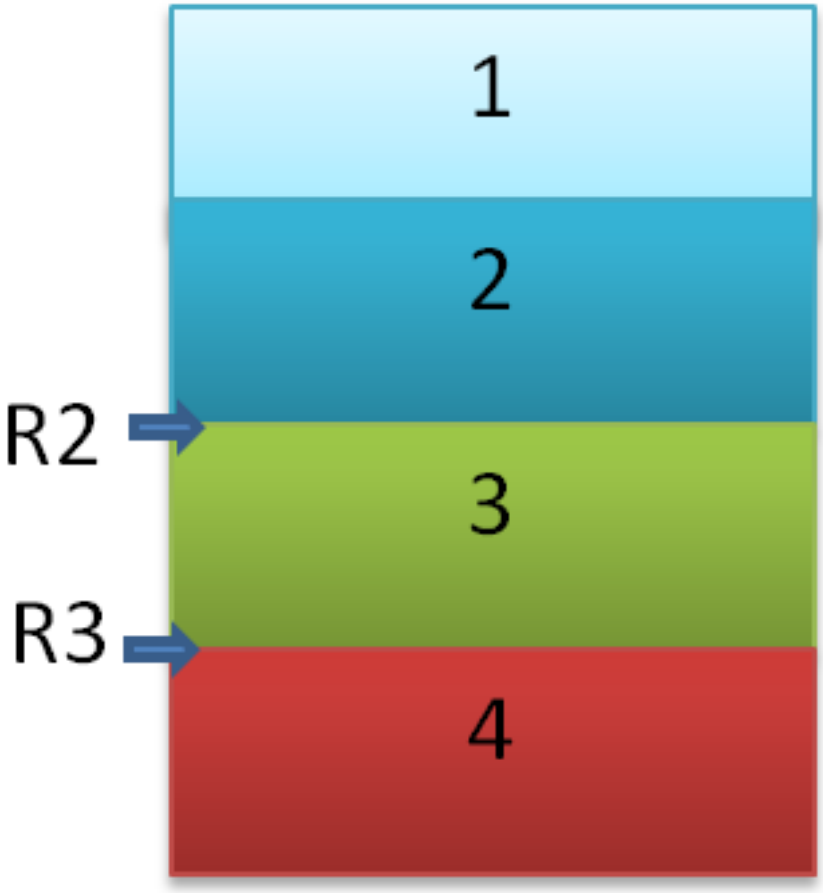

Figure 4.9: A four-layer model where R2 and R3 are defined in equation 1.

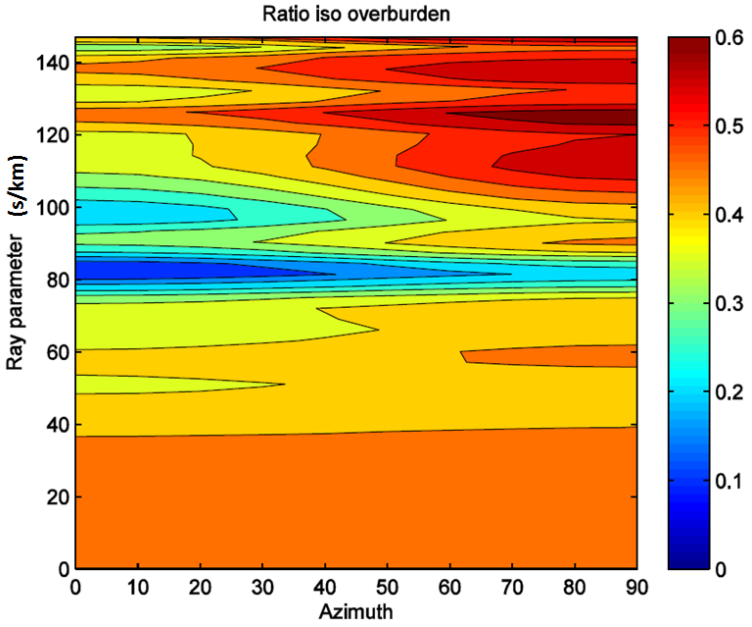

(a)

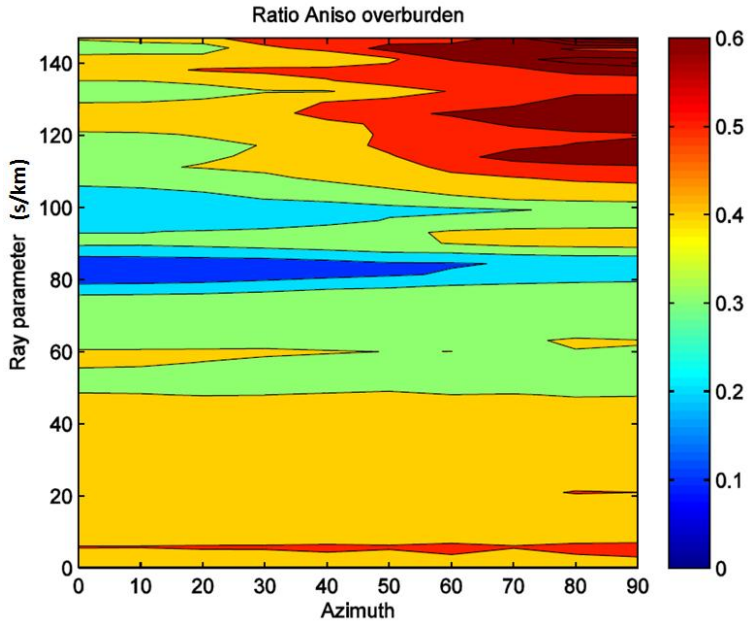

(b)

Figure 4.10: Ratio for reservoir top and a reflector below reservoir picks in the tau-p domain for two models one with isotropic overburden (a) and the other with anisotropic overburden (b).

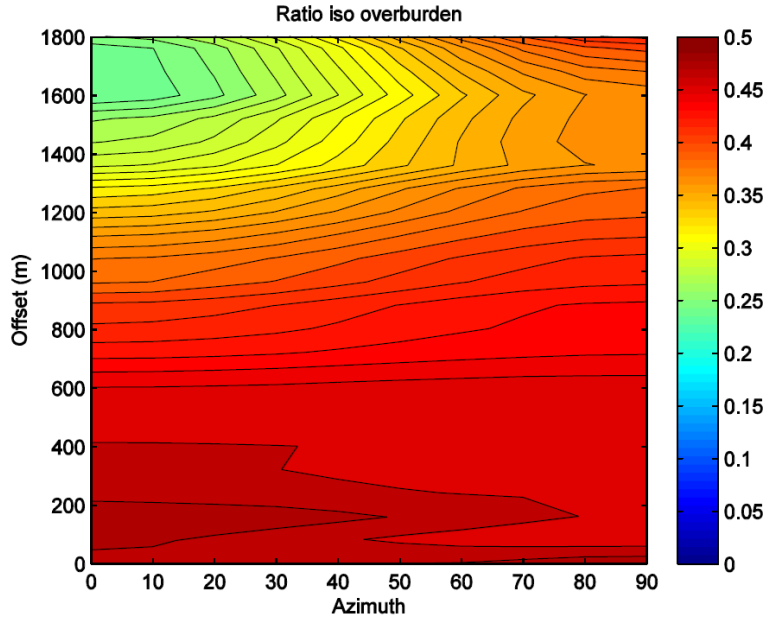

(a)

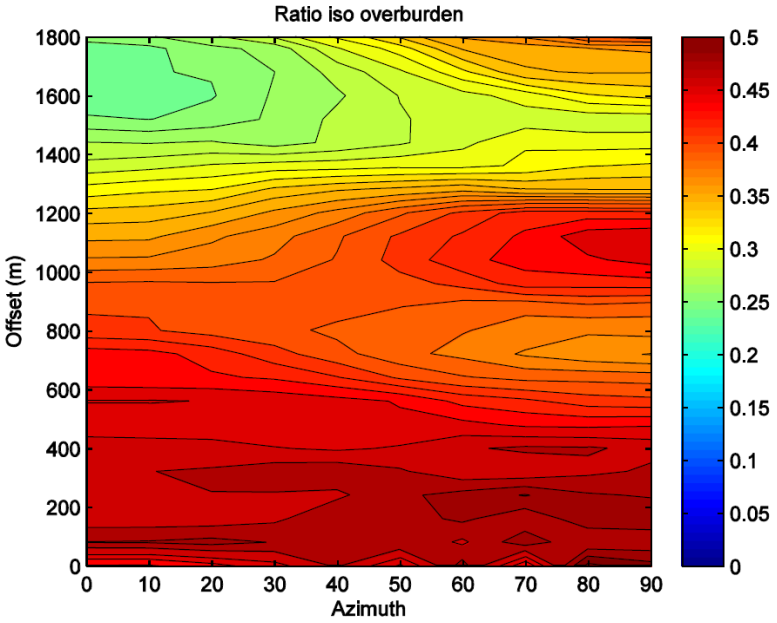

(b)

Figure 4.11: Ratio for reservoir top and a reflector below reservoir picks in the t-x domain for two models one with isotropic overburden (a) and the other with anisotropic overburden (b).

Chapter 5: Application to Real Data

STUDY AREA

Location and geology

The study area is located in the Arabian Peninsula. The target formation is an Upper Jurassic carbonate reservoir, composed primarily of limestone with associated traces of dolomite. The structure is defined by a NW-SE oriented, elongate-asymmetric, anticline that is doubly plunging. The anticline is controlled by a deep seated fault that cuts the section below the reservoir formation and ceases to cut the reservoir. The reservoir is overlain by an Anhydrite layer. It is hypothesized that the reservoir was affected by active faulting during Permo-Triassic and Early Jurassic times, and by compressive deformation during the Late Cretaceous-Early Tertiary times (Balharith, 2009).

Well logs and surface seismic data

In addition to conventional well logs such as acoustic sonic, density, gamma ray, porosity, caliper and shear sonic, FMI logs for four horizontal wells are also available for the study area. The trajectories of the horizontal wells intersect many target reservoir points. As a result, we have more control points to calibrate with seismic data. The seismic data consist of P-P pre-stack gathers. Wide-azimuth geometry is defined as geometries with a large aspect ratio (Inline /Crossline dimension). The P-P seismic dataset has an aspect ratio of 0.4 (Figure 5.1). Due to high fold density of the data at the target level, it is possible to extract a sufficient distribution of azimuths and offsets for

proper AVOA analysis. At each CMP bin, we are able to extract a subset of the data that has good sampling of source-receiver azimuths and offset, and each subset contains enough traces to fully populate each azimuth-range subclass (Jenner, 2002). This was done by extracting traces with offset that is less than 1800 m. As a result of this, the subset of the original data has an aspect ratio of 1, a more uniform offset distribution with respect to azimuth, and sufficient offset range to image the target horizon at a depth of approximately 1600 m (Figure 5.2) (Balharith, 2009).

Figure 5.3 shows the fold of the 3D seismic data after trimming, and Figure 5.4 shows a common shot point where we place the contribution from all receivers (pink dots) from all azimuths. This demonstrates that the acquisition geometry is indeed of wide azimuth and there is no bias toward any particular azimuth, which could hinder the AVOA analysis. The histogram of all offsets for the entire survey is shown in figure 5.5a where large offsets have higher trace counts. The histogram of the azimuths is displayed in figure 5.5b emphasizing that the distributions of trace count in all azimuths are equal.

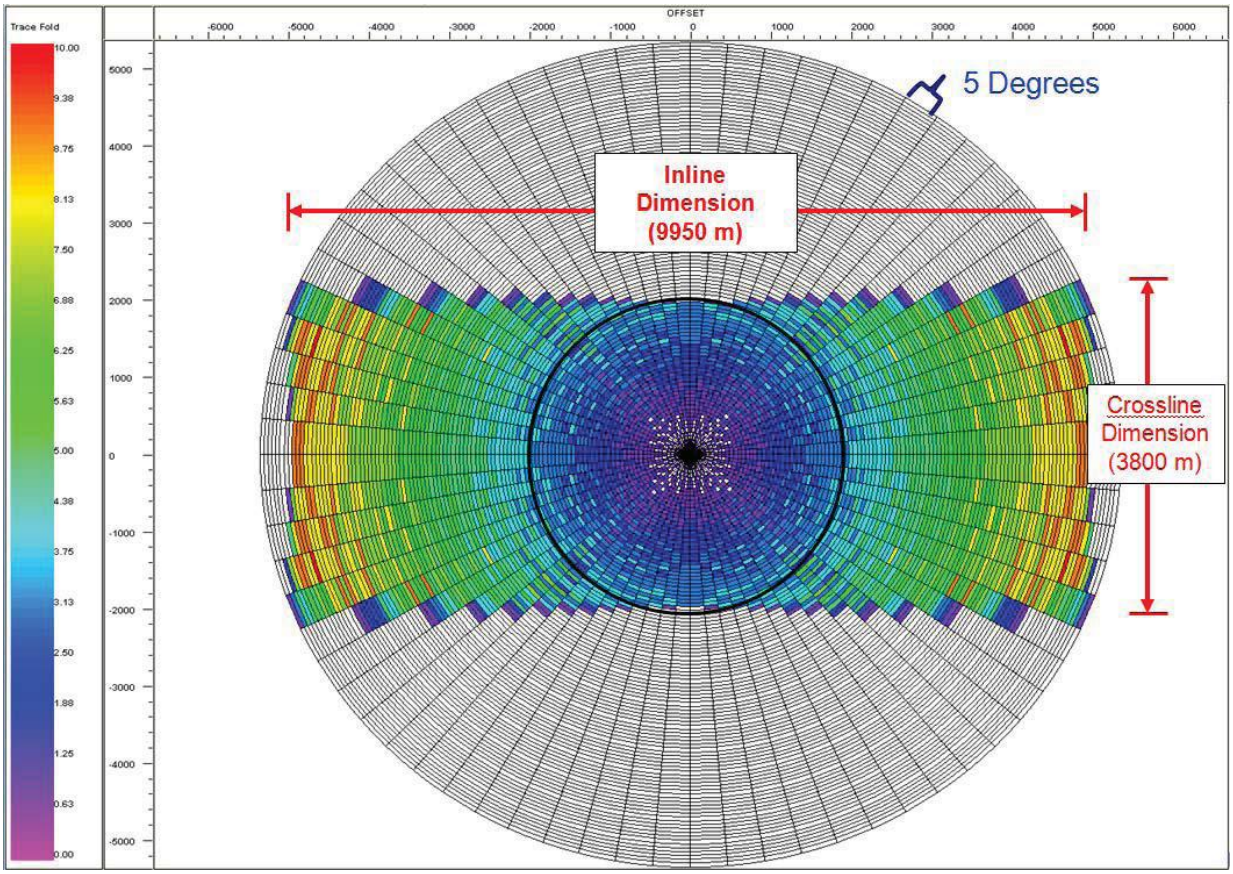

Figure 5.1: Offset-azimuth rose diagram of the 3D P-P seismic survey before trimming. The inline dimension is 9950m and crossline dimension is 3800m. Color bar indicates trace fold (Balharith, 2009).

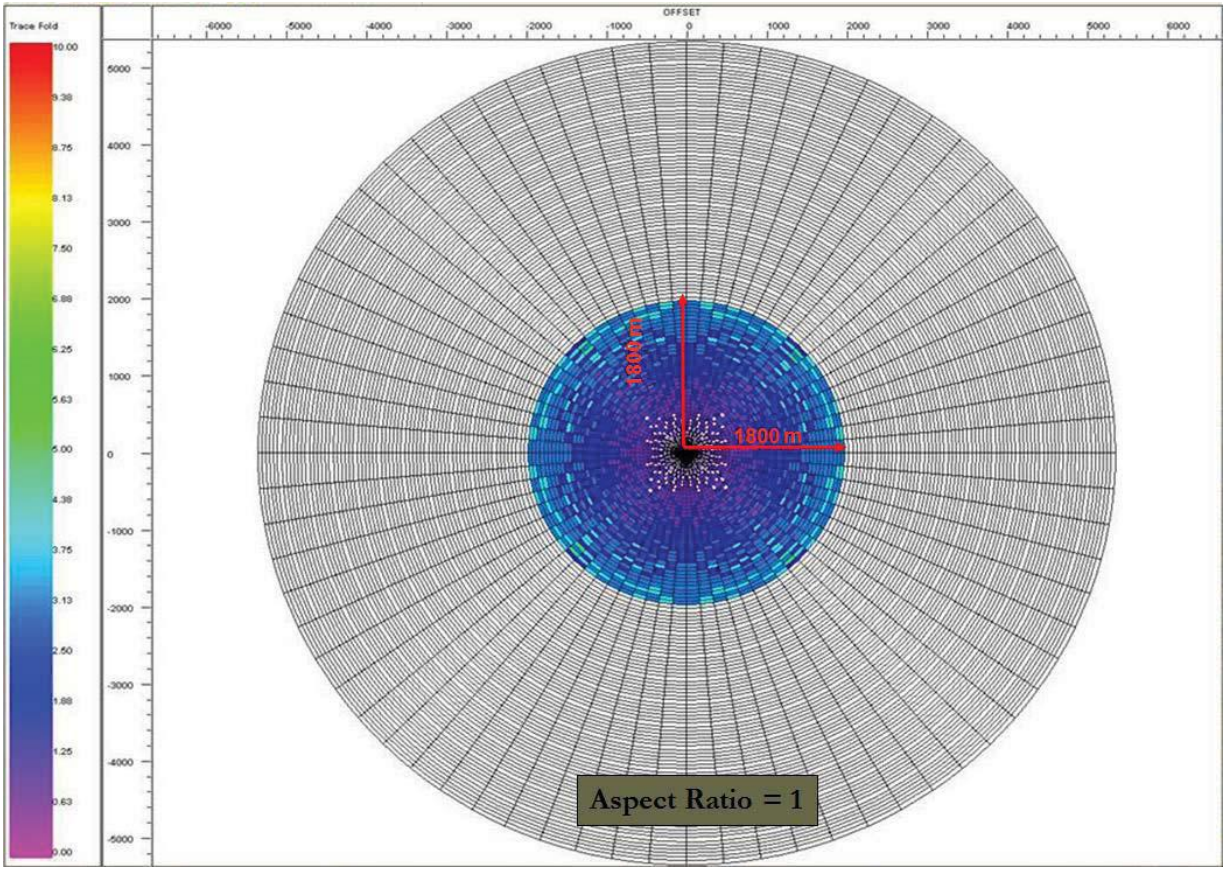

Figure 5.2: Offset-azimuth rose diagram of the 3D P-P seismic after editing. After trimming, the offset is limited to 1800m. Uniform color code means that we have equal distribution of azimuth (Balharith, 2009).

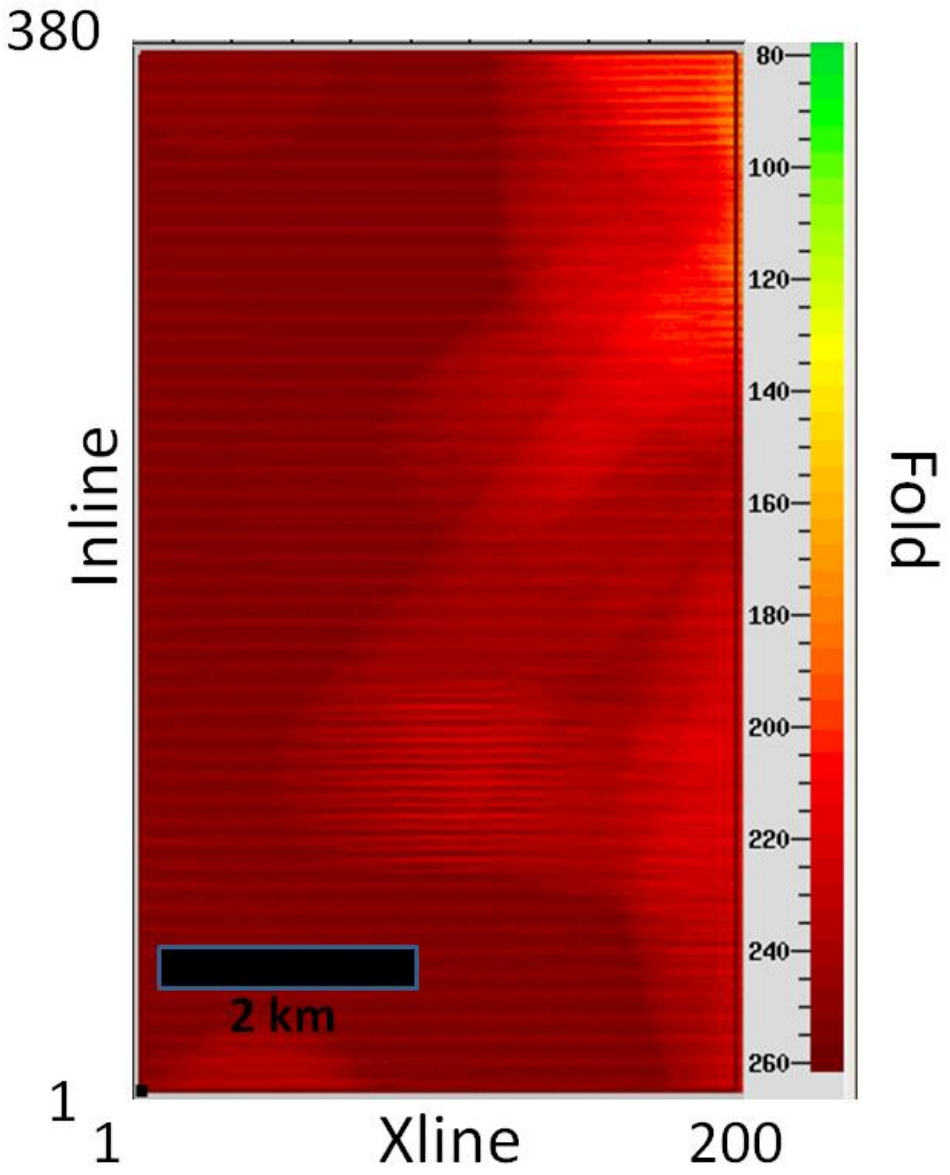

Figure 5.3: Fold of the 3D seismic. The color bar shows the fold count.

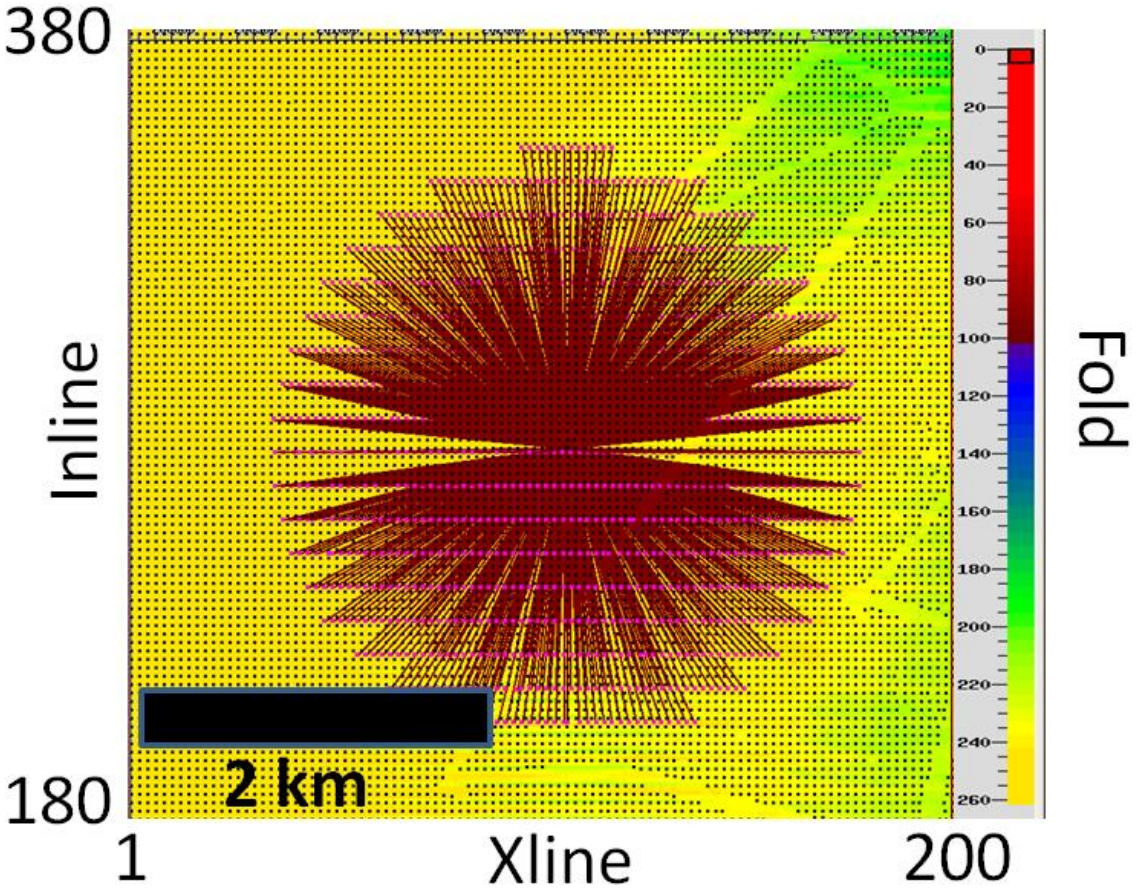

Figure 5.4: Common shot point where contribution from all receivers (pink dots) comes from all azimuths.

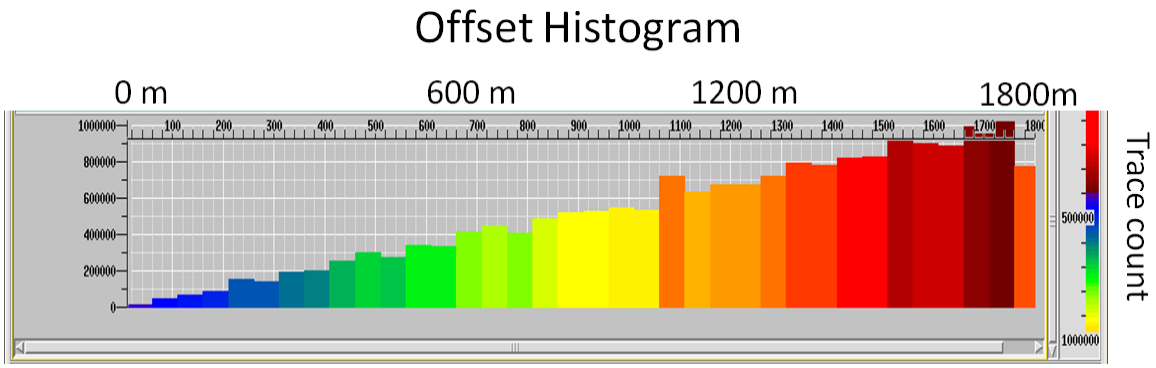

(a)

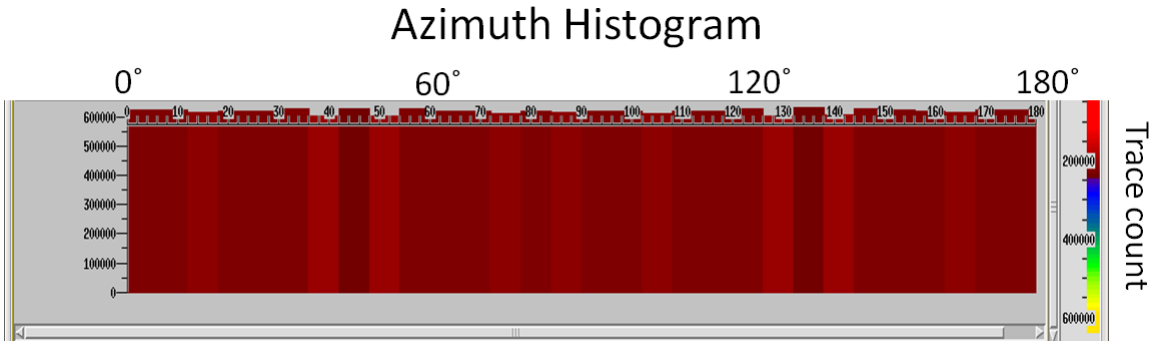

(b)

Figure 5.5: (a) Offset histogram for the entire survey where lager offsets have more trace count. (b) Azimuth histogram for the entire survey showing that distribution of azimuth is equal.

Several super bin gathers were generated by combining each of the 16 adjacent bins forming a 4 by 4 square. The uniformity of offsets and azimuths is further enhanced by this process. Figure 5.6 shows the travel time pick for the reservoir horizon where the seismic survey covers the west flank of the anticline structure. Figure 5.7 shows a post-stack section with overlain P-wave sonic log where the reservoir top is indicated by the red arrow. Correlation of one of the wells with post-stack section is shown in figure 5.8. The black arrow indicates the reservoir top horizon. The reservoir base reflector is not evident in seismic data and that is why the reflection form a reflector below the reservoir (blue arrow) is used instead in the ratio analysis.

AMPLITUDE PICKING IN TAU-P DOMAIN

The first step to applying the AVOA ratio method to real data requires taking CMP gathers containing all azimuths and decomposing them into ranges of azimuthal subsections. A range of 15 degrees is taken (Figure 5.9). Subsequently each azimuthal gather is transformed to tau-p domain using linear operator (slant stack). One CMP gather for 0-15˚ azimuth range is shown in t-x and in tau-p (figure 5.10 a and b). The two highlighted horizons are the reservoir top and the layer below reservoir picks respectively.

In order to obtain the ratio attribute discussed in the synthetic part of this study, amplitudes are to be picked for both reservoir top and for a reflector below reservoir in the tau-p domain for all decomposed azimuthal gathers for all CMPs in the 3D seismic survey. Clearly enough, the practicality of this method needs an automation process in order to pick amplitudes for all CMP gathers.

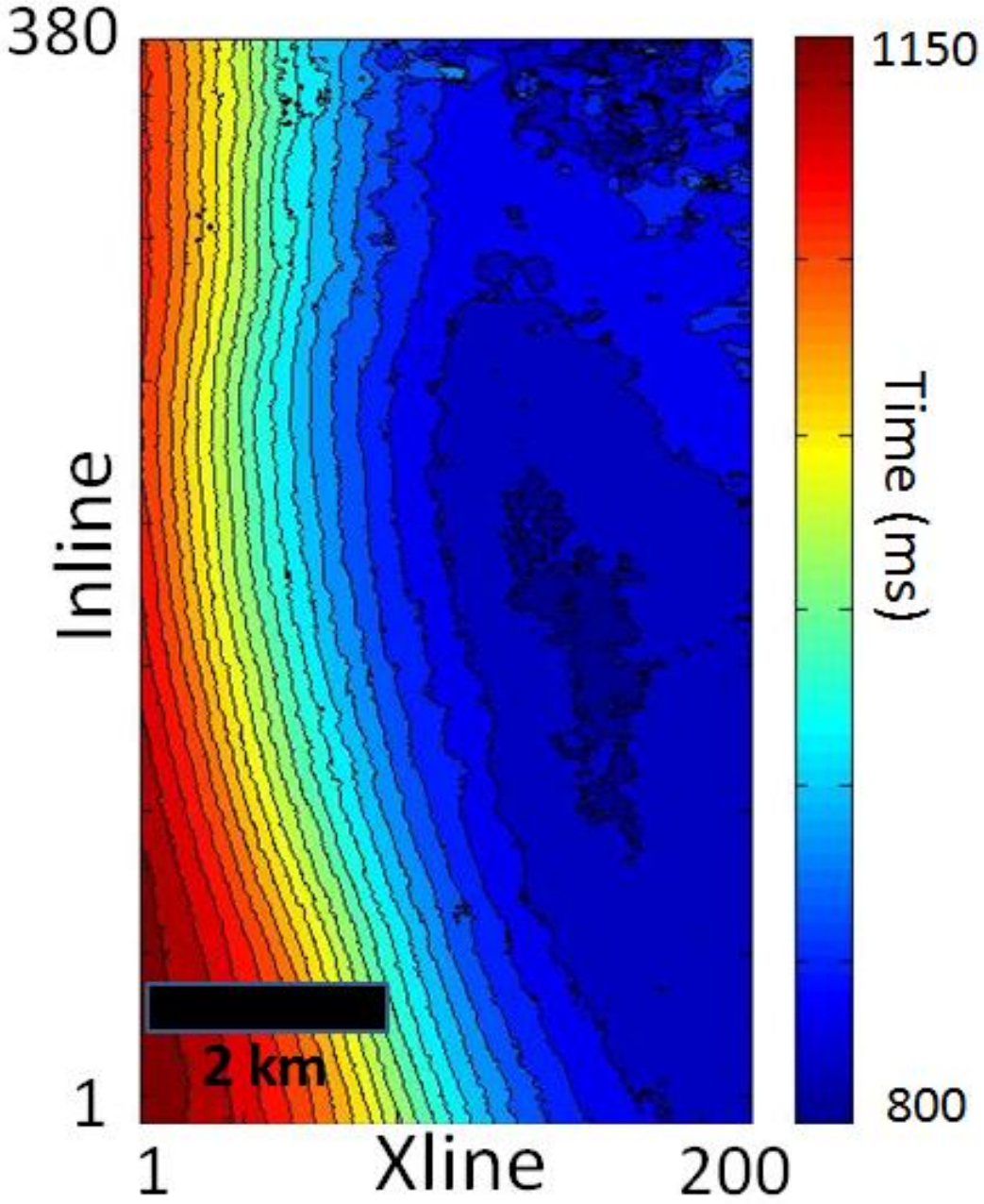

Figure 5.6: Reservoir time structure map.

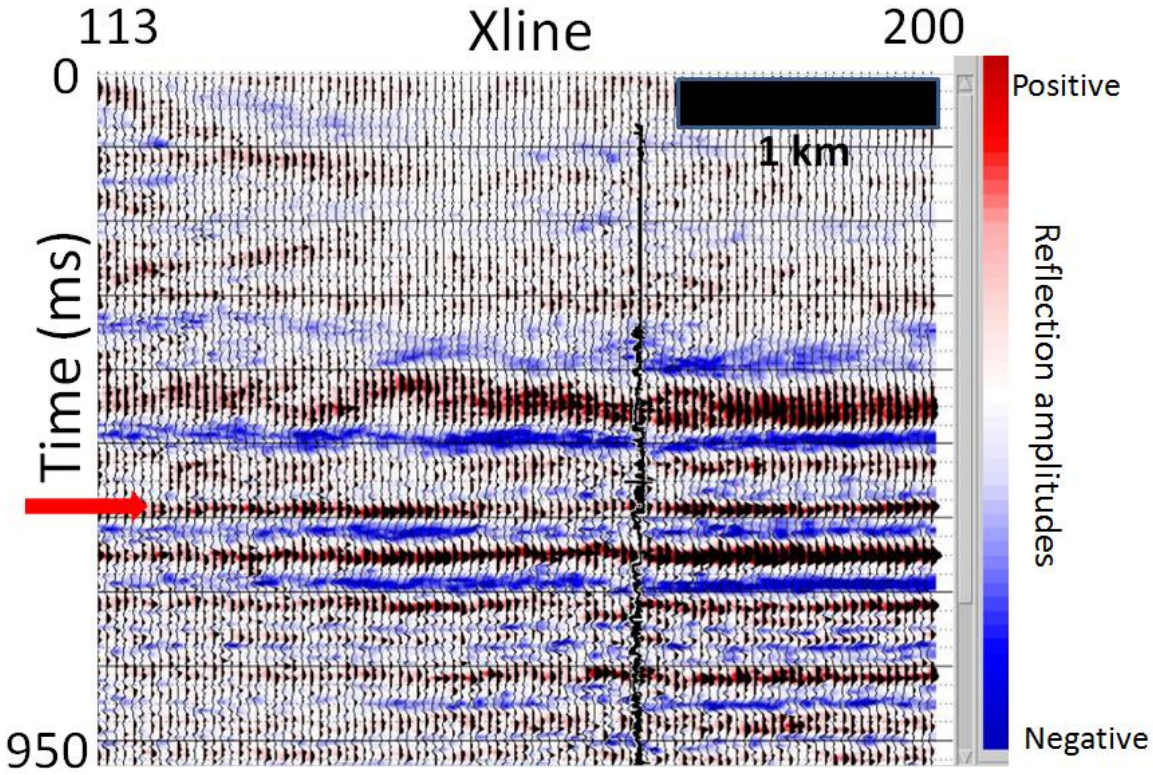

Figure 5.7: Post-stack seismic with P-wave sonic log overlaid. The reservoir horizon is indicated by the red arrow. It is flattened to a constant time.

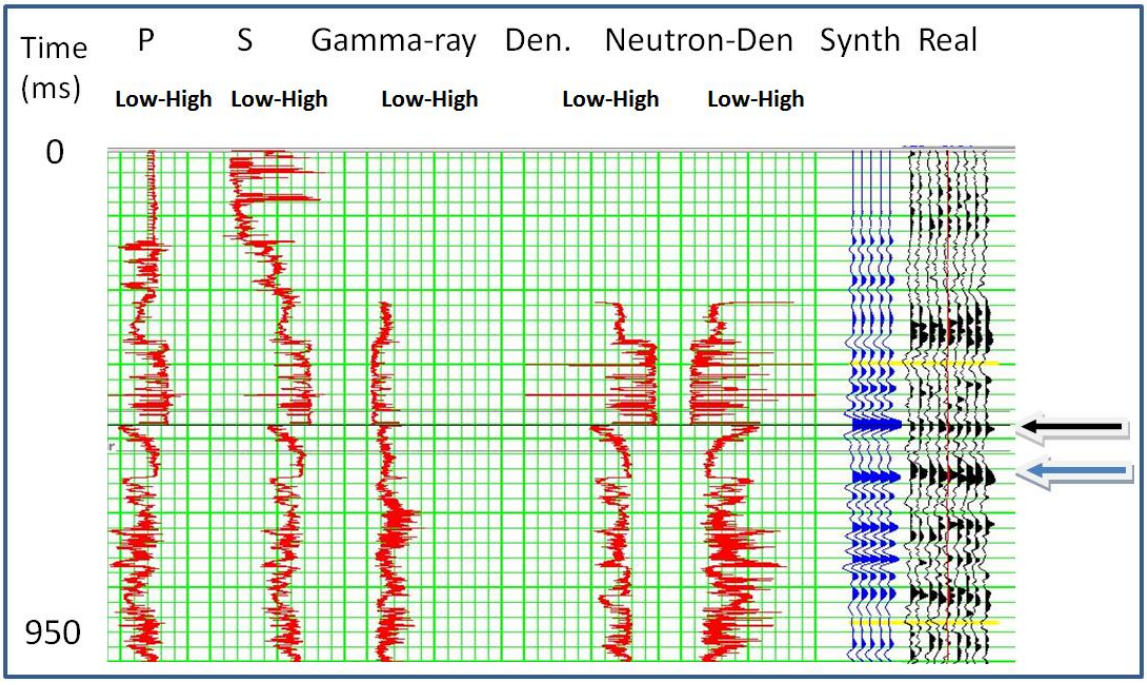

Figure 5.8: Correlation of one of the wells with a post-stack section is shown. The black and blue arrows indicate reflection horizons for reservoir and a reflector below the reservoir, respectively.

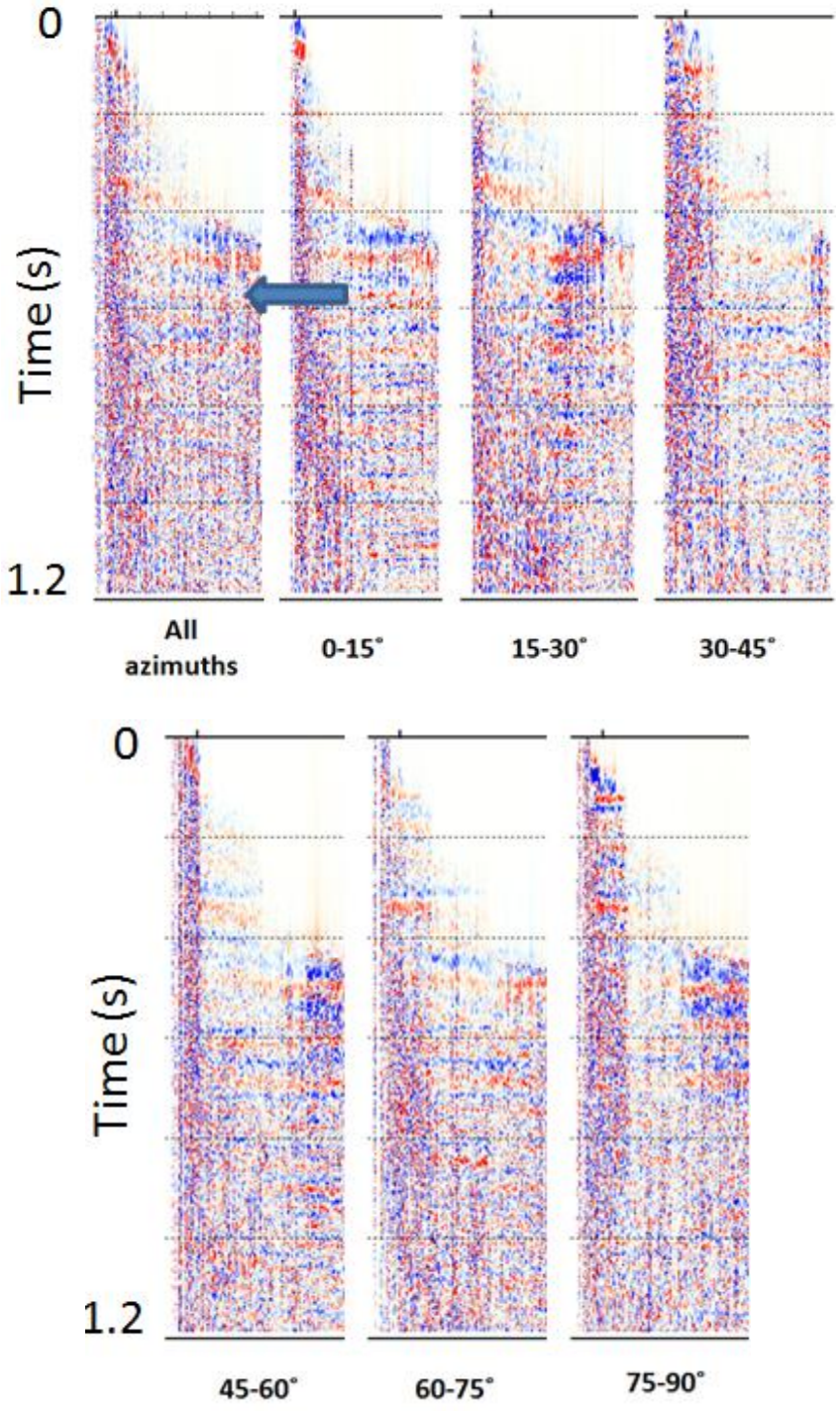

Figure 5.9: A CMP gather (top left panel) is decomposed into ranges of azimuthal gathers. The arrow shows the target horizon.

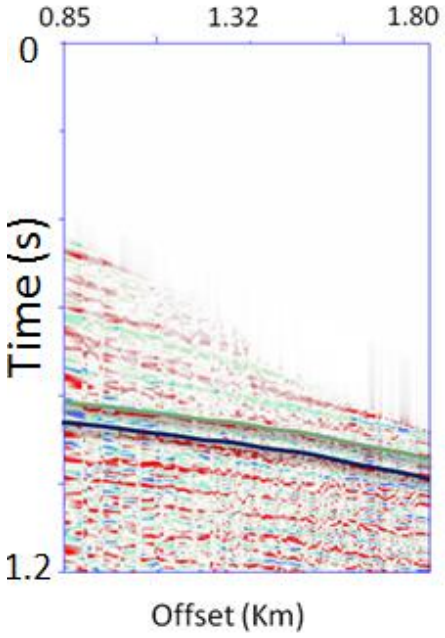

(a)

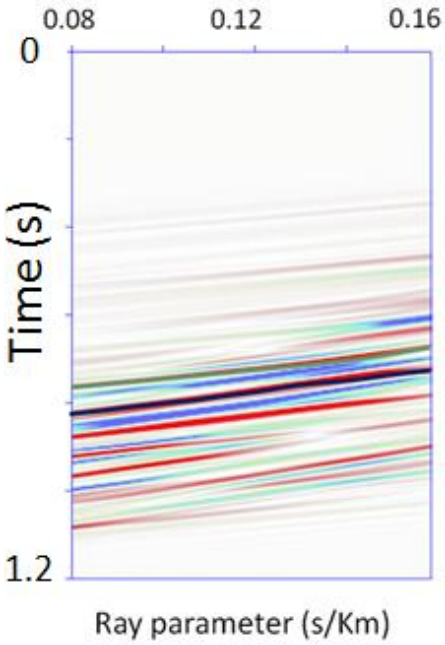

(b)

Figure 5.10: CMP gather for 0-15˚ azimuth range in x-t domain (a), and tau-p domain (b). The two highlighted lines correspond to reservoir top and for a reflector below reservoir, respectively.

This process is summarized in the following steps:

1. Start with NMO-corrected gathers where time picks of the two horizons are known
2. Remove NMO and calculate new horizons' time picks using the well known NMO equation:

$$t_{rnmo} = \sqrt{t_0 + (\frac{x^2}{v_{rms}})} \tag{5.1}$$

3. Calculate local slopes at all offsets which is equivalent to the ray parameter using:

$$p = \frac{\Delta t}{x} \tag{5.2}$$

4. Compute the value of tau using the slant stack transformation operator (Stoffa et al., 1981):

$$\tau = t_{rnmo} - px \tag{5.3}$$

5. Pick and extract amplitude on tau-p transformed gathers using both ray parameter and tau values from step 4

Figure (5.11 a-d) illustrates automation steps mentioned above for one representative CMP gather.

After picking all amplitudes for the entire 3D seismic survey for reservoir horizon and for a reflector below the reservoir, the ratio of amplitudes from both reflectors is taken in order to remove transmission effect from the overburden.

AVOA inversion of ratio attribute

An ellipse-fitting method is used to invert for two fracture properties: fracture direction and fracture density. Conventional AVOA analysis is usually applied to

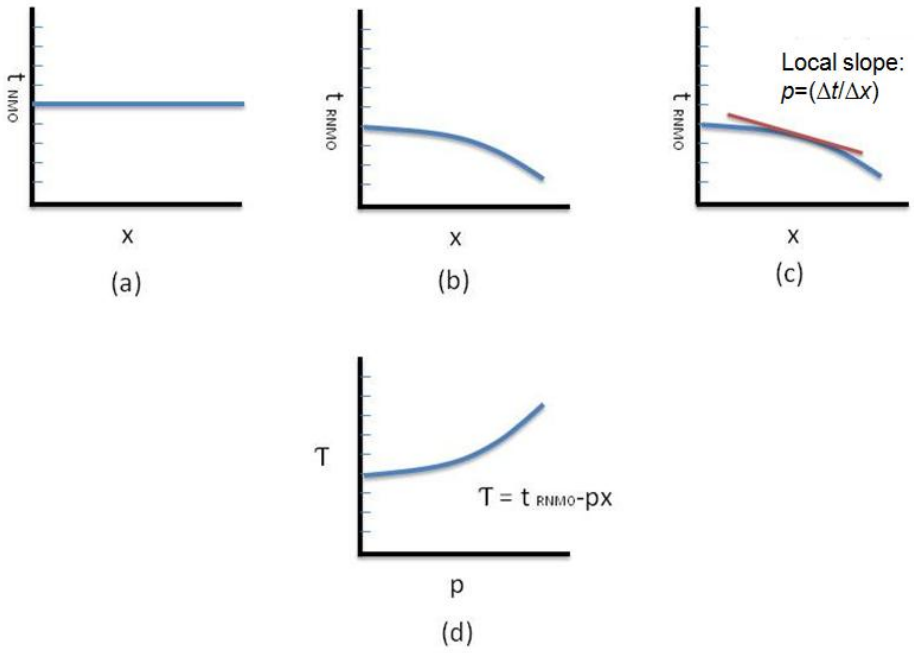

Figure 5.11: Automatic picking of amplitude in the tau-p domain. (a) NMO correct gather. (b) Reversed NMO gather. (c) Local slope calculation (p) for every value of x. (d) Tau value is predicted using both p calculated from (c) and time of RNMO from (b).

azimuthal amplitudes extracted in x-t domain. The same methodology is used but applied to the extracted ratio attribute where the overburden effect is assumed to be removed. The ratio attribute is a function of ray parameter and azimuth $R_{ratio}(p, \emptyset)$, and conversion from ray parameter to angle is needed for the AVOA inversion. The geology of the area is not complex, and the following relation is a good approximation (Biondi and Trisserant, 2004; Wang et al., 2003):

$$\sin(i) = \frac{V.p}{2\cos(\eta)}, \tag{5.4}$$

where i is the incident angle, η is the geological dip of target horizon and V is P-wave velocity above target. In order to compute horizon dip for the top reservoir pick, post-stack depth migration is performed. The reservoir horizon is picked on the new 3D volume and the horizon dip attribute is calculated. Figure 5.12a shows depth structure maps. The dip attribute is shown in Figure 5.12b. The horizon dip is almost flat in the east part of the anticline structure, and the dip increases to the west toward the flank of the anticline. Depending on dip, each CPD gather has a distinct range of angles as input to the AVOA inversion.

The following equations are used for the AVOA inversion (Grechka and Tsvankin, 1998, Al-Marzoug et al.,2006):

$$R(i, \emptyset) = A + [W_{11}cos^2\emptyset + 2W_{12}sin\emptyset cos\emptyset + W_{22}sin^2\emptyset]sin^2 i, \tag{5.5}$$

$$G_{max} = \frac{1}{2}(W_{11} + W_{22} + \Delta), \tag{5.6}$$

$$G_{min} = \frac{1}{2}(W_{11} + W_{22} - \Delta), \tag{5.7}$$

$$\Delta = [(W_{11} + W_{22})^2 + (2W_{12})^2]^{1/2}, \tag{5.8}$$

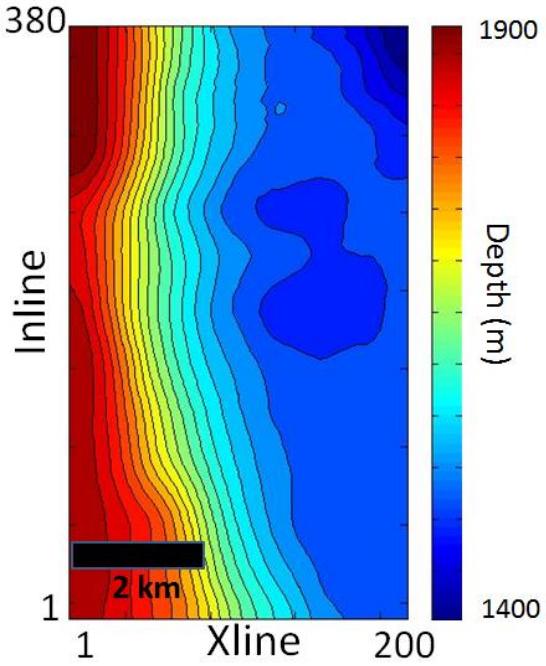

(a)

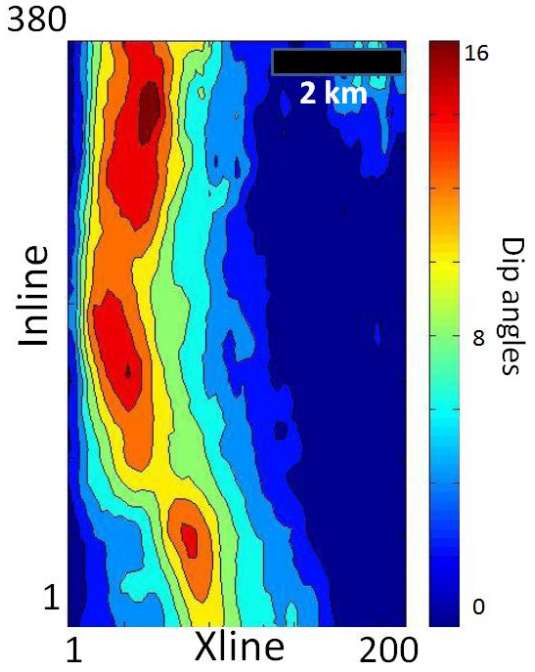

(b)

Figure 5.12: Depth structure map after post stack time migration (a) and corresponding dip angle map (b).

where $R(i, \emptyset)$ is the reflection coefficient as a function of the incidence angle and azimuth, respectively, and in our case $R_{ratio}(i, \emptyset)$ is used instead. A is the AVO intercept. W_{11}, W_{12} and W_{22} coefficients representing an azimuthally varying AVO gradient ellipse. The coefficients are solved using the least squares method. G_{max} and G_{min} are large and small semi-axes of the AVO gradient.

Fracture density is calculated using:

$$Fracture\ den = \frac{(G_{max} - G_{min})}{G_{ave}}, \tag{5.9}$$

where G_{ave} is the average gradient. Fracture direction attribute is computed using:

$$Fracture\ dir = \tan^{-1}\left[\frac{W_{22} - W_{11} + \sqrt{(W_{22} - W_{11})^2 + 4{W_{12}}^2}}{2W_{12}}\right], \tag{5.10}$$

Figure 5.13 shows the inversion result for fracture density and a smoothed version is shown in figure 5.14. Hot colors indicate high fracture density values. It can be seen that there is coherency on the inverted attribute indicating a good level of confidence on the inversion results. It is also noted that the fracture density attribute is similar to the anticline structure highlighted by the dip angle map in figure 5.12b where values are elongated north-south direction.

An important observation is that the hinge of the elongate-asymmetric anticline has high fracture density. Nelson (2001) showed a diagram (figure 5.15) of the frequency of fracture intensity measurements for fold-related fractures measured in Mississippian carbonate outcrops in the thrust belt in western Alberta. It shows a similar finding where

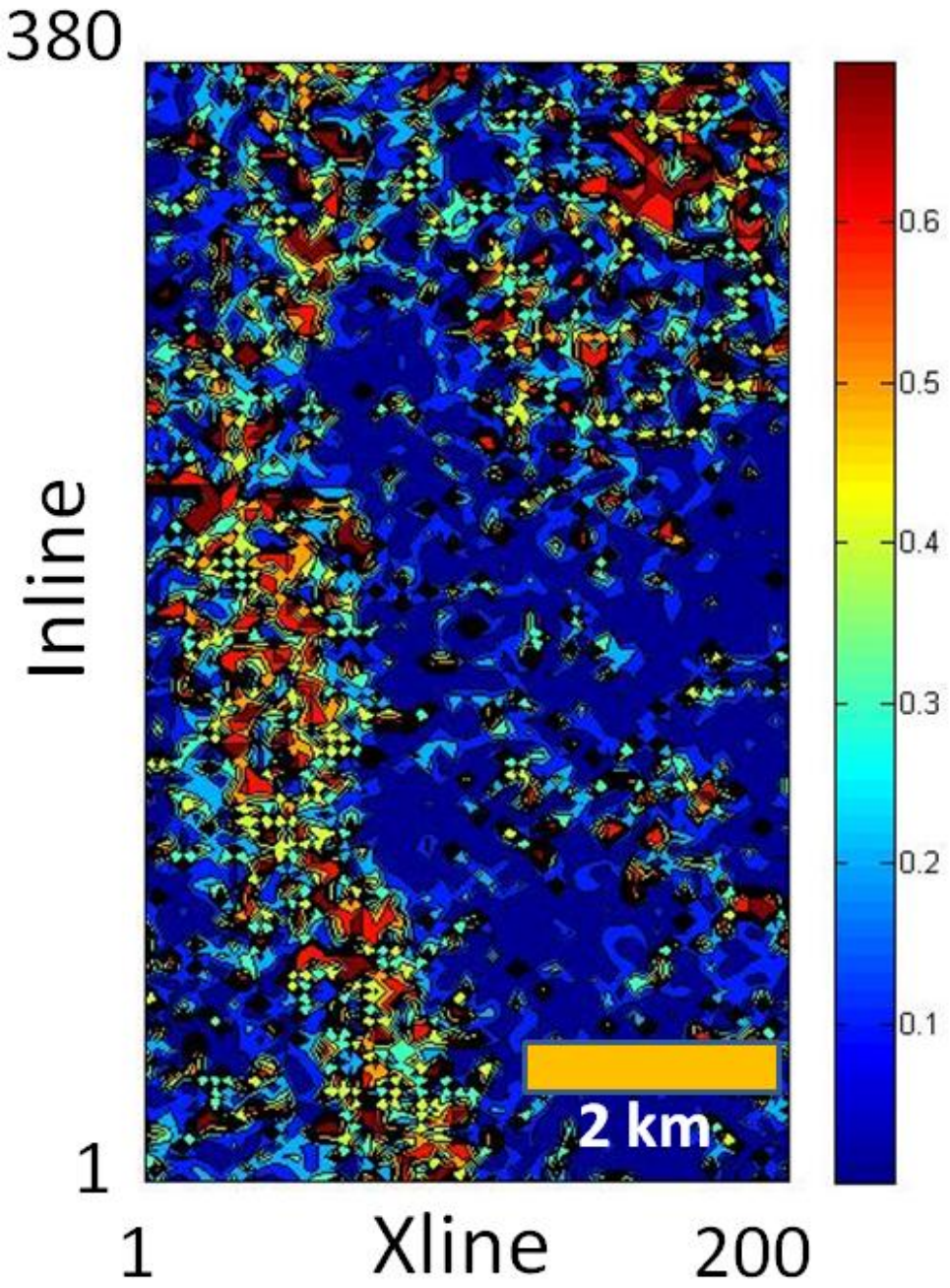

Figure 5.13: Inverted fracture density map.

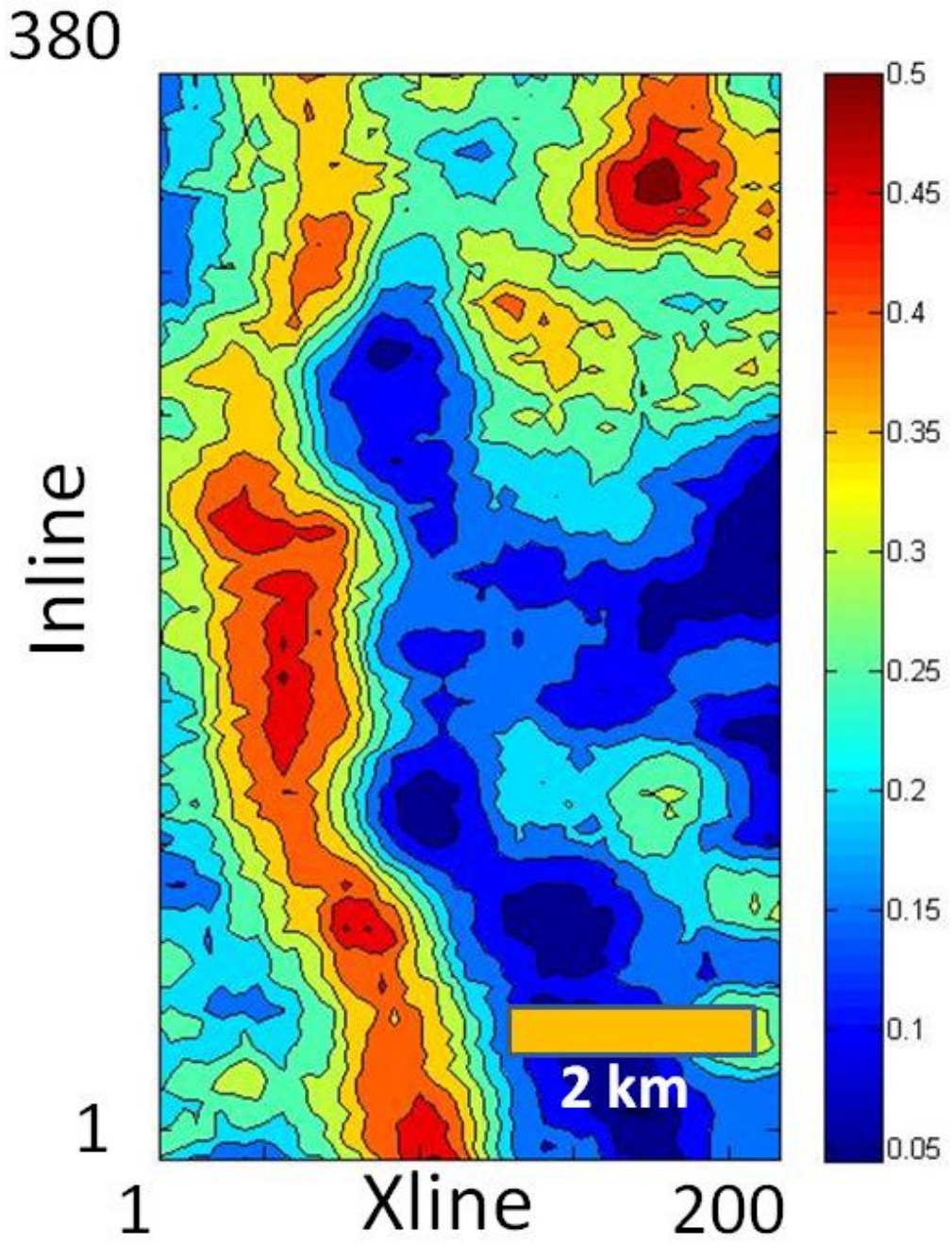

Figure 5.14: Inverted fracture density map (smoothed).

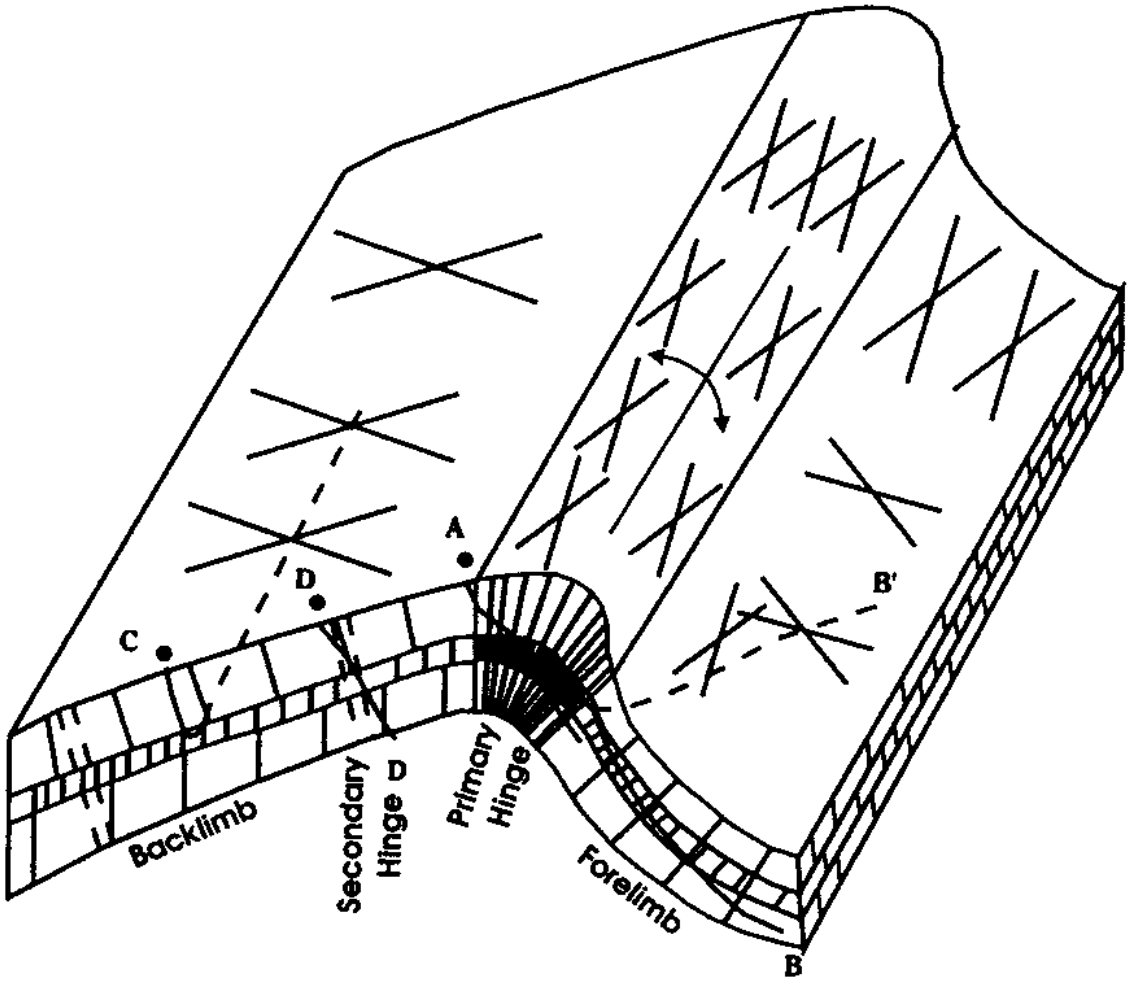

Figure 5.15: Frequency of fracture intensity measurements for fold-related fractures measured in Mississippian carbonate outcrops in the thrust belt in western Alberta (Nelson, 2001).

the hinge of the anticline has relatively high fracture density. The north-east part of the density map has high values, and this is related to the bad quality of seismic section at that area.

Inversion results for the fracture direction attribute can be seen in figure 5.16. There is some coherency in the attribute along north-south trends, and the best way to check the integrity of the inversion result is to compare it to the FMI log. Figure 5.17a is a rose diagram computed from FMI logs. The rose diagram computed from the seismic data is shown in figure 5.17b. The corresponding histograms can be seen in figures 5.18 a and b. Results from both FMI logs and seismic inversion have a general NW-SE fracture direction. Further analysis is done where fracture direction values that corresponds to low fracture density are muted and the resulting map is shown in figure 5.19. We can see that the general fracture trend is WNW-ESE in areas that correspond to high density values. The rose diagram and histogram for the selected high density areas (Figure 5.20 a and b) highlight the WNW-ESE dominant fracture direction.

Post stack seismic attributes

Despite the fact that stacking is an averaging process that eliminates offset and azimuth information, post-stack information can be valuable. In this section I use curvature and coherency attributes, which are used to obtain valuable information about faults and fractures (Chopra and Marfurt, 2005). The structural geology relationship between the curvature attribute and fractures is well established (Lisle, 1994). Hart et al. (2002), Sigismonodi and Soldo (2003), Masaferro et al. (2003), and others have used the

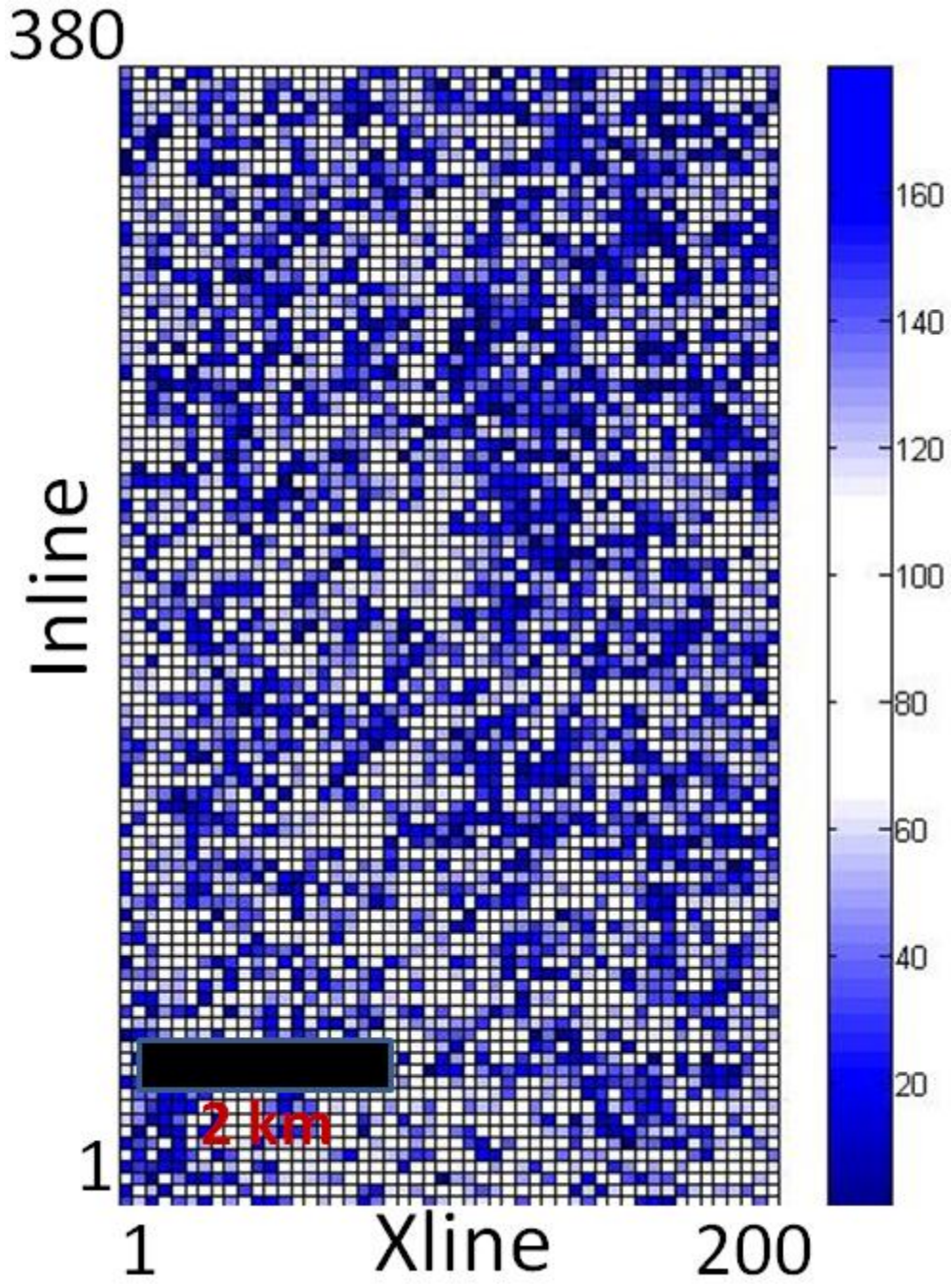

Figure 5.16: Inverted fracture direction attribute. 90 degree azimuth indicates (east-west) fracture direction and 0 and 180 degree azimuth correspond to fractures oriented (north-south) direction.

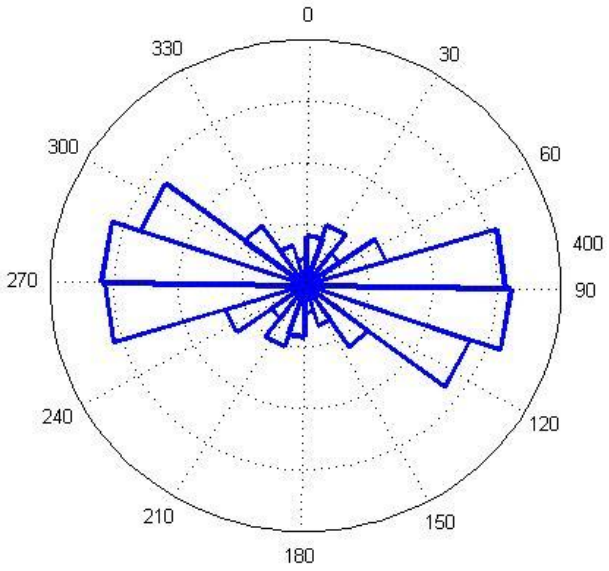

(a)

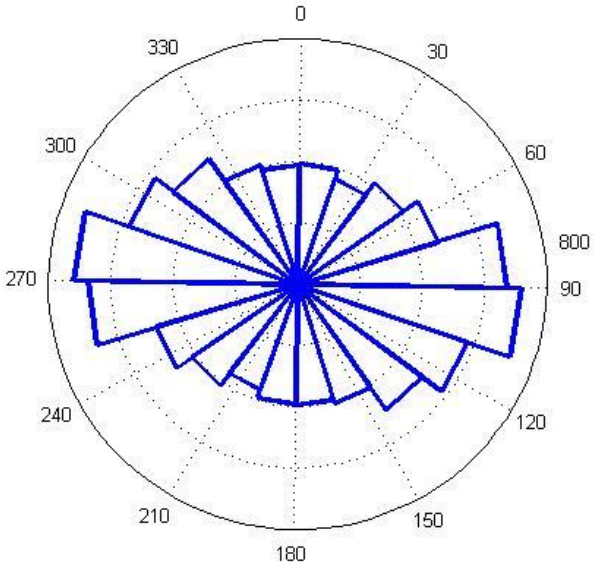

(b)

Figure 5.17: Rose diagram from FMI logs (a). (b) Shows a rose diagram from inverted fracture direction attribute from seismic. The dominant fracture direction of both FMI logs and seismic is (WNW-ESE).

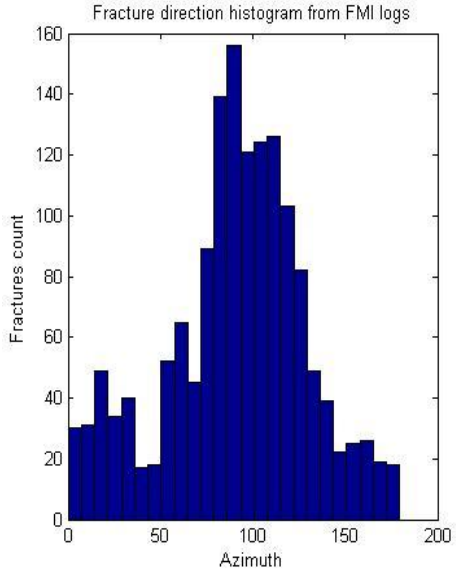

(a)

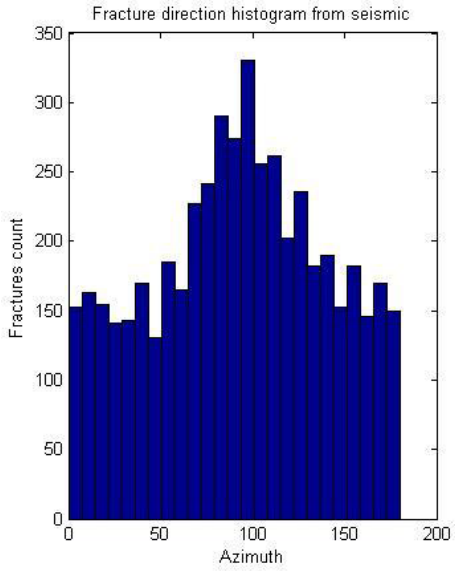

(b)

Figure 5.18: Rose diagram from FMI logs (a). (b) Shows a rose diagram from inverted fracture direction attribute from seismic. The dominant fracture direction of both FMI logs and seismic is (WNW-ESE).

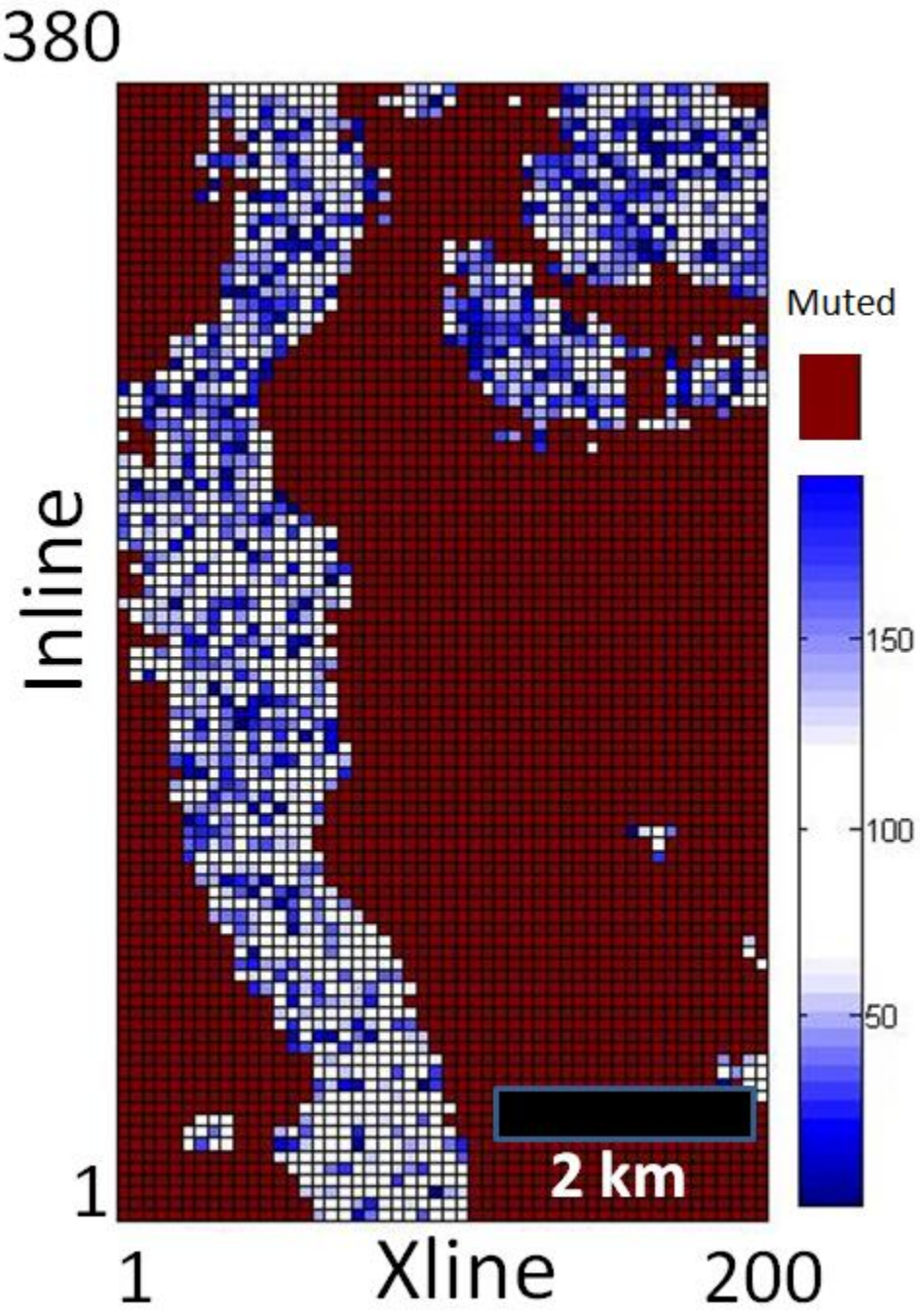

Figure 5.19: Inverted fracture direction attribute. 90 degree azimuth indicates (east-west) fracture direction and 0 and 180 degree azimuth correspond to fractures oriented (north-south) direction. Values that corresponds to low fracture density are muted.

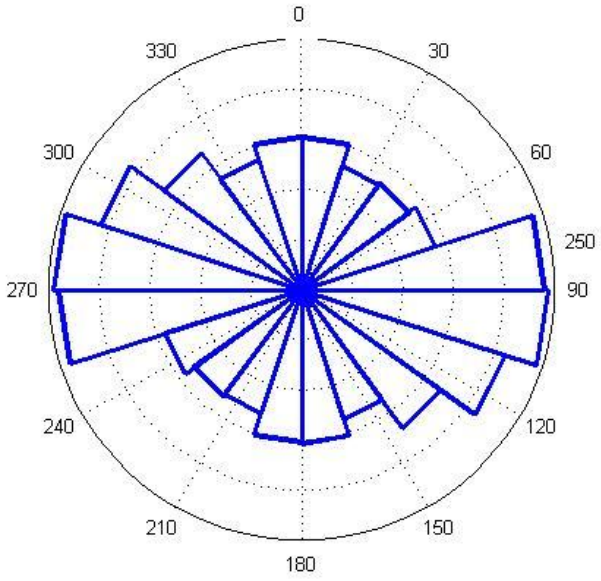

(a)

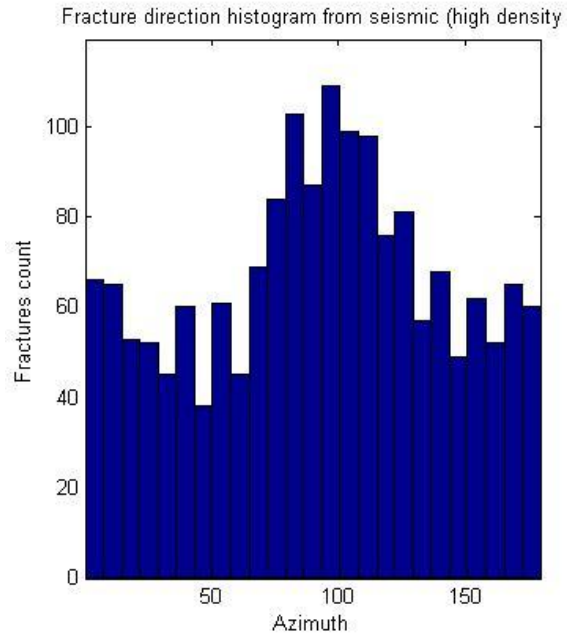

(b)

Figure 5.20: Rose diagram from FMI logs (a). (b) Shows a rose diagram from inverted fracture direction attribute from seismic The dominant fracture direction of both FMI logs and seismic is (WNW-ESE).

curvature attribute to map subtle features and predict fractures. The attribute is a 3D property of a quadratic surface that quantifies the degree to which the surface deviates from being planar. It helps in removing the effects of regional dip and emphasizes small scale features associated with depositional features or small-scale faults (Chopra and Marfurt, 2005). The coherency attribute is a measure of lateral changes in the seismic response caused by variation in structure, stratigraphy, porosity, lithology, and the presence of hydrocarbons (Marfurt et al., 1998). The currency attribute is based on the idea of computing and mapping a normalized cross-correlation between adjacent traces in the same survey (Bahorich and Farmer, 1995).

Attributes are derived from amplitudes extracted from the top reservoir pick. Figure 5.21 shows top reservoir amplitudes. An F-X filter is applied for optimum attribute results (figure 5.22). Consequently, the coherence attribute is computed (figure 5.23). It can be seen that there are some areas of high coherency indicating (brown color) low fracture zones. On the other hand, low coherency areas (white color) imply high fracture density. The curvature map (figure 5.24) shows that high values (red color) correspond to high fracture density and low values (blue color) indicate low fracture zones.

It is important to note that there is a good correlation between post-stack coherence and curvature attributes and the pre-stack ratio attribute. Both pre-stack and post-stack methods give the conclusion that high fracture density values are located at the hinge of the anticline structure.

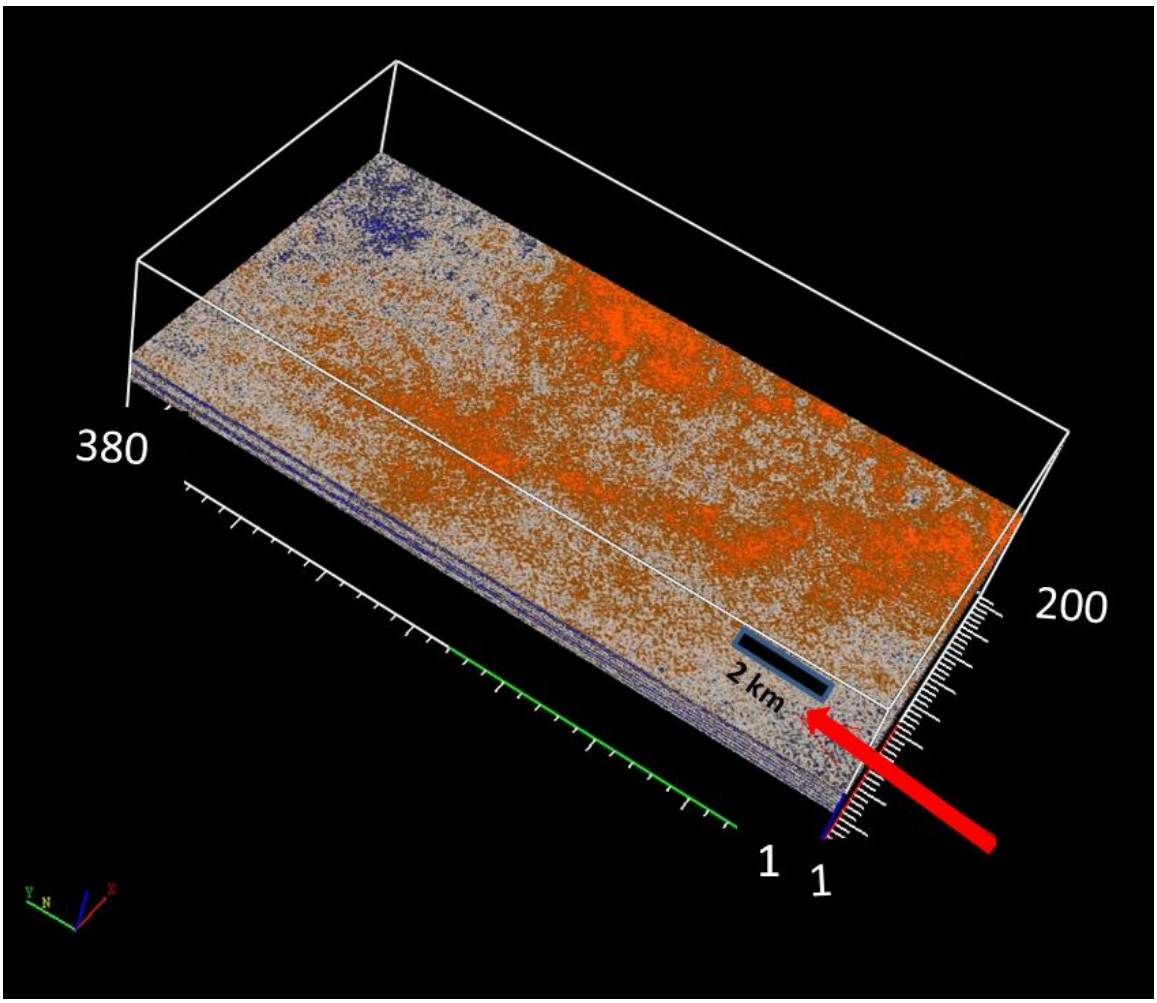

Figure 5.21: Top reservoir amplitude map. The red arrow indicates north direction.

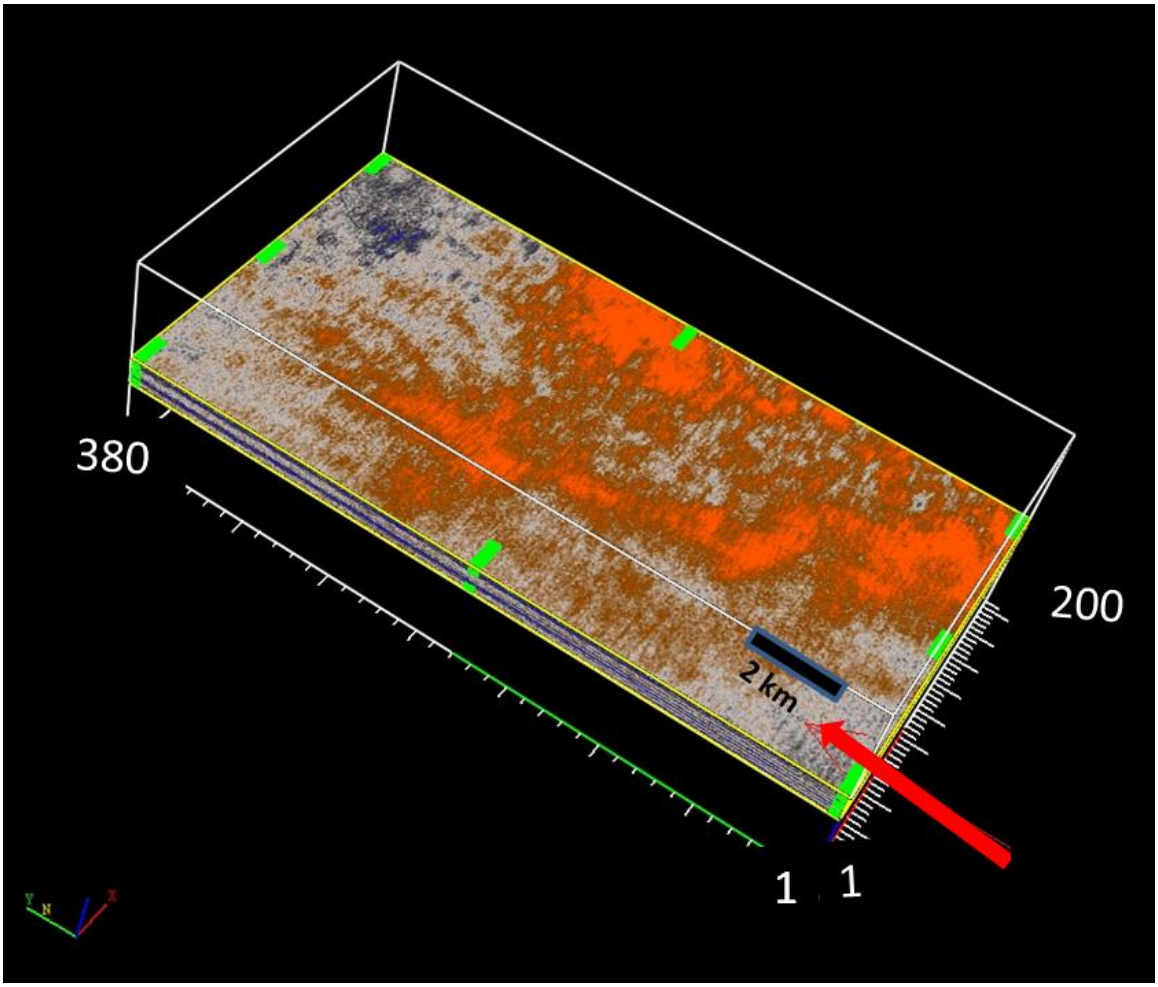

Figure 5.22: Top reservoir amplitude map after applying F-X filter. The red arrow indicates north direction.

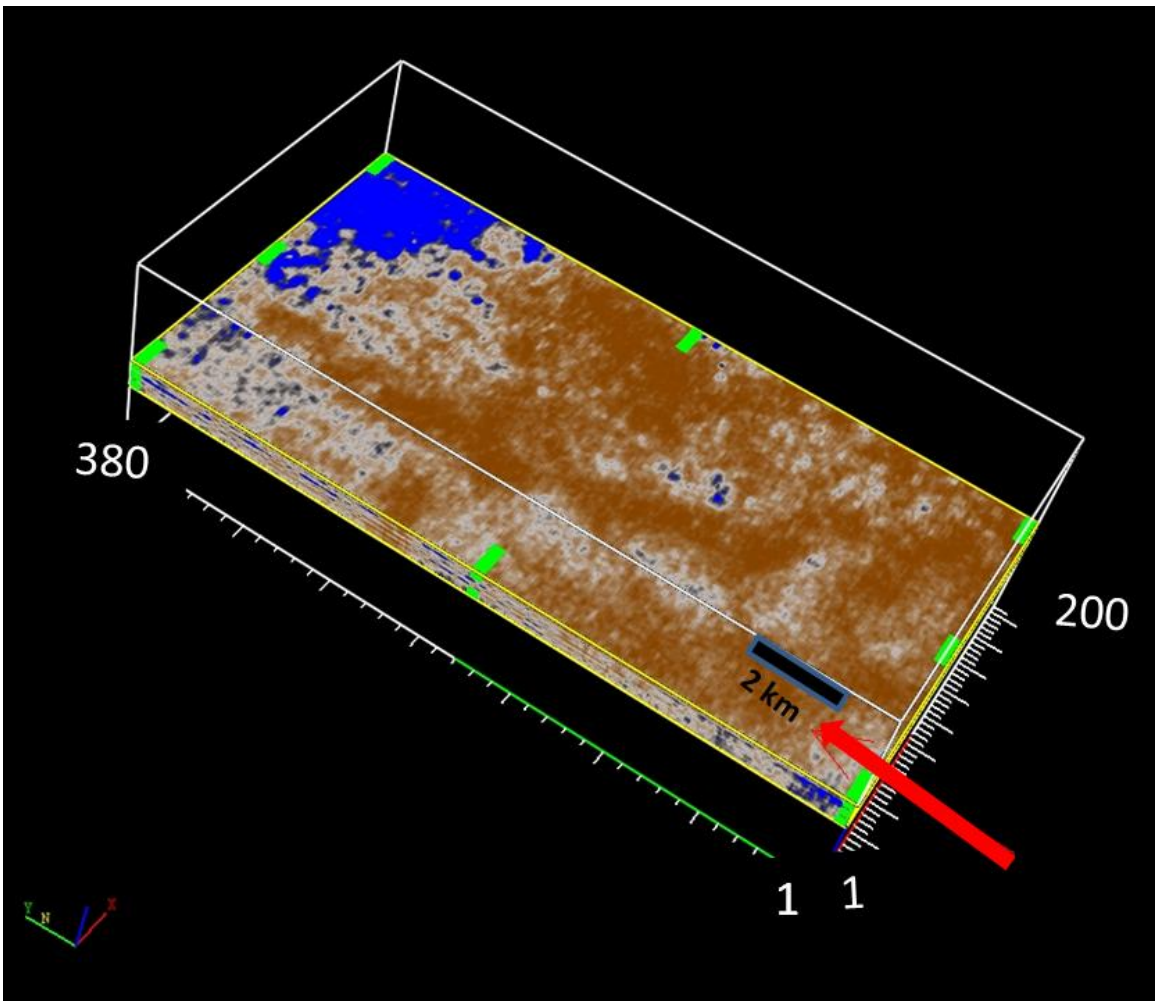

Figure 5.23: Top reservoir coherence map. Brown color corresponds to high coherence values and white color indicates low coherence values. The red arrow indicates north direction.

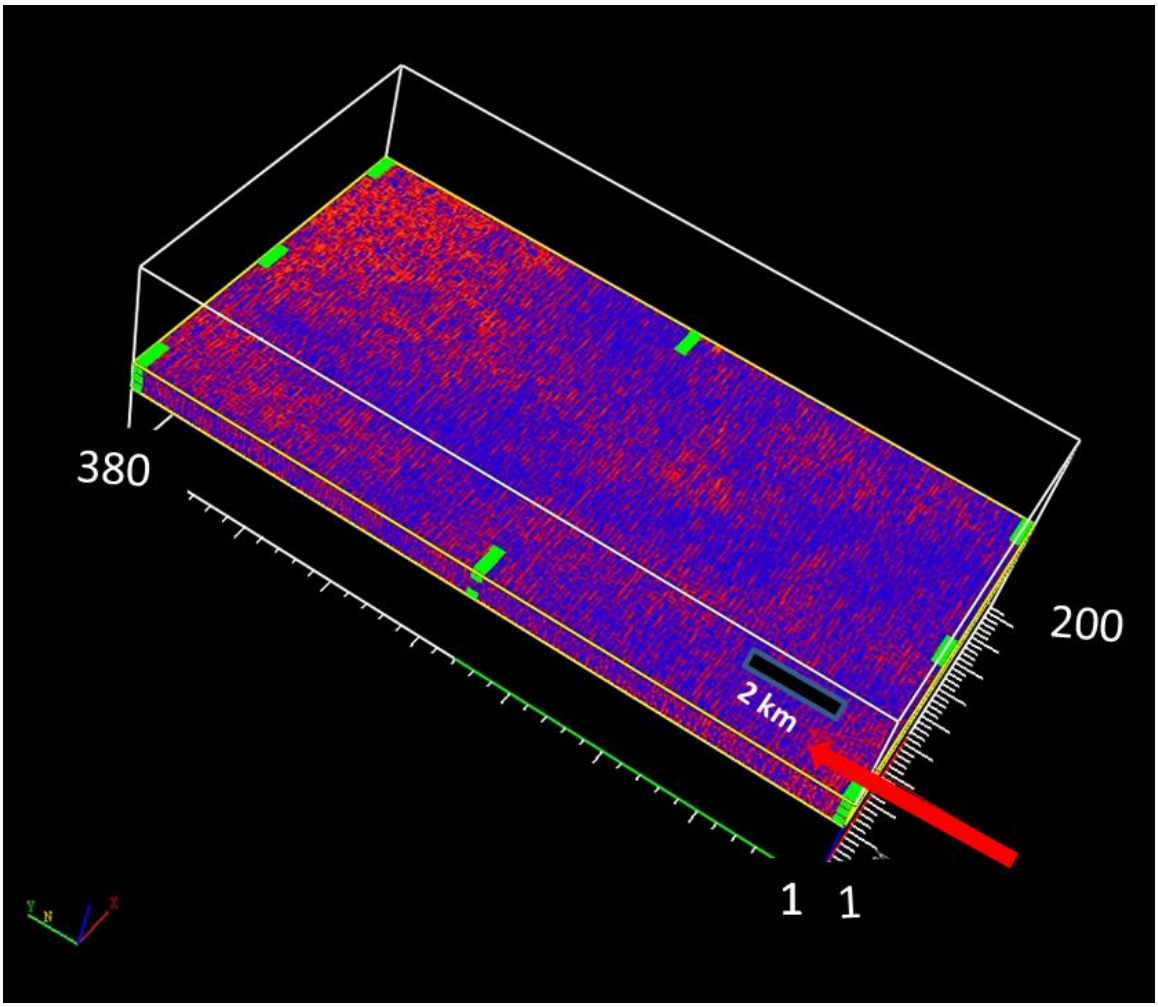

Figure 5.24: Top reservoir coherence map. Red color corresponds to high coherence values and white color indicates low coherence values. The red arrow indicates north direction.

SUMMARY

The ratio method was applied to a P-P 3D dataset from the Arabian Peninsula. Fracture density inversion results indicate greater fracturing in the hinge zone of the anticline structure, which agree very well with the structural geology of the anticline. Fracture orientation inversion results agree with FMI logs where fractures have a WNW-ESE trend. Fracture directions show a general WNW-ESE trend within a selected zone where fractures are believed to have high density.

Post-stack coherency and curvature attributes correlate well with the ratio method. This indicates that new pre-stack proposed ratio method gives reliable results despite the low signal to noise problem of pre-stack gathers. Even though post-stack attributes look similar to those of pre-stack, they are not suitable for quantitative estimation of fracture parameters. A method to determine fracture weaknesses from pre-stack data is described in the next chapter.

Chapter 6: Inversion of Normal and Tangential Weaknesses

INTRODUCTION

In this chapter I perform a quantitative analysis of reservoir fracture properties namely, fracture normal and tangential weaknesses or ΔN and ΔT, respectively. To test the accuracy of results, the inversion is first performed on synthetic data generated in chapter 4. The first step is to do a conventional inversion using AVOA data and see which parameter is reliable. The second step is to apply the inversion to the ratio attribute derived in chapter 4. The last step is to perform the inversion on real data using the ratio method where the overburden effect is believed to have been removed.

THEORY

The starting point of the derivation is the fundamental idea of linear-slip theory (Schoenberg and Sayers, 1995), which states that fractures can be represented as either infinitely thin and high compliant layers or planes of weakness with linear-slip or non-welded boundary conditions (Bakulin et al., 2000). The displacement discontinuity $[u]$ is assumed to be linearly related to the stress traction (σ), which is continuous across the interface (Schoenberg, 1980). The equations describing displacement and stress across an interface are:

$$[\sigma_{11}] = [\sigma_{12}] = [\sigma_{13}] = 0, \tag{6.1}$$

$$[u_1] = h(K_N\sigma_{11} + K_{NH}\sigma_{12} + K_{NV}\sigma_{13}), \tag{6.2}$$

$$[u_2] = h(K_{NH}\sigma_{11} + K_H\sigma_{12} + K_{VH}\sigma_{13}), \tag{6.3}$$

$$[u_3] = h(K_{NV}\sigma_{11} + K_{VH}\sigma_{12} + K_V\sigma_{13}). \tag{6.4}$$

where h is the average distance between the fractures and the brackets denote the jump of the values across the interface. σ_{11} is the normal stress, σ_{12} and σ_{13} are shear stresses. u_1, u_2 and u_3 are displacements in x, y and z directions respectively. K_N, K_V, K_H, K_{NV}, K_{NH} and K_{VH} are fracture compliances relating the jump of displacement to stress.

A medium that is homogeneous and isotropic and embedded with a set of parallel vertical fractures can be represented by the liner slip model; the effective stiffness matrix is derived by Schoenberg and Sayers (1995):

$$C = (\lambda + 2\mu)[C^b - C^f], \tag{6.5}$$

$$C^b = \begin{bmatrix} 1 & x & x & 0 & 0 & 0 \\ & 1 & x & 0 & 0 & 0 \\ & & 1 & 0 & 0 & 0 \\ & & & g & 0 & 0 \\ & & & & g & 0 \\ & & & & & g \end{bmatrix}, \tag{6.6}$$

$$C^f = \begin{bmatrix} \Delta N & x\Delta N & x\Delta N & 0 & \sqrt{g}\Delta NV & \sqrt{g}\Delta NH \\ & x^2\Delta N & x^2\Delta N & 0 & x\sqrt{g}\Delta NV & x\sqrt{g}\Delta NH \\ & & & 0 & x\sqrt{g}\Delta NV & x\sqrt{g}\Delta NH \\ & & & 0 & 0 & 0 \\ & & & & g\Delta V & g\sqrt{g}\Delta VH \\ & & & & & g\Delta H \end{bmatrix}, \tag{6.7}$$

where λ and μ are Lame's parameters, $g = \frac{\mu}{\lambda+2\mu} = \frac{V_s^2}{V_p^2}$. $x = \frac{\lambda}{\lambda+2\mu} = 1 - 2g$, and the fracture weaknesses are defined by:

$$\Delta N = \frac{(\lambda+2\mu)K_N}{1+(\lambda+2\mu)K_N}, \tag{6.8}$$

$$\Delta NV = \frac{\sqrt{\mu(\lambda+2\mu)}K_{NV}}{1+\sqrt{\mu(\lambda+2\mu)}K_{NV}}, \tag{6.9}$$

$$\Delta V = \frac{\mu K_V}{1+\mu K_V}, \tag{6.10}$$

$$\Delta NH = \frac{\sqrt{\mu(\lambda+2\mu)}K_{NH}}{1+\sqrt{\mu(\lambda+2\mu)}K_{NH}}, \tag{6.11}$$

$$\Delta H = \frac{\mu K_H}{1+\mu K_H}, \tag{6.12}$$

$$\Delta VH = \frac{\sqrt{\mu(\lambda+2\mu)}K_{VH}}{1+\sqrt{\mu(\lambda+2\mu)}K_{VH}}. \tag{6.13}$$

The fracture stiffness matrix in equation (6.7) corresponds to a medium with monoclinic symmetry. Two assumptions are made in order to reduce the symmetry to horizontal transverse isotropic (HTI) medium:

1. Fractures are invariant under rotation about the normal to the facture faces (rotationally invariant)
2. Fractures have no corrugation or surface roughness

The above assumptions result in:

$K_{NV} = K_{NH} = K_{VH} = 0$, $\Delta NV = \Delta NH = \Delta VH = 0$, and

$$K_V = K_H = K_T, \ \Delta V = \Delta H = \Delta T. \tag{6.14}$$

Amplitude variation with offset and azimuth (AVOA) has been studied extensively (Mallick and Frazer, 1991; Rüger, 1998; Rüger and Tsvankin, 1997, Alhussain et al., 2007). Thomsen's (1986) weak anisotropy parameters for HTI medium ($\epsilon^v, \delta^v, \gamma^v$) are used routinely to represent TI media and have a simple relationship to stiffness coefficients (Bakulin et al., 2000):

$$\epsilon^{(v)} = \frac{C_{11}-C_{33}}{2C_{33}}, \tag{6.15}$$

$$\delta^{(v)} = \frac{(C_{13}+C_{55})^2-(C_{13}-C_{55})^2}{2C_{33}(C_{33}-C_{55})}, \tag{6.16}$$

$$\gamma^{(v)} = \frac{C_{66}-C_{44}}{2C_{44}}. \tag{6.17}$$

Fracture weaknesses can be computed directly from both Thomsen's parameters and Vp/Vs ratio (Bakulin et al., 2000):

$$\Delta N = -\frac{\epsilon^{(v)}}{2g(1-g)}, \tag{6.18}$$

$$\Delta T = \frac{1}{2g}\left[\frac{1-2g}{1-g}\epsilon^{(v)} - \delta^{(v)}\right], \tag{6.19}$$

$$g = \frac{V_s^2}{V_p^2}. \tag{6.20}$$

Shaw and Sen (2006) expressed AVOA reflection coefficients directly as a function of fracture weaknesses:

$$R^{total}(i, \emptyset) = R^{iso}(i) + R^{ani}(i, \emptyset, \Delta), \tag{6.21}$$

$$\Delta^T = (\Delta N, \Delta V, \Delta H, \Delta NV, \Delta NH, \Delta VH), \quad (6.22)$$

R^{iso} represents the isotropic part of the reflection coefficient and depends only on the incident angle i. R^{ani} is the anisotropic part of the reflection coefficient and is a function of incident angle i, azimuth $\emptyset$, and fracture weaknesses Δ. Shaw and Sen (2004) derived linearized reflection coefficients by presenting a weak anisotropic medium as a volume of scatterers embedded in a background isotropic medium. They used asymptotic ray theory and the method of stationary phase to show that the scattering function $S(r_0)$ corresponding to the singly scattered wavefield relates to the linearized PP-reflection coefficients as follows:

$$R_{pp}(i) = \frac{1}{4\rho_{0\,cos^2(i)}} S(r_0), \quad (6.23)$$

$$S(r_0) = \Delta\rho\xi + \Delta_{C_{ijkl}}\eta_{ijkl}, \quad (6.24)$$

$$\xi = t_i t_j'|_{r=r_0}, \quad (6.25)$$

$$\eta_{ijkl} = t_i' p_j' t_k p_l|_{r=r_0}, \quad (6.26)$$

where ρ_0 is the density of the background medium. $\Delta\rho$ is the perturbation in density and $\Delta_{C_{ijkl}}$ is the perturbation in elastic stiffness. p is the slowness, and t are the polarization vectors. The scattered wave is denoted by a prime. The position vector r_0 is the point on a horizontal interface that separates two weak isotropic or anisotropic media.

Shaw and Sen (2006) derived the dependence of PP-reflection coefficients on fracture weaknesses by collecting the coefficients η_{ijkl} corresponding to each weakness. Under the assumption of weak fracture weakness the derived equation is:

$$\delta R = R_{pp}^{obs}(i, \emptyset) - R_{pp}^{iso}(i) = A_{sens}\Delta, \tag{6.27}$$

$$A_{sens} = \frac{1}{4}[a_N, a_V, a_H, a_{NV}, a_{NH}, a_{VH}], \tag{6.28}$$

where R_{pp}^{obs} is our observed reflection coefficient and R_{pp}^{iso} is the reflection coefficient of the isotopic background. A_{sens} is the sensitivity matrix. For a given incidence angle and azimuth, the row elements of A_{sens} are given by:

$$a_N = (1-2g)^2 + [(1-2g) + 2g(1-2g)cos2\emptyset]sin^2 i + \left[\left(1 - 2g + \frac{3}{2}g^2\right) + 2g1{-}gcos2\emptyset{+}12g2cos4\emptyset sin2i\, tan2i, \right. \tag{6.29}$$

$$a_v = -2g(1 + cos2\emptyset)sin^2 i, \tag{6.30}$$

$$a_H = \frac{g}{2}(1 - cos4\emptyset)sin^2 i\, tan^2 i, \tag{6.31}$$

$$a_{NV} = 0, \tag{6.32}$$

$$a_{NH} = 2\sqrt{g}(1-g)sin2\emptyset sin^2 i + \sqrt{g}[2(1-g)sing2\emptyset + gsing4\emptyset]\, sin^2 i\, tan^2 i, \tag{6.33}$$

$$a_{VH} = 0, \tag{6.34}$$

ESTIMATING ΔN AND ΔT FROM A FRACTURED SYNTHETIC MODEL

The synthetic model introduced in Chapter 4 (Figure 4.2) is used here to invert for ΔN and ΔT. The model consists of a vertically fractured reservoir that is divided into 14 compartments (Figure 4.1) representing the gradual change in vp, vs, density and porosity within the reservoir. The reservoir has an isotropic overburden layer. The AVOA response of the layer below the reservoir is used to invert for ΔN and ΔT parameters. Figure 6.1a shows the ray path of a wave reflected from Layer4/Layer5 interface. Full-waveform numerical simulation is performed at all azimuths. One CMP gather for a seismic wave traveling across the fractures (0° azimuth) is shown in figure 4.4. The normalized AVOA response can be seen in figure 6.1b. The azimuthal change of amplitudes caused by vertical fractures is clear at large offsets.

The ΔN and ΔT values for each reservoir compartment are calculated directly from elastic coefficients of the HTI medium using equations 6.15, 6.16, 6.18 and 6.19. Elastic coefficients that are used as an input to the numerical simulation and corresponding ΔN and ΔT values are shown in table 6.1. Both parameters are almost constant in all reservoir units, and the average values are 0.62 and 0.14 for ΔN and ΔT, respectively. This is extremely helpful because we are inverting for one value for each parameter that represents the entire reservoir units.

AVOA inversion for ΔN and ΔT parameters

Equation 6.27 is used to invert for ΔN and ΔT parameters. In order to perform the inversion, knowledge of the orientation of the vertical fractures as well as information about the physical parameters of isotropic background (Vp/Vs) are required. For the synthetic example both parameters are available. In equation 6.27, the term $R_{pp}^{iso}(i)$ is the reflection coefficient for the interface separating the overlying medium from the

isotropic medium in which fractures are embedded. $R_{pp}^{iso}(i)$ is set to be equal to $R_{pp}^{fracture\ parallel}(i)$ where seismic waves do not see factures as they travel parallel to them. The isotropic reflection coefficient term is subtracted from the observed amplitude data to isolate the effect of fractures on the AVOA.

A linear least-squares inversion is performed to estimate the fracture weaknesses ΔN and ΔT:

$$\Delta = [{A_{sens}}^T A_{sens}]^{-1} {A_{sens}}^T \delta R, \tag{6.35}$$

where $\Delta^T = [\Delta N\ \Delta T]$ and we set $a^T = (a^V + a^H)/2$.

Inverted ΔN and ΔT are equal to 0.64 and -0.048, respectively, and the average values calculated directly from input parameters are 0.62 and 0.14. This means that ΔN is successfully inverted for, but ΔT is not. I attribute this difficulty in the parameter estimation to the complexity of equations 6.16 and 6.19 where ΔT depends on many medium parameters for accurate prediction. It depends on $C_{11}, C_{33}, C_{13}, C_{55}, and\ v_p/v_s$. The effect of ΔT on PP-reflection coefficients is prominent at large angles of incidence only (Shaw and Sen, 2006). This behavior is similar to the effect of S-wave velocity on PP-reflection coefficient from an interface separating two isotropic media. On the other hand, ΔN depend only on $C_{11}, C_{33}, and\ v_p/v_s$ and the effect of ΔN on the reflection coefficients is at most incidence angles.

It is important to understand the significance of ΔN and how it is related to fracture parameter prediction. Note that ΔN is directly related to crack density by the following relation (Schoenberg and Douma, 1988):

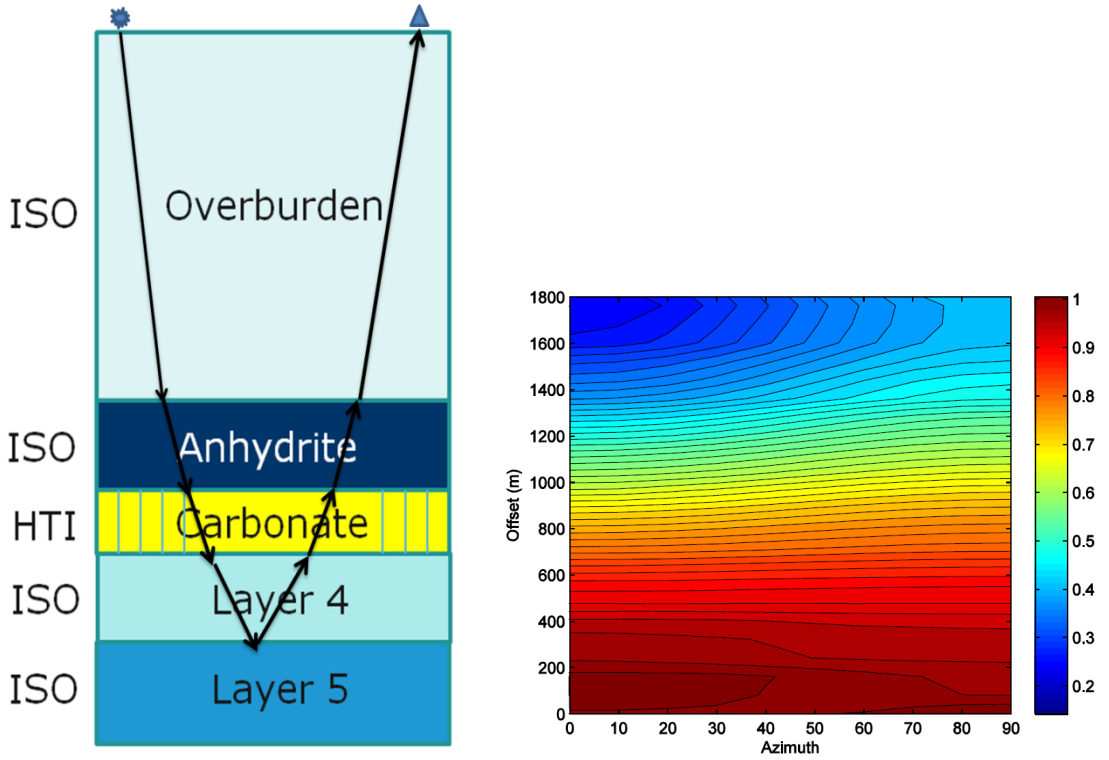

(a) (b)

Figure 6.1: (a) Forward model containing isotropic overburden and fractured carbonate reservoir. The black arrows indicate ray path of reflection from a reflector below the reservoir, (Layer 4/Layer 5) interface. (b) AVOA Rpp reflection response for a reflector below the reservoir. Fracture direction is at azimuths 90 degrees.

\

Compartment	C11	C33	C13	C44	C55	ΔN	ΔT
1	15.2	31.2	6.8	10.1	7.8	0.58	0.14
2	16.5	33.7	7.6	10.7	8.3	0.58	0.14
3	17.7	36.6	7.9	11.7	9.1	0.59	0.14
4	18.6	38.9	8.4	12.4	9.6	0.60	0.14
5	20.1	42.2	8.6	13.8	10.7	0.60	0.14
6	21.8	46.7	9.7	14.9	11.6	0.62	0.14
7	23.6	49.6	9.8	16.4	12.7	0.60	0.15
8	25.4	52.7	10.9	17.2	13.3	0.59	0.15
9	27.9	58.7	11.6	19.4	15.0	0.60	0.15
10	27.2	59.1	12.3	18.8	14.6	0.65	0.14
11	28.3	61.9	12.9	19.5	15.2	0.65	0.14
12	31.6	68.7	13.7	22.2	17.2	0.64	0.14
13	33.3	70.2	14.9	22.4	17.5	0.63	0.14
14	36.2	75.2	16.1	23.8	18.5	0.62	0.14

Table 6.1: HTI elastic stiffness parameters for 14 reservoir compartments and the computed normal (ΔN) and tangential (ΔT) weakness parameters.

$$\Delta N = \frac{4e}{3g(1-g)}, \tag{6.36}$$

where e is crack density and $g = \frac{V_s^2}{V_p^2}$.

Assuming that we have an accurate value of Vp/Vs ratio, we can have a good idea about crack density, and ΔN can then be used to invert for fracture density parameter.

Proposed ΔN and ΔT inversion method

A method to remove the effect of an anisotropic overburden in order to recover true reservoir fracture parameters is presented in chapter 4. It involves analyzing AVOA for a reservoir pick and for a reflector below the reservoir. Seismic gathers are transformed to delay-time slowness domain, and the ratio of reservoir pick to the layer below the reservoir is taken in order to remove transmission effect from the overburden. The ratio attribute that corresponds to two models, one has an isotropic overburden (Figure 4.2) and the other has anisotropic overburden (figure 4.3), are used here to invert for both ΔN and ΔT parameters. Equation 6.27 is modified in order to use ratio amplitudes instead to conventional AVOA as follows:

$$\delta R = Rratio_{pp}^{obs}(i,\emptyset) - Rratio_{pp}^{iso}(i) = \frac{A_{sens}}{\mathrm{R}_{\mathrm{pp}}^{\mathrm{top}}(i,\emptyset)*\propto}\Delta, \tag{6.37}$$

where $Rratio_{pp}^{obs}$ is the ratio amplitudes for observed data and is a function of angle and azimuth. $Rratio_{pp}^{iso}$ is the ratio amplitudes for isotropic background and is a function of angles. A_{sens} is the sensitivity matrix defined in equations 6.29 to 6.34 normalized by $\mathrm{R}_{\mathrm{pp}}^{\mathrm{top}}$ which is the reflection amplitudes of top reservoir as a function of angle and azimuth. $\propto$ is a scalar. Note that we do not need to know or use the scalar in our

inversion; we will obtain scaled values of Δ, and the relative values will not be strongly affected.

Inversion results of both models (Isotropic and anisotropic overburden) are 0.551 and 0.546 for ΔN and -5.94 and -8.6 for ΔT. It can be concluded that ΔN is reasonably estimated (with 11% and 12% error) when compared to the derived value (0.62) from HTI elastic coefficients. I believe that this discrepancy in ΔN is related to the composite effect of the term: $T_{2\to3}^{down}(\mathrm{R}_3/\mathrm{R}_2)T_{3\to2}^{up}$ of equation 4.1. The ratio of reflection coefficient of a reflector below the reservoir R_3 and reservoir top R_2 at different angle of incidence and azimuth could be the cause of the deviation of ΔN estimation. Overall, I demonstrate that the ΔN parameter can be successfully inverted for using the ratio method. On the other hand, the inversion of ΔT parameters is unstable for the same reasons mentioned in the previous section.

Inversion of ΔN from real data

The inversion of the ratio attribute from synthetic data for ΔN parameter is stable. This motivates me to apply the method to real data despite the fact that quantitative analysis of real data is challenging. The real data set introduced in chapter 5 is used here. Equation 6.37 is used for the inversion. The observed ratio attribute which is a function of angle an azimuth represents the term $Rratio_{pp}^{obs}$. The isotropic part the ratio attribute or $Rratio_{pp}^{iso}$ is taken to be the ratio attribute for fracture strike azimuth direction. This means the inversion requires knowledge about fracture direction, which we already inverted for in chapter 5. Another important parameter needed for the inversion is Vp/Vs

ratio, which is estimated from the well logs in the area. This parameter is assumed to be constant.

Inversion results for ΔN can be seen in figure 6.2, and a smoothed version is shown in figure 6.3. Crack density are calculated directly from ΔN parameter using equation 6.36 (Figure 6.4). Hot colors correspond to high and can be interpreted as high crack density (equation 6.36). On the other hand cold colors indicate low crack density areas. The comparison of facture density, inverted for in chapter 5, and the fracture density computed from ΔN parameter is shown in figure 6.5. Both attributes are similar and the white arrows highlight such similarity. There are some areas of discrepancy, and they are highlighted with black arrows. A possible reason of this difference is the assumption of constant Vp/Vs ratio, which the ΔN parameter is highly dependent on (equation 6.36). Another reason is the assumption of correct fracture direction information taken from the inversion performed and described in chapter 6. Overall the two maps in figure 6.5 are similar where more fractures are located at the hinge of the anticline structure and variability of the provided attribute is valuable in locating areas of sweet spots within the reservoir interval.

SUMMARY

Conventional AVOA inversion results applied to a synthetic model generated and described in chapter 4 show that ΔN is reliably estimated as long as the background isotropic parameter is estimated with good accuracy. This information is usually taken from well logging information. On the other hand, inversion for ΔT from Rpp information is not successful and I attribute that to the dependence of ΔT on many medium parameters for accurate prediction. It depends on $C_{11}, C_{33}, C_{13}, C_{55}, and\ v_p/v_s$.

Another reason is that effect of ΔT on PP-reflection coefficients is prominent at large angles of incidence only. The best solution to the problem is to acquire a multi-component survey where converted waves can help to estimate ΔT parameter.

The inversion is also done to the ratio attribute derived in chapter 4. ΔN is also reliably inverted for with some discrepancy, which I believe is related to the composite effect of the term: $T_{2\to3}^{down}(\mathrm{R}_3/\mathrm{R}_2)T_{3\to2}^{up}$ of equation 4.1. The ratio of reflection coefficient of a reflector below the reservoir R_3 and reservoir top R_2 at different angles of incidence and azimuth could be the cause of the deviation of ΔN estimation. It is important to note that ΔN parameter is directly proportional to fracture density (equation 6.36) and high ΔN values can be attributed to high crack density values.

The last part of this chapter is the real data application where ΔN is inverted for using ratio attribute data derived in chapter 5. The inversion requires knowledge about fracture direction which we already inverted for in chapter 5. Another important parameter needed for the inversion is Vp/Vs ratio, which is estimated from well logs in the area. This parameter is assumed to be constant. Inversion results are promising where fracture density computed from ΔN is compared to fracture density parameter inverted for in chapter 5. The maps of both attributes are similar where more fractures are located at the hinge of the anticline structure, and the variability of the attributes is valuable in locating areas of sweet spots within the reservoir interval.

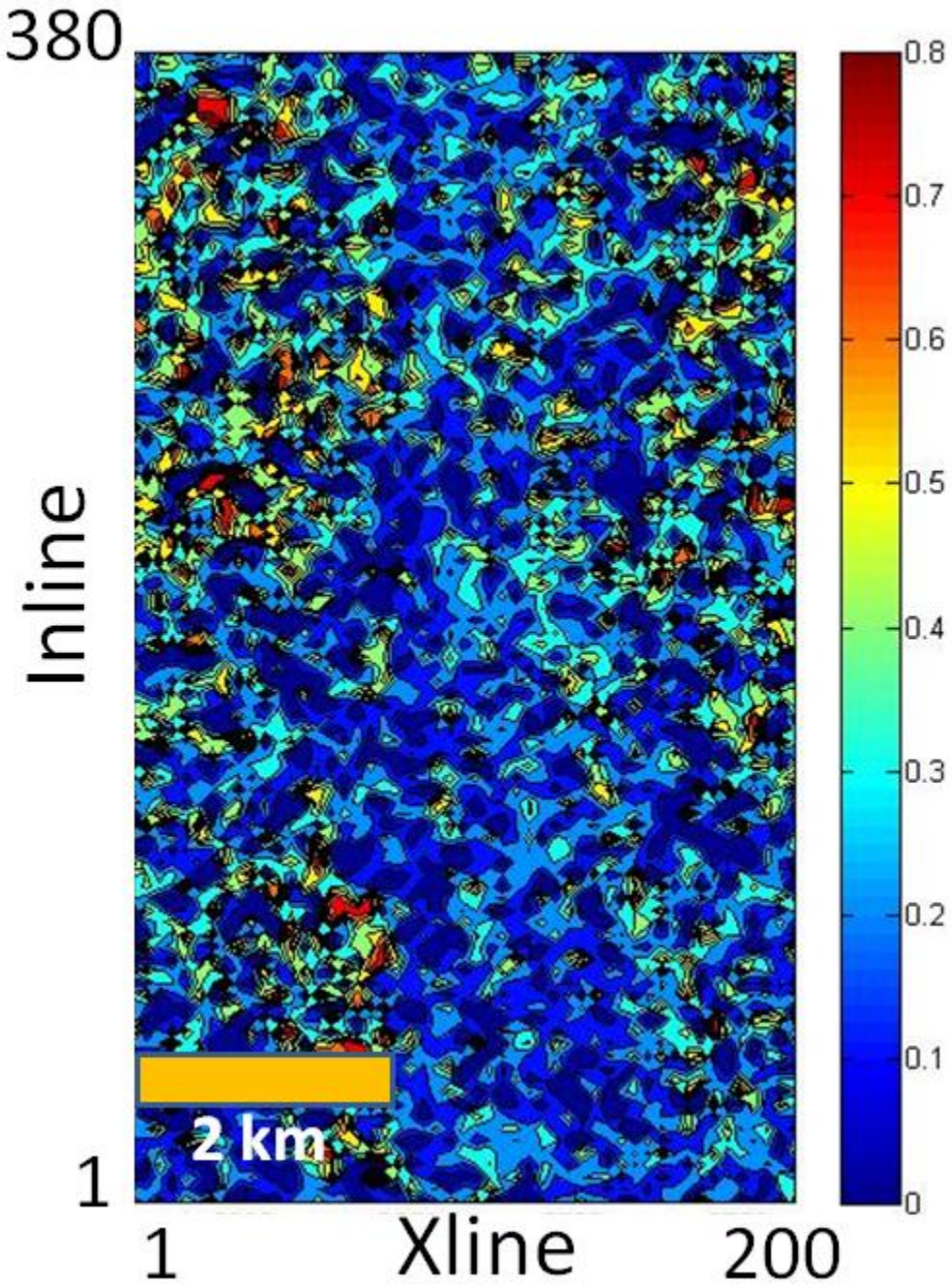

Figure 6.2: Inverted ΔN parameter from real data. Hot colors indicate high values which correspond to high fracture zones.

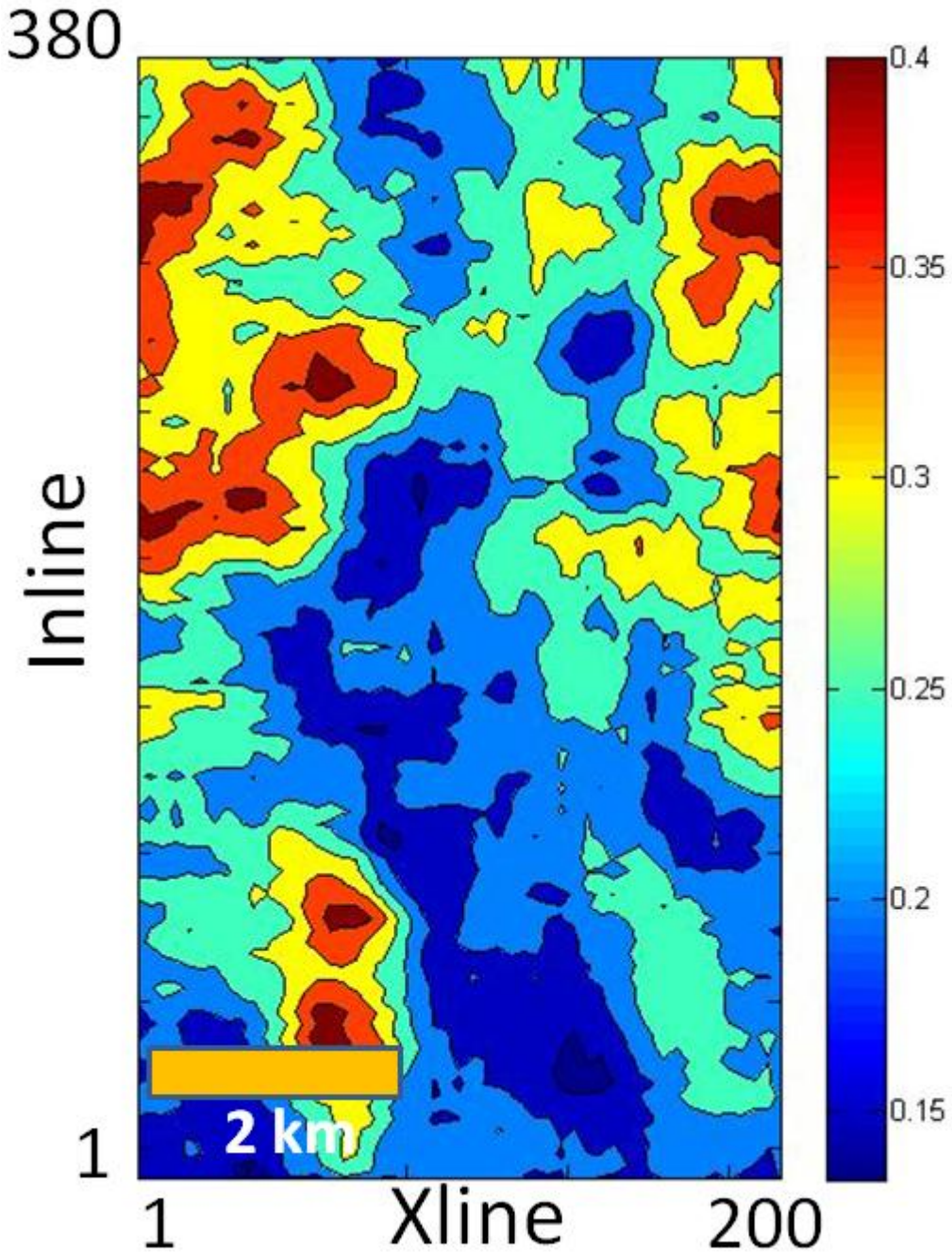

Figure 6.3: Inverted ΔN smoothed parameter from real data. Hot colors indicate high values which correspond to high fracture zones.

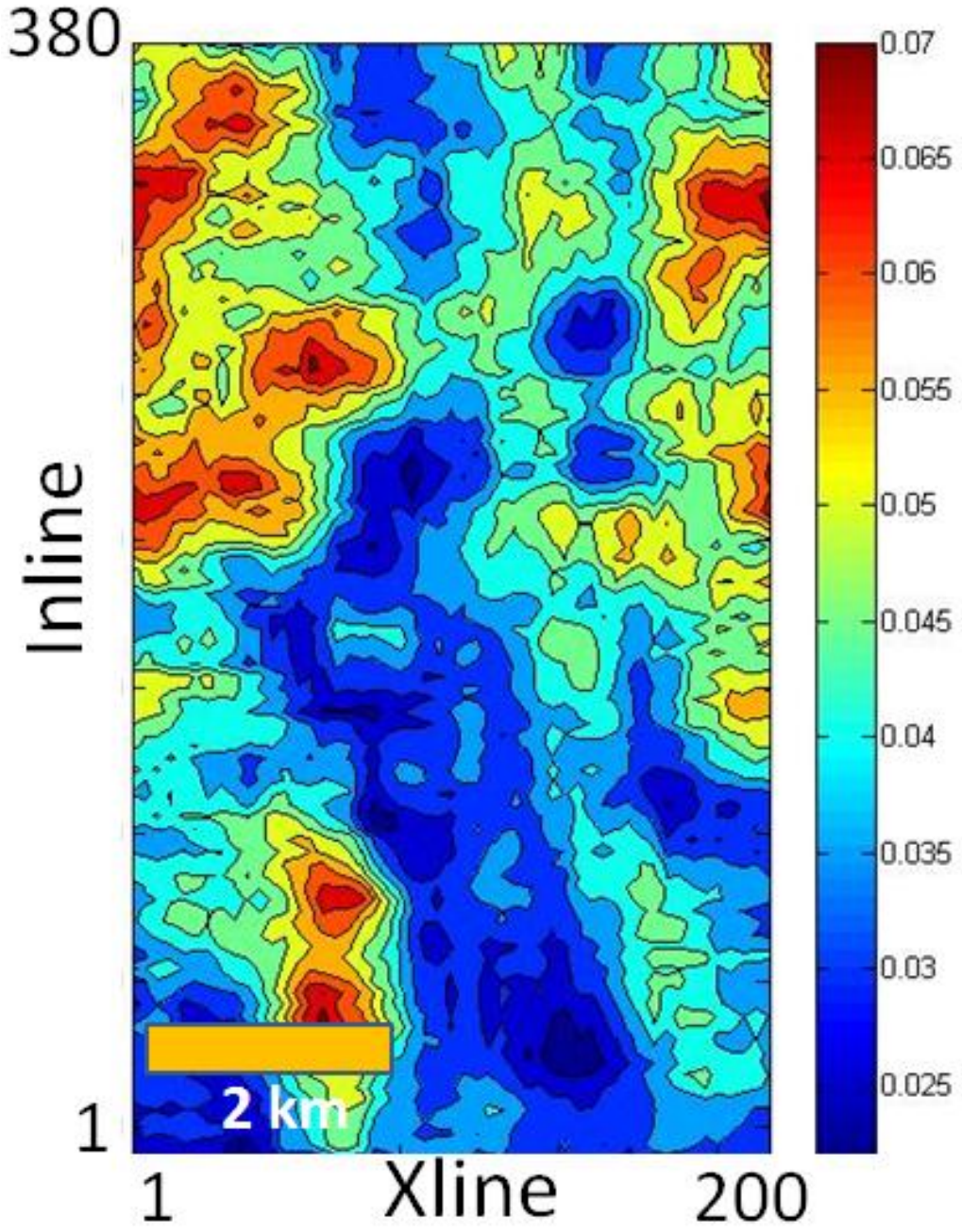

Figure 6.4: Inverted fracture density from ΔN parameter. Hot colors indicate high fracture zones.

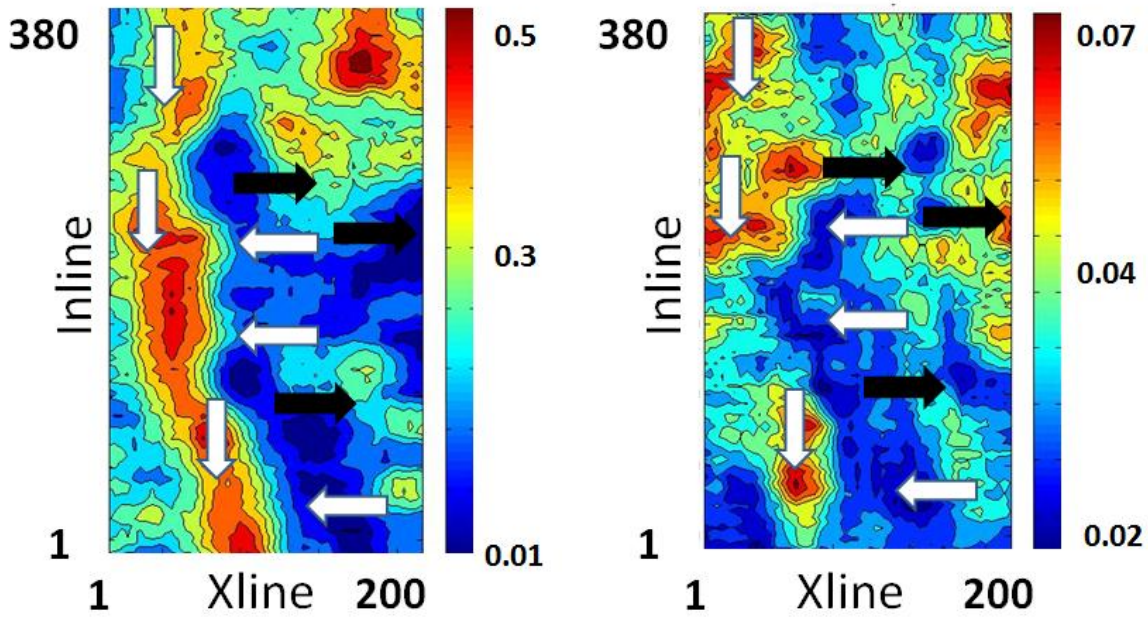

Figure 6.5 (a) Inverted fracture density parameter (smoothed) from chapter 5. (b) Inverted fracture density from ΔN parameter (smoothed). Hot colors indicate high values which correspond to high fracture zones. Both attributes are similar and the white arrows highlight such similarity. There are some areas of discrepancy and they are highlighted with black arrows.

Chapter 7: Conclusions and Limitations

CONCLUSIONS

In this dissertation, first I investigated the sensitivity of different fracture parameters to seismic amplitudes, which was followed by the development of a new method to invert for these parameters from seismic data. Finally the technique was applied to field data from an oil field from the Arabian Peninsula.

For the sensitivity study of fracture parameters, FMI analysis indicated one set of dominant fractures. The change in Epsilon due to porosity appears to be the highest at high crack density, high fluid bulk modulus and low porosity. Change in Epsilon due to crack density is the highest at low fluid bulk modulus and high porosity and high crack density. Epsilon change due to fluid bulk modulus is the greatest at low porosity, high crack density and low fluid bulk. Crack density is the easiest parameter to discriminate in the intercept-gradient plot. Porosity estimation is more robust at high crack density and fluid bulk modulus is the most difficult parameter to discriminate. Crack density and Porosity are best estimated when seismic wave travels across the fractures.

A method to remove the effect of an anisotropic overburden in order to recover true reservoir fracture parameters is presented. It involves analyzing AVOA for a reservoir pick and for a reflector below the reservoir. Seismic gathers are transformed to delay-time slowness (tau-px,py or tau-p,azimuth) domain and the ratio of reservoir pick to the layer below the reservoir is taken in order to remove transmission effect from the overburden. Note that it is the ray-parameter and not the angle that remains constant in

different layers and that the reflection/transmission coefficients are fundamentally functions of ray-parameters. That is precisely the reason as to why the ratio method works better in tau-p than in x-t domain. The method is applied to two sets of forward models one containing fractured reservoir with isotropic overburden and the other is the same model but with anisotropic overburden. Conventional analysis in the t-x domain shows that the anisotropic overburden has completely obscured the anisotropic estimation. When the new method is applied, the overburden effect was removed and more reliable anisotropic fracture parameter estimation can be reached.

The ratio method is applied to a P-P 3D data set from the Arabian Peninsula. Fracture density inversion results indicate greater fracturing in the hinge zone of the anticline structure, which agree very well with the structural geology of the anticline. Fracture orientation inversion results agree with FMI logs where fractures have a NW-SE trend. Fracture directions show a general WNW-ESE trend within a selected zone where fractures are believed to have high density.

Post-stack coherency and curvature attributes correlate well with the ratio method. This indicates that new pre-stack proposed ratio method gives reliable results despite the low signal to noise problem of pre-stack gathers. Even though post-stack attributes look similar to those of pre-stack, they are not suitable for quantitative estimation of fracture parameters.

Conventional AVOA inversion results applied to a synthetic model generated and described in chapter 4 show that the ΔN parameter is reliably estimated as long as the background isotropic parameter is estimated with good accuracy. This information is

usually taken from well logging information. On the other hand, inversion for ΔT from Rpp information is not successful and I attribute that to the dependence of ΔT on many medium parameters for accurate prediction. It depends on $C_{11}, C_{33}, C_{13}, C_{55}, and\ v_p/v_s$. Another reason is that effect of ΔT on PP-reflection coefficients is prominent at large angles of incidence only. The best solution to the problem is to acquire a multi-component survey where converted waves can help to estimate ΔT parameter.

The inversion is also done to the ratio attribute derived in chapter 4. ΔN is also reliably inverted for with some discrepancy which I believe is related to the composite effect of the term: $T_{2\rightarrow3}^{down}(\mathrm{R}_3/\mathrm{R}_2)T_{3\rightarrow2}^{up}$ of equation 4.1. The ratio of reflection coefficient of a reflector below the reservoir R_3 and reservoir top R_2 at different angles of incidence and azimuth could be the cause of the deviation of ΔN estimation. It is important to note that ΔN parameter is directly proportional to fracture density (equation 6.36) and high ΔN values can be attributed to high crack density values.

The last part of chapter 6 is the real data application where ΔN is inverted for using ratio attribute data derived in chapter 5. The inversion requires knowledge about fracture direction which we already inverted for in chapter 5. Another important parameter needed for the inversion is Vp/Vs ratio, which is estimated from well logs in the area. This parameter is assumed to be constant. Inversion results are promising where fracture density computed from ΔN attribute is compared to fracture density parameter inverted for in chapter 5. The maps of both attributes are similar where more fractures are located at the hinge of the anticline structure and the variability of the attributes is valuable in locating areas of sweet spots within the reservoir interval.

LIMITATIONS

For the sensitivity study in chapter 2, it is understood that besides using an idealized earth model, all other effects that might hinder the robustness of parameter estimation like signal-to-noise ratio and overburden effects are ignored. Estimation of fluid bulk modulus in my study area is challenging where the fluid effect of changing oil and water is minimal.

One limitation of applying the new ratio method is the requirement of wide azimuth and long offset seismic dataset with good spatial sampling to insure a reliable x-t to τ-p transformation of individual azimuthal gathers. Another limitation is that the method depends on the ratio of two horizons and at areas of low signal-to-noise ratio, it might not work.

An accurate estimation of ΔN parameter requires knowledge of both fracture direction and background isotropic parameters. One challenge of ΔN inversion is the case of narrow azimuth and/or short offset recording where the fracture direction estimation is limited. Another challenge is the lack of well control where estimation of the Vp/Vs ratio parameter is difficult. Another limitation of ΔN parameter estimation is the effect of the term: $T_{2\to3}^{down}(\mathrm{R}_3/\mathrm{R}_2)T_{3\to2}^{up}$ of equation 4.1. The ratio of reflection coefficient of a reflector below the reservoir R_3 and reservoir top R_2 at different angles of incidence and azimuth could be the cause of the deviation of ΔN estimation.

FUTURE WORK

One of the conclusions from the sensitivity work is that the porosity is best estimated when seismic wave travels across the fractures. Most of the porosity inversion methods are based on the assumption of isotropic pre-stack gathers. I would like to investigate the possibility of using estimated fracture direction attribute from pre-stack azimuthal analysis for better porosity inversion.

I would like to improve the new ratio method to include azimuthal velocity analysis for accurate amplitude extraction in the τ-p domain. I plan to apply the ratio method on several data sets for further testing. I also plan to use multi-component seismic data to investigate the accuracy of the method when applied to p-s section.

Appendix A

REFLECTIVITY METHOD

Introduction

Numerical seismic modeling is a very useful tool in the interpretation of field seismic data, seismic imaging, inversion and evaluating the performance of seismic processing algorithms (Sen, 2011; Ma et. al, 2004). Solution of the partial differential equation (PDE) for seismic wave propagation is needed to generate synthetic seismograms. Depending on the earth model (e.g., acoustic, elastic, anisotropic etc) different forms of the PDE exists. The main advantage of reflectivity method is that it can model almost all kinds of waves with high numerical stability and low computation cost. Numerical methods such as finite differences (Vireux, 1984) and finite elements (Marfurt, 1984; Komatitsch and Tromp, 1999, DeBasabe and Sen, 2007) are accurate but computationally intensive and time consuming.

Plane waves

Plane waves are very important to understand wave propagation. Aki and Richards (2009) has demonstrated that a point source response can be generated by a weighted sum of individual plane wave responses. The amplitude and phase of plane waves undergo changes as they propagate through a stack of flat layers but their wavefront remain planar. Plane waver reflection and transmission coefficients across interfaces can be accounted for by imposing two boundary conditions:

1. Continuity of displacement
2. Continuity of stress

Snell's low takes care of changes in propagation angles across interfaces. In non-vertical propagation angle, a plane wave generates both converted waves and internal multiples with amplitudes corresponding to reflection and transmission coefficients. Individual layer velocities are used to compute travel time changes (Sen, 2011).

Generating plane wave synthetic seismograms for a layered medium is straightforward and involves important parameters:

1. Ray parameter or horizontal slowness (p). This parameter stays constant in all layers and defined as
2. Vertical slowness (q)
3. Vertical delay time (τ)

They are defined as follows:

$$p = \frac{\sin i}{v}, \tag{1}$$

$$q = \frac{\cos i}{v}, \tag{2}$$

$$\tau = 2hq, \tag{3}$$

where i is the incident angle and h is the layer thickness.

The primary PP mode between two layers denoted by l and 2 in the frequency slowness domain is:

$$R(\omega, p) = R_1^{pp} e^{(i\omega 2 h_1 q_1^{pp})}, \tag{4}$$

R_1^{pp} is the PP plane wave reflection. The subscript 1 denotes first interface.

The PP mode reflected from the second layer is as follows:

$$R(\omega, p) = T_{1D}^{pp} R_2^{pp} T_{1U}^{pp} e^{(i\omega 2(h_1 q_1^{pp} + h_2 q_2^{pp}))}, \tag{5}$$

T_{1D}^{pp} and T_{1U}^{pp} are downdoing and upgoing transmission coefficients respectively.

Reflectivity Theory

It is easy to compute seismograms for few phases and layers but earth is complicated and contains many layers and infinite number of ray-paths. The reflectivity theory computes the full response without having to count rays (Sen, 2011). Fuchs and Muller (1971) and Kennett (1983) showed the developments of the theory of the reflectivity method for isotropic media. The derivation of reflectivity method for anisotropic media is shown by Booth and Crampin (1983) and Fryer and Frazer (1984).

The starting point of the derivation is two important equations. The first one is the constitutive relation equation given by:

$$\tau = C : \nabla u, \tag{6}$$

and the second is the equation of motion given by:

$$\rho\omega^2 u = \nabla . \tau + f, \tag{7}$$

were τ is a second rank stress tensor, C is the forth rank elastic stiffness tensor, u is the displacement vector, ω is the angular frequency, and f is a body force term.

Both equations 6 and 7 are transformed into a system of ordinary differential equations (ODE) in depth z by applying a Fourier transform in x and y. The resultant equation is:

$$b = i\omega A_s b + f, \tag{8}$$

$$b(\omega, p) = [u_x, u_y, u_z, \tau_{xz,}\tau_{zz,}\tau_{yz,}]^T, \tag{9}$$

where b is the stress displacement vector which is a function of frequency and ray parameter p. A_s is the system matrix which is a function of elastic coefficients. f is a body force term.

For both isotropic and transversely isotropic (TI) media like vertical transverse isotropic media (VIT) and horizontal transverse isotropic media (HTI), equation (9) decouples into two systems, one correspond to P-SV system and the other one correspond to SH system.

In reflectivity theory, the solution of the ODE system in equation (10) is obtained using an invariant imbedding or a reflection matrix approach (Kennett, 1983). This method is widely used in seismology because of its ray-interpretation and easy generalization to azimuthally anisotropic media like HTI (Sen, 2011). Kennett (1983) used an unconditionally stable reflection matrix approach where the propagation uses the eigenvalues and eigenvector of the system matrix A which are used to define four upgoing and downgoing reflection and transmission coefficient matrices. If we propagate these through a stack of layers we get composite reflection matrix containing the effects of reflection, transmission, converted waves and internal multiples. The iteration equations used to derive reflection and transmission coefficients for a layered model in figure (A1) are:

$$\begin{aligned} R_D^{AC} &= R_D^{AB} + T_U^{AB} R_D^{BC} [I - R_U^{AB} R_D^{BC}]^{-1} T_D^{AB} \\ T_D^{AC} &= T_D^{BC} [I - R_U^{AB} R_D^{BC}]^{-1} T_D^{AB} \\ R_U^{AC} &= R_U^{BC} + T_D^{BC} R_U^{AB} [I - R_D^{BC} R_U^{AB}]^{-1} T_U^{BC} \\ T_U^{AC} &= T_U^{AB} [I - R_D^{BC} R_U^{AB}]^{-1} T_U^{BC} \end{aligned} \tag{10}$$

From the reflection and transmission matrices of two zones AB and BC in figure (A1) we can calculate the response of region AC using equation (10).

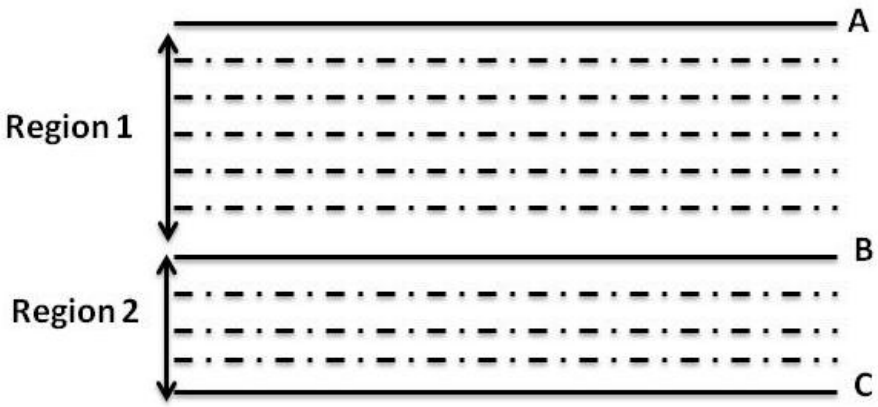

Figure A1: A layered model which consists of zones AB and BC from a stack of layers. If the upgoing and downgoing relfection and transmission matrices for these two zones are know, those for the entire stack (AC) can be generated using the iteration equations (modified after Sen, 2011).

Appendix B

NOTATIONS

Symbols (s) Description

σ_{ij} = Elements of stress tensor

ε_{ij} = Elements of strain tensor

ε_{kk} = Volumetric strain

λ, μ = Lame's constants

c_{ijkl} = Elastic stiffness tensor

c_{ij} = 6x6 elastic stiffness tensor

$c^{(VTI)}_{ij}$ = Elastic stiffness tensor for vertical transverse isotropic symmetry

$c^{(HTI)}_{ij}$ = Elastic stiffness tensor for horizontal transverse isotropic symmetry

$S^{\shortparallel}$ = Vertically traveling shear wave in HTI media with parallel mode of polarization.

$S^{\perp}$ = Vertically traveling shear wave in HTI media with perpendicular mode of polarization.

$\varphi_0 = i$ = Angle of incident P-wave

φ_1 = Angle of reflected P-wave

φ_2 = Angle of transmitted P-wave

ψ_1 = Angle of reflected S-wave

ψ_2 = Angle of transmitted S-wave

Φ = P-wave potential

Ψ = S-wave potential

ρ = density

α = V_P = P-wave velocity

β = V_S = S-wave velocity

θ = Average of the incidence and transmission angles for the P-wave.

ϕ = Azimuth

A, B, C = Intercept, gradient and curvature

B_{iso} = Isotropic gradient

B_{ani} = Anisotropic gradient

e = Crack density

ξ = Number of cracks per unit volume

a = Average crack radius.

W = Symmetric 2x2 matrix determined by the medium properties around the zero-offset ray

S = Effective compliance matrix

S_b = Compliance matrix of the background

S_f = Compliance matrix of fractures or excess compliance

ΔN = Normal weakness

ΔT = Tangential weakness

g = Square of the ratio of P- and S-wave velocities in the background medium

$C_{11}^{sat}, C_{33}^{sat}, C_{13}^{sat}, C_{44}^{sat}, C_{55}^{sat}$ = Saturated rock elastic constants

K = Bulk modulus of dry host rock

K_g = Bulk modulus of grain material

K_f = Bulk modulus of fluid

ε = Epsilon

Φ = Porosity

$T_{1\to2}^{down}$, $T_{2\to1,}^{up}$ $T_{2\to3}^{down}$, $T_{3\to2}^{up}$ = Upward and downward transmission amplitudes between layers 1, 2 and 3

R_3, R_2 = Reflection amplitudes for layer interface

R_{ratio} = Ratio attribute

t_o = Zero offset time

t_{rnmo} = Reverse normal moveout time

v_{rms} = Root mean square velocity

x = offset

p = Ray parameter or horizontal slowness

τ = Vertical delay time

q = Vertical slowness

η = Geological dip of target horizon

V = P-wave velocity above target

W_{11}, W_{12}, W_{22} = Coefficients representing an azimuthally varying AVO gradient ellipse

G_{max}, G_{min} = Large and small semi-axes of the AVO gradient

G_{ave} = Average gradient

u_1, u_2, u_3 = Components of the slip along x, y, and z directions

h = Separation between two fractures

K_N, K_V, K_T, K_H …

K_{NH}, K_{VH}, K_{NV} = Elements of excess compliance matrix

C = Effective stiffness matrix

C^b = Stiffness matrix of background matrix

C^f = Stiffness matrix of fracture

$\epsilon^{(v)}$, $\delta^{(v)}, \gamma^{(v)}$ = Thomsen's weak anisotropy parameters for HTI medium

R^{iso} = Isotropic part of reflection coefficient

R^{ani} = Anisotropic part of reflection coefficient

Δ = Fracture weaknesses

$S(r_0)$ = Scattering function

ρ_0 = Density of the background medium

$\Delta\rho$ = Perturbation in density

$\Delta_{C_{ijkl}}$ = Perturbation in elastic stiffness

r_0 = Position vector

A_{sens} = Sensitivity matrix

$a_N, a_V, a_H, a_{NV}, a_{NH}, a_{VH}$ = Elements of sensitivity matrix

$Rratio_{pp}^{obs}$ = Ratio amplitudes for observed data

$Rratio_{pp}^{iso}$ = Ratio amplitudes for isotropic background

$\mathrm{R}_{\mathrm{pp}}^{\mathrm{top}}$ = Reflection amplitudes of top reservoir

$\propto$ = A scalar

ω = Angular velocity

b = stress displacement vector

A_s = System matrix

f = body force term

References

Aki, K. I. and Richards, P. G., 1980, Quantitative seismology: W. H. Freeman and Co.

Aki, K. I. and Richards, P. G., 2009, Quantitative seismology: W. H. Freeman and Co.

Alhussain, M. A., 2007, AVOaz response of a fractured medium: Laboratory measurements versus numerical simulations, 78th Annual International Meeting, SEG, Expanded Abstracts, 1-4.

Al-Marzoug, A., F. A. Neves, J. J. Kim, and E. L. Nebrija, 2006, P-wave anisotropy from azimuthal AVO and velocity estimates using 3D seismic data from Saudi Arabia: Geophysics, **71(2)**, E7-E11.

Backus, M., 1962, Long-wave elastic anisotropy produced by horizontal layering: J. Geophys. Res., 67, 4427-4440.

Bahorich, M. S., and, S. L. Farmer, 1995, 3D seismic discontinuity for faults and stratigraphic features: The coherence cube: 65th Annual International Meeting, SEG, Expanded Abstracts, 93-96.

Bakulin, A., I. Tsvankin, and V. Grechka, 2000, Estimation of fracture parameters from reflection seismic data–Part I: HTI model due to a single fracture set: Geophysics, **65**, 1788–1802.

Balharith, H., 2009, Fracture detection using azimuthal P-wave amplitude variation with offset and (AVOA) in a carbonate reservoir, Saudi Arabia, Master thesis, King Faisal University of Petroleum and Minerals (KFUPM).

Biondi, B., and T. Trisserant, 2004, 3D angle-domian common-image gathers for migration velocity analysis, Geophysical prospecting, **52**, 575-591.

Booth, D. C., and Crampin, S., 1983, The anisotropic reflectivity technique: theory, Geophys. J. R. Astr. Soc., 72(3), 755-766.

Bortfeld, R., 1961, Approximation to the reflection and transmission coefficients of plane longitudinal and transverse waves: Geophys. Prosp., **9**, 485-502.

Chopra, S., and K. Marfurt, 2005, Seismic attributes – A historical perspective, Geophysics, **70(5)**, 3SO-28SO.

Crampin, S., E. M., Chesnokov, and R. A. Hipkin, 1984, Seismic anisotropy– the state of the art: First Break, 2, 9-18.

De Basabe, J., and M. K. Sen, 2007, Grid dispersion and stability criteria of some finite element methods for seismic wave propagation modeling, Geophysics, **72(6)**, T81-T95.

Fryer, G. J., and L. N. Frazer, 1984, Seismic waves in stratified anisotropic media, Geophysical J. International, **78(3)**, 691-710.

Fuchs, K., and Mueller G., 1971. Computation of synthetic seismograms with the reflectivity method and comparison with observations, *Geophys. J. R. astr. Soc.* **23**, 417-433.

Gassmann, F., 1951, Elastic waves through a packing of sphere: Geophysics, **16**, 673-685.

Grechka, V. and I. Tsvankin, 1998, 3-D description of normal moveout in anisotropic inhomogeneous media: Geophysics, **63**, 1079-1092.

Gurevich, B., 2003, Elastic properties of saturated porous rocks with aligned fractures: Journal of Applied Geophysics, 54, 203–218.

Gurevich, B., M. Brajanovski, R. J. Galvin, T. M.,Muller and J. Toms-Stewart, 2009, P-wave dispersion and attenuation in fractured and porous reservoirs – poroelasticity approach, Geophysical Prospecting, **57**, 225-237.

Hart, B. S., R. Pearson, and G. C. Rawling, 2002, 3D seismic horizon-based approaches to fracture-warm sweet spot definition in tight-gas reservoirs, The Leading Edge, **21**, 28-35.

Hornby, B. E., L. M. Schwartz, and J. A. Hudson, 1994, Anisotropic effective-medium modeling of the elastic properties of shales: Geophysics, 59, 1570-1583.

Hsu, C. J., and M. Schoenberg, 1993, Elastic wave through asimulated fractured medium:Geophysics, **58**, 964-977.

Hudson, J. A., 1980, Overall properties of a cracked solid: Math. Proc. Camb. Phil. Soc., **88**, 371–384.

----------, 1981, Wave speeds and attenuation of elastic waves in material containing cracks: Geophys. J. Roy. Astr. Soc., **64**, 133–150.

Jenner, E., 2002, Azimuthal AVO: Methodology and data examples: The leading edge, **21**, 782-786.

Kennett, B. L. N., 1983, Seismic wave propagation in stratified media, Cambridge University Press.

Komatitsch, D., and Tromp, J., 1999, Introduction to the spectral element for three dimensional seismic wave propagation, Geophys. J. International, **139**, 806-822.

Lisle, R. J., 1994, Detection of zones of abnormal strains in structures using Gaussian curvature analysis: Bulletin of the American Association of Petroleum Geologists, **78**, 1811-1819.

Liu, E., G. Zelewski, C. Lu, J. M. Reilly and Z. J. Shevchek, 2011, Mitigation of overburden effects in fracture prediction using azimuthal AVO analysis: The leading edge, **30**, 750-756.

Luo, M., I. Takahashi, M. Takanashi, and Y. Tamura, 2005, Improved fracture network mapping through reducing overburden influence: The Leading Edge, 24, 1094-1098.

Luo, M., M. Takanashi, K. Nakayama, and T. Ezaka, 2007, Physical modeling of overburden effects: Geophysics, 72, T37-T45.

Ma, Y., L. Loures, G. F. Margrave, 2004, Seismic modeling with reflectivity method, CREWES research report, **16**, 1-7.

Mallick, S., and L. N. Frazer, 1991, Reflection/transmission coefficients and azimuthal anisotropy in marine seismic studies: Geophys. J. Int, **105**, 241-252.

Marfurt, K. J., 1984, Accuracy of finite-difference and finite-element modeling of the scalar and elastic wave equations, Geophysics, **49**, 533-549.

Marfurt, K. J., R. L. Kirlin, S. L. Farmer, and M. S. Bahorich, 1998, 3-D seismic attributes using a semblance-based coherency algorithm, Geophysics, **63**, 1150-1165.

Martin, M. A., T. L. Davis, 1987, Shear-wave birefringence: A new tool for evaluating fractured reservoirs: The Leading Edge, **6 (10)**, 22-28.

Masaferro, J. L., M. Bulnes, J. Poblet, and M. Casson, 2003, Kinematic evolution and fracture prediction of the Valle Morado structure inferred from 3-D seismic data, Salta Province, northwest Argentina: Bulletin of the American Association of Petroleum Geologists, **87**, 1083-1104.

Mavko, G., T. Mukeji, and J. Dvorkin, 1998, The rock physics handbook: Cambridge University Press.

Mavko, G., T. Mukerji, and J. Dvorkin, 2009, The rock physics handbook: Tools for seismic analysis in porous media: Cambridge University Press.

Montoya, P., W. Fisher, R. Marrett, and R. Tatham, 2002, Estimation of fracture orientation and relative intensity using azimuthal variation of P-wave AVO responses and oriented core data in the Tracata Field, Venezuela, 72nd Annual International Meeting, SEG, Expanded Abstracts, 1-4.

Nelson, R.A., 2001, Geologic analysis of naturally fractured reservoirs: Second edition, Gulf Professional Publishing.

Officer, C. B., 1958, Introduction to the theory of sound transmission with application to the ocean: McGraw-Hill Book Co.

Rüger, A.,1996, Reflection coefficients and azimuthal AVO analysis in anisotropic media: PhD thesis, Colorado School of Mines.

Rüger, A., 1998, Variation of P-wave reflectivity with offset and azimuth in anisotropic media: Geophysics, **63**, 935-947.

Rüger, A., I. Tsvankin, 1997, Using AVO for fracture detection: Analytic basis and practical solutions: The leading edge, **16**, 1429-1434.

Sayers, C. M., 2009, Seismic characterization of reservoirs containing multiple fracture sets, Geophysical Prospecting, 57, 187-192.

Sayers, C. and J. E. Rickett, 1997, Azimuthal variation in AVO response for fractured gas sands: Geophysical Prospecing, 45, 165-182.

Schoenberg, M., 1980, Elastic wave behavior across linear slip interfaces: J. Acoust. Soc. Am., **68**, 1516–1521.

----------,1983, Reflection of elastic waves from periodically stratified media with interfacial slip: Geophys. Prosp., **31**, 265–292.

Schoenberg, M., and C. Sayers, 1995, Seismic anisotropy of fractured rock: Geophysics, **60**, 204–211.

Schoenberg, M., and J. Douma, 1988, Elastic wave propagation in media with parallel fractures and aligned cracks: Geophys. Prosp., **36**, 571–590.

Schoenberg, M., and F. Muir, 1989, A calculus for finely layered anisotropic media: Geophysics, **54**, 581-589.

Sen, M. K., 2006, Seismic inversion, Society of Petroleum Engineers.

Sen, M. K., 2007, Anomalous reflection amplitudes from fractured reservoirs- Failure or AVOA?: The Leading Edge, **26**, 1148-1152.

Sen, M. K., 2011, The reflectivity method, Encyclopedia of solid earth geophysics, Harsh K. Gupta, Springer, 1269-1279.

Sheriff, R. E., 1991, Encyclopaedic dictionary of exploration geophysics: SEG Publication.

Shaw, R. K. and M. K. Sen, 2004, Born integral , stationary phase and linearized reflection coefficients in weak anisotropic media, Geopys. J. Int., 158, 225-238.

Shaw, R. K. and M. K. Sen, 2006, Use of AVOA data to estimate fluid indicator in a vertically fractured medium, Geophysics, **71(3)**, C15-C24.

Shuey, R. T., 1985, A simplification of the Zoeppritz equations: Geophysics, **50**, 609-614.

Sigismondi, M., and J. C. Soldo, 2003, Curvature attributes and seismic interpretation: Case studies from Argentina basins: The Leading Edge, **22**, 1122-1126.

Sil, Samik, M. K. Sen, and B. Gurevich, 2010, Sensitivity analysis of fluid substitution in a porous medium with aligned fractures, 80th Annual International Meeting, SEG, Expanded Abstracts, 1-4.

Slater, C., 1997, Estimation and modelling of anisotropy in vertical and walkaway seismic profiles at two North Caucasus oil fields: Ph.D. Dissertation, University of Edinburgh.

Stoffa, P., P. Buhl, J. B., Diebold, and F. Wenzel, 1981, Direct mapping of seismic data to the domain of intercept time and ray parameter- A plane-wave decomposition: Geophysics, **46**, 225-267.

Teng, L., and G. Mavko, 1996, Fracture signatures on P-wave AVOZ: 66th Annual International Meeting, SEG, Expanded Abstracts, 1818-1821.

Thomsen, L., 1986, Weak elastic anisotropy: Geophysics, 51, 1954-1966.

----------, 2002, Understanding seismic anisotropy in exploration and exploitation: Distinguished Instructor Short Course Notes, SEG.

Timoshenko, S., and J. N. Goodier, 1934, Theory of Elasticity: McGraw-Hill Book Co.

Tsvankin, I., 2001, Seismic signatures and analysis of refection data in anisotropic media: Elsevier Science Publ. Co., Inc.

Tsvankin, I., 2005, Seismic signatures and analysis of reflection data in anisotropic media: *Elsevier Science*, second edition.

Tsvankin , I., J. Gaiser, V. Grechka, M. van der Baan, and L. Thomsen, 2010, Seismic anisotropy in exploration and reservoir characterization: An overview: Geophysics, **75(4)**, 75A15-75A29.

Virieux, J., 1984, SH-wave propagation in heterogeneous media: Velocity-stress finite-difference method, Geophysics, **49**, 1933-1957.

Wang, J., H. Kuehl, and M. Sacchi, 2003, Least-squares wave-equation AVP imaging of 3D common azimuth data: 73rd Annual International Meeting, SEG, Expanded Abstracts, 1039-1042.

Wayne, N., W. Schechter, and L. Thompson, 2006, Naturally Fractured Reservoir Characterization: Society of Petroleum Engineers.

Yilmaz, O, 2001, Seismic Data Analysis: Processing. Inversion and Interpretation of Seismic Data, vol. 2: SEG Publication.

Zoeppritz, K., 1919, On the reflection and propagation of seismic waves: Gottinger Nachrichten, **1**, 66-84.